CHALMERS

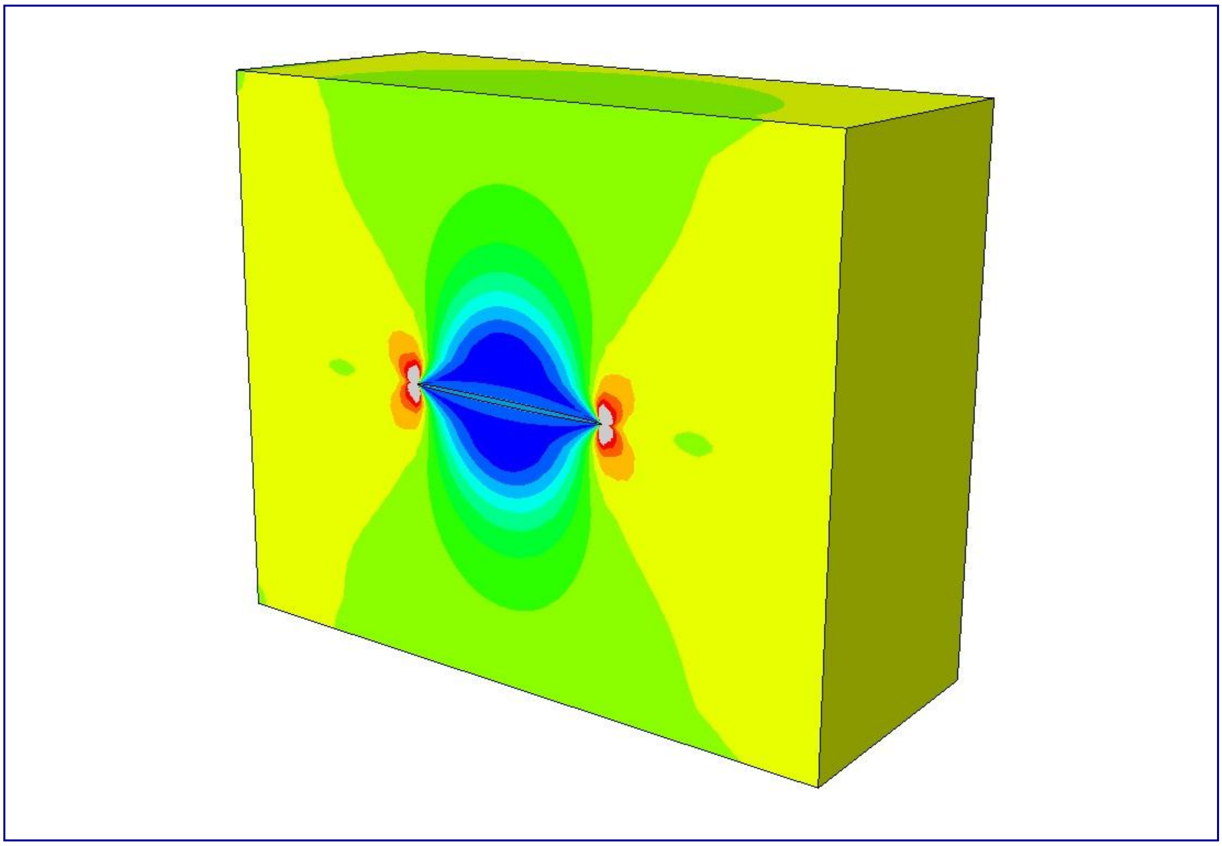

Stationary 3D crack analysis with Abaqus XFEM for integrity assessment of subsea equipment

Master's Thesis in Applied Mechanics

MICHAEL LEVÉN

DANIEL RICKERT

Department of Applied Mechanics
Division of Material and Computational Mechanics
CHALMERS UNIVERSITY OF TECHNOLOGY
Göteborg, Sweden 2012
Master's thesis 2012:35

MASTER’S THESIS IN APPLIED MECHANICS

Stationary 3D crack analysis with Abaqus XFEM for integrity assessment of subsea equipment

MICHAEL LEVÉN

DANIEL RICKERT

Department of Applied Mechanics
Division of Material and Computational Mechanics
CHALMERS UNIVERSITY OF TECHNOLOGY
Göteborg, Sweden 2012

Stationary 3D crack analysis with Abaqus XFEM for integrity assessment of subsea equipment

MICHAEL LEVÉN

DANIEL RICKERT

© MICHAEL LEVÈN, DANIEL RICKERT, 2012

Master's Thesis 2012:35
ISSN 1652-8557
Department of Applied Mechanics
Division of Material and Computational Mechanics
Chalmers University of Technology
SE-412 96 Göteborg
Sweden
Telephone: + 46 (0)31-772 1000

Cover:
The von Mises stress field of a cracked specimen subjected to tension using XFEM in Abaqus.

Chalmers Reproservice
Göteborg, Sweden 2012

Stationary 3D crack analysis with Abaqus XFEM for integrity assessment of subsea equipment
Master’s Thesis in Applied Mechanics
MICHAEL LEVÉN
DANIEL RICKERT
Department of Applied Mechanics
Division of Material and Comput1tional Mechanics
Chalmers University of Technology

ABSTRACT

Subsea equipment provided by FMC is used under the most extreme conditions in the North Sea and is exposed to severe functional and environmental loading conditions. Today, assessment of cracks and crack growth are based on handbook standards. The implementation of a new fracture mechanics based approach to analysis may significantly extend equipment life while improving model accuracy and system reliability. Crack modeling using conventional FEM is accurate, but problematic with respect to modeling. Therefore, an investigation of crack modeling using the extended finite element method (XFEM) is conducted. The method simplifies the modeling of cracks by adding a priori knowledge of the solution in the finite element space. Modeling cracks using conventional FEM can be cumbersome due to the fact that the mesh has to match the crack geometry. XFEM alleviates this shortcoming and allows the crack to be represented independently of the mesh.

The XFEM tool in Abaqus is evaluated for three dimensional stationary cracks with a variety of parameters and features such as meshing technique, element size, symmetry and submodeling. The purpose is to find a robust and flexible strategy to model cracks. The strategy is verified through handbook cases modeled in Abaqus, where the accuracy has been evaluated. Reference cases in the thesis consist of three dimensional closed-form solutions of finite plates with various crack configurations. Also finite plates including cracks at holes/notches have been studied. The Mode I stress intensity factor acquired for the crack configurations serves as the main parameter in the comparison between models.

Good agreement between the XFEM Abaqus analyses and the closed-form handbook solutions is found for general cracks, with errors ranging between three and ten percent. XFEM models of cracks placed by holes and notches give insufficient correlation with the closed-form solutions, with as much as 100 percent disagreement. Based on the evaluations and obtained results, a strategy for general crack modeling is proposed.

Contents

Preface

The thesis has been conducted as the final part for the Master of Science in Applied Mechanics at Chalmers University of Technology. The work was carried out during 2012 at Xdin AB in Göteborg for FMC Technologies in Kongsberg, Norway. The work has been supervised by Mikael Almquist and Timo Mäki at Xdin AB, Per Thomas Moe and Anders Wormsen at FMC Technologies. Supervisors at Chalmers have been Associate Professor Fredrik Larsson and Assistant Professor Martin Fagerström. Examiner was Martin Fagerström.

We are very grateful to all the people that have followed and helped us on our way in this project. We want to express our gratitude to our supervisors for providing us with invaluable knowledge and guidance throughout the project. In addition, we would like to thank Professor Lennart Josefson CTH and Jan Granlund Simulia for their support in the project.

We also would like to thank the employees in the respective offices (Xdin AB and FMC Technologies) that have contributed to a very pleasant atmosphere to work at.

Göteborg September 2012

Michael Levén, Daniel Rickert

1 Introduction

1.1 Background

The equipment and service in the subsea industry is highly constrained by integrity assessment. Therefore, large demands lie upon finite element analyses to assure and continuously improve the integrity assessments. An important aspect to cope with the competitive market is accuracy and efficiency in the analyses. FMC Technologies is a world-leading company in supplying subsea equipment and service for oil and gas wells, constantly challenged by the aforementioned difficulties. Equipment provided by FMC is used under the most extreme conditions in the North Sea and is exposed to severe functional and environmental loading conditions. Therefore, systematic structural analysis of riser and subsea installation is performed both as a part of the system development and in the establishment of project specific operating limitations and fatigue estimates. Advanced methods have been established in order to facilitate exact predictions of system responses.

Assessment of cracks and crack growth is an essential part of the analysis regarding subsea equipment. The subsea industry has so far adopted a conservative approach to treatment and assessment of cracks; no detectable cracks can be tolerated. In accordance with today’s need for sustainable development, a more accurate assessment for safe cracks is of interest. By increasing the tolerance interval for flaws and fatigue damage, the need for service and new material is decreased. In this way, both financial and material resources are saved.

Today, analyses regarding assessment of cracks and crack growth are performed according to handbook standards. In the area connected to flaws, focus lies on the standards BS 7910 [1], DNV-RP-C203 [2] and ISO 13628-7 [3]. BS 7910 is a guide to methods for assessing the acceptability of flaws in metallic structures. DNV-RP-C203 gives recommendations on fatigue analysis based on fatigue tests and fracture mechanics. ISO 13628-7 provides guidance, general requirements and recommendations for development of subsea production systems.

The implementation of an improved fracture mechanics based approach to analysis and maintenance may significantly extend equipment life while improving model accuracy and system reliability. Challenges related to a fracture mechanics based approach to crack growth assessment are greater requirements for material data and more complex finite element models.

As a part of the Abaqus/CAE software, Simulia has recently implemented the XFEM (eXtended Finite Element Method) module which allows significantly simplified modeling and assessment of cracks in FEM [4], [5]. The extended finite element method allows for an approximation of cracks in the FE environment without the need for the mesh to follow the crack as in conventional crack modeling techniques. In this context, the crack is geometrically independent of the mesh. The discontinuity in the elements that the crack represents is described through enrichment of the native FE displacement approximation functions. The method enables both stationary cracks and propagating cracks [6], where additional enrichment functions can be added to include the singularity that arises at a crack tip in LEFM (Linear Elastic Fracture Mechanics) [7].

1.2 Purpose

The purpose of this thesis is to understand the potential of crack modeling using the XFEM in Abaqus and to evaluate the possibilities to analyze and assess critical flaw sizes under design loads. In addition, the purpose has also been to enable and perform improvements in the model accuracy and flexibility in the current crack assessment procedure for subsea equipment.

1.3 Limitations

The analysis has been performed solely with stationary pre-existing cracks, due to the complexity and calculation extent of growing cracks. Hence, the analysis has been focused on critical flaw size and position. The exclusion of propagating crack analysis in this work is also motivated by the absence of the special functions to capture the singularity occurring at the tip [6] (crack tip enrichment functions) for crack propagation in Abaqus. The analysis was carried out with a finite number of cracks in a specimen, with the restriction that the cracks may not intersect the same elements [6]. Furthermore, only three-dimensional geometries are studied since two-dimensional stress intensity factor evaluation is not implemented for XFEM in Abaqus 6.11-1.

A linear elastic material model has been used throughout the crack simulations. Hence, the work has only been carried out considering linear elastic fracture mechanics (LEFM). This follows from the fact that Abaqus only allows for elastic material models in stationary XFEM simulations, since only asymptotic crack tip field functions for isotropic elastic material are included [6].

Experimental testing has not been performed to verify the simulations, instead available data in the literature have been used. Only five handbook cases for cracks have been studied as the crack types are well documented and commonly used. For simplicity only loading in Mode I is considered, i.e. stress intensity factor K_I will be evaluated.

1.4 Objectives

The main objective has been to evaluate XFEM in Abaqus. The basis of this evaluation is to enable incorporation of an improved fracture mechanics approach in the integrity assessment of subsea equipment based on the current standards methodology. In relation to the central part of current assessment involving handbook crack cases, the work has been devoted to an evaluation of stationary crack simulations in XFEM. The primary goal here has been to conduct a convergence analysis of the FE discretization, identifying appropriate aspects and parameters for the models. Secondly a verification of the XFEM simulations has been sought, through benchmark tests with analytical and closed-form solutions. Accuracy and flexibility improvements in the models have been the primary focus in the stationary crack analysis, enabling a strategy proposal for improved crack assessment.

1.5 Method

Initially, an evaluation of the XFEM modeling in Abaqus has been performed to discover its capabilities and limitations. Included here is also an investigation in which aspects XFEM could improve the current standards methodology in the most beneficial way, which is considered to be through stationary crack simulation. Focus has consequently been upon the ability to estimate critical flaw size under design loads, meaning that the stress intensity factor (SIF) for a certain crack can be predicted.

The stationary crack evaluation consists of two main parts, a convergence analysis and a benchmark analysis. In the convergence analysis, the FE-discretization is investigated with various crack configurations to obtain converging results. Additionally, convergence analyses of simplified models and modeling techniques are also included.

Within the determined limitations of the XFEM module, a new strategy to analyze cracks has been developed. A proposal for stationary crack analysis has been established, stating related guidelines and verified analyses. The most important aspect of this method is accuracy and flexibility based on the effective implementations associated with the XFEM module. Hence, improvements within the current methodology are possible.

1.6 Thesis outline

Chapter 2 starts with the basic concepts of linear elastic fracture mechanics followed by the calculation of the stress intensity factors. Furthermore, the governing equations for the finite element analysis are stipulated and the extension to XFEM is explained. Lastly the benchmark cases are defined with the respective equation for the stress intensity factor.

In Chapter 3, the procedure to model stationary cracks in Abaqus XFEM is described. It also includes a description of the different features present in an XFEM-model and how they are handled in the FE model. Furthermore, two meshing techniques used throughout the project are explained as well as two model simplification techniques. The post-processing procedure is presented and the output variables used in the evaluations are defined. Lastly the convergence and benchmark analysis performed in the thesis are described.

Chapter 4 explains how the different convergence/benchmark analyses are conducted and what results they gave. A discussion for the analyses is also held to point out what is concluded from each analysis.

In Chapter 5, the results from the convergence/benchmark analyses are used to create guidelines for the different analyses made such as for crack dimension, mesh size and element type.

Lastly, the conclusions made from the evaluation of stationary crack simulation in Abaqus XFEM are presented in the Chaper 6. Furthermore, future work is suggested.

2 Theory

In this chapter, the basics of fracture mechanics and FEM are described and the steps from a finite element approximation to an extended finite element approximation are detailed. Furthermore, some special Abaqus modeling features are explained and lastly the different crack cases used in the benchmark analysis are presented together with their closed-form solutions.

2.1 Linear elastic fracture mechanics

The key in fracture mechanics is to capture the behavior occurring at the crack tip. One classical and important approach in this area used throughout in this work, is the Linear Elastic Fracture Mechanics (LEFM) theory [8]. In this approach, the large stress effect at the crack tip is approximated as an ideal elastic crack with theoretically infinite stresses at the tip. These stress fields are related to an engineering measure in the LEFM concept; the Stress Intensity Factors (SIF). The basics of these concepts and related problems are covered in this section.

2.1.1 Crack approximation

Cracks subjected to loads respond in the same manner as a notch in a material, namely as stress raisers. Due to the sharp configuration at the tip, the crack creates severe concentrations of stress at the tip. This behavior is shown in Figure 2.1 for a real crack (solid line). Related to this behavior is also the creation of a plastic zone in the vicinity of the tip, due to plasticity in the material from the high stresses. Using the LEFM concept, the plasticity behavior is not accounted for and the stress field is approximated from an ideal crack following linear elasticity, shown in Figure 2.1 by a dashed line. Consequently, the LEFM concept includes a large flaw in this manner related to reality. But to overcome this problematic assumption, limitations exist on the size of the plastic zone where the ideal crack can be guaranteed to show the same behavior as the real crack [8]. These limitations are not checked in this work since only comparisons between different linear elastic models are done.

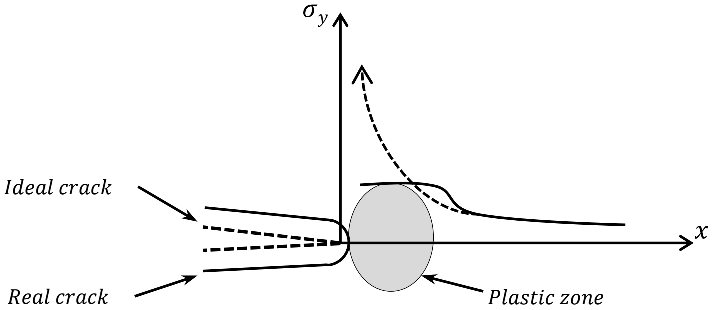

Figure 2.1: Stress behavior for an ideal and real crack.

2.1.2 Stress intensity factors

The stress intensity factors are used for the expression of the stress field at a crack tip and serve as a measure of the severity of the crack tip for different crack configurations. They have a central role in crack assessment, where they can be related to critical levels of stresses resulting in crack growth and eventually fracture.

There are three independent loading modes used in fracture mechanics; Mode I, II and III. They can be seen in Figure 2.2 a-c. Mode I is the crack opening mode where the crack surfaces move apart and is the most common load type. The Mode II is an in-plane shear mode where the crack surfaces slide apart perpendicular to the crack. Mode III is an out-of-plane shear mode where the crack surfaces slide apart in a tearing manner.

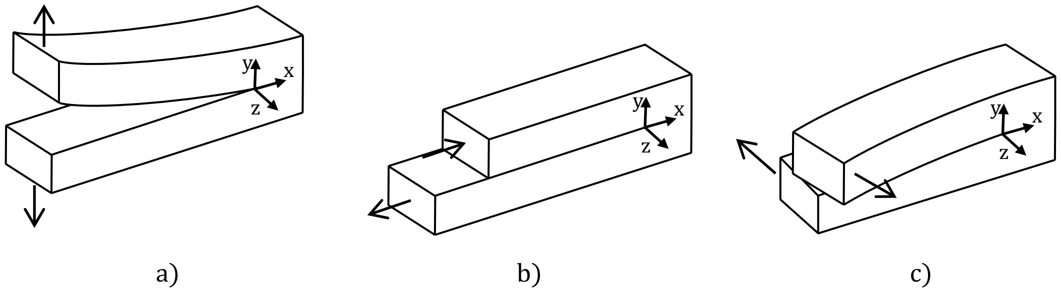

a) b) c)

Figure 2.2: The three loading modes. a) Mode I, b) Mode II, c) Mode III.

The solution of the elastic stress field near the crack tip is defined as

$$\boldsymbol{\sigma} = K_I \boldsymbol{f}_I(r, \alpha) + K_{II} \boldsymbol{f}_{II}(r, \alpha) + K_{III} \boldsymbol{f}_{III}(r, \alpha) + \boldsymbol{\sigma}_0 \tag{2.1}$$

where K_I, K_{II} and K_{III} are the stress intensity factors for the respective mode, $\boldsymbol{\sigma}_0$ is a finite stress, r is the distance from the crack tip and α is the angle from the crack tip. A schematic definition of the stress field, radial distance and angle can be seen in in Figure 2.3. $\boldsymbol{f}_I$, $\boldsymbol{f}_{II}$ and $\boldsymbol{f}_{III}$ are proportional to $1/\sqrt{r}$, for example

$$(\boldsymbol{f}_I)_{xx} = \frac{1}{\sqrt{2\pi r}} \cos\left(\frac{\alpha}{2}\right)\left(1 - \sin\left(\frac{\alpha}{2}\right)\sin\left(\frac{3\alpha}{2}\right)\right) \tag{2.2}$$

which makes the term singular as $r \to 0$. The other terms have a similar form. For the total analytical expressions, cf. [9]. Hence at the crack tip, i.e. $r \to 0$, σ_y becomes infinite according the ideal crack approximation in LEFM (cf. Section 2.1.1).

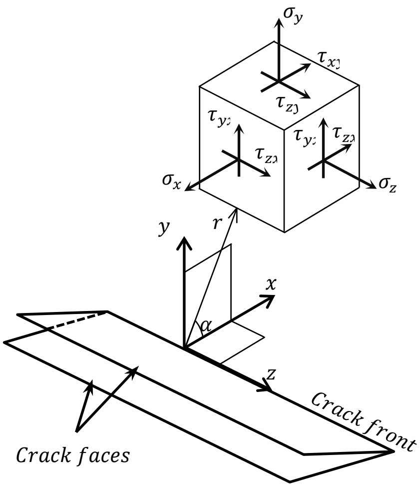

Figure 2.3: A three-dimensional coordinate system describing the stresses near the crack front.

The stress intensity factors for the three modes are defined as

$$K_I = \lim_{r \to 0} \sqrt{2\pi r}\sigma_{yy}(r,0) \tag{2.3}$$

$$K_{II} = \lim_{r \to 0} \sqrt{2\pi r}\sigma_{yx}(r,0) \tag{2.4}$$

$$K_{III} = \lim_{r \to 0} \sqrt{2\pi r}\sigma_{yz}(r,0) \tag{2.5}$$

where σ_{ij} is the stress/shear in the particular direction.

2.1.3 Contour integral evaluation

The stress intensity factors can be calculated from the J-integral with the so called interaction integral method [10]. The J-integral is a contour integral method to calculate the strain energy release rate, the energy dissipated during fracture per unit created fracture surface area [11]. This measure is also important in fracture mechanics since the energy can be related to crack growth. The interaction integral method is an extension of the J-integral, where the J-integral is calculated for pure modes. Hence, the calculation of the J-integral for a three dimensional crack front is first described in Section 2.1.3.1 and is then extended with the interaction integral method to extract the stress intensity factors in Section 2.1.3.2.

2.1.3.1 J-integral

The J-integral is originally defined for a contour integral in two dimensions (see Figure 2.4a). This can then be extended to three dimensions which is used in the interaction integral method to extract the stress intensity factors.

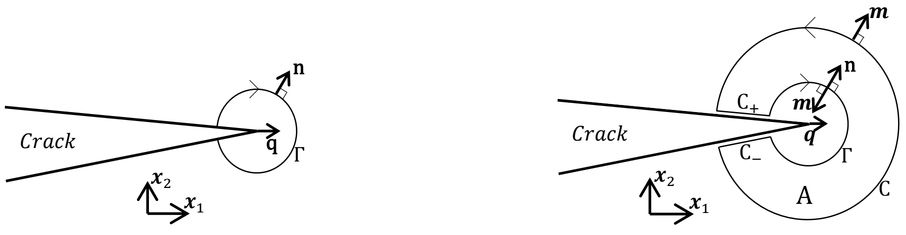

a) b)

Figure 2.4: a) A 2D contour integral and b) a 2D closed contour integral.

Starting with the two dimensional J-integral, it is defined for a quasi-static analysis as [10]

$$J = \lim_{\Gamma \to 0} \int_{\Gamma} \boldsymbol{n} \cdot \boldsymbol{H} \cdot \boldsymbol{q} \, d\Gamma \tag{2.6}$$

where Γ is the contour around the crack tip, $d\Gamma$ is the arc increment on Γ, $\boldsymbol{n}$ is the outwards pointing normal of the contour, $\boldsymbol{q}$ is the unit vector in the virtual crack extension direction. $\boldsymbol{H}$ is defined according to

$$\boldsymbol{H} = W\boldsymbol{I} - \boldsymbol{\sigma} \cdot \frac{\partial \boldsymbol{u}}{\partial \boldsymbol{x}} \tag{2.7}$$

where W is the elastic strain energy, $\boldsymbol{I}$ is the identity tensor, $\boldsymbol{\sigma}$ is the Cauchy stress tensor and $\boldsymbol{u}$ the displacement vector. The strain energy can be extended to include elasto-plastic material response, but in this work only elasticity is considered.

The contour Γ is connected with the two crack faces and encloses the crack tip. This is shown schematically in Figure 2.4a. The contour is reduced so that it only includes the crack tip ($\Gamma \rightarrow 0$ in (2.6)). The outwards pointing normal $\boldsymbol{n}$ is located along the whole contour and the unit vector in the virtual crack extension direction $\boldsymbol{q}$ is located at the crack tip. It should be noted that the J-integral is path-independent for elastic material in the absence of body forces and tractions on the crack surfaces [10]. This means that the contour does not have to be shrunk onto the crack tip but can be specified anywhere where it encloses the crack tip.

The regular 2D contour integral can be rewritten to a 2D closed contour integral [10]

$$J = \oint_{C + C_+ + \Gamma + C_-} \boldsymbol{m} \cdot \boldsymbol{H} \cdot \bar{\boldsymbol{q}} \, d\Gamma - \int_{C_+ + C_-} \boldsymbol{t} \cdot \frac{\partial \boldsymbol{u}}{\partial \boldsymbol{x}} \cdot \bar{\boldsymbol{q}} \, d\Gamma \tag{2.8}$$

where integral segments are defined as a closed contour that is extended from Γ, see Figure 2.4b. The contour remains the same, C_+ and C_- are contours along the crack faces respectively and C encloses the contour from C_+ and C_- over the crack tip. The unit normal $\boldsymbol{m}$ has been introduced here instead as the outwards-pointing normal at C, meaning that for Γ the normal $\boldsymbol{m} = -\boldsymbol{n}$. Here also the weighting function $\bar{\boldsymbol{q}}$ has been introduced as the unit vector in the virtual crack extension direction, $\bar{\boldsymbol{q}} = \boldsymbol{q}$**,** on Γ and vanishing on C, $\bar{\boldsymbol{q}} = 0$. Requirement also exists that it is sufficiently smooth in the domain enclosed by the contour. In equation (2.8), $\boldsymbol{t}$ is the traction on the crack surfaces, $\boldsymbol{t} = \boldsymbol{m} \cdot \boldsymbol{\sigma}$. Traction on the crack surfaces is not regarded in this work and therefore the second term in the J-integral is disregarded from here on.

The J-integral can now be transformed to a domain integral with the divergence theorem [10]

$$J = \int_A \left(\frac{\partial}{\partial \boldsymbol{x}}\right) \cdot (\boldsymbol{H} \cdot \overline{\boldsymbol{q}})\ dA \tag{2.9}$$

where A is the area domain enclosed by the closed contour, and dA the infinitesimal area segment.

Introducing the equilibrium equation,

$$\left(\frac{\partial}{\partial \boldsymbol{x}}\right) \cdot \boldsymbol{\sigma} + \boldsymbol{f} = \boldsymbol{0} \tag{2.10}$$

and the gradient of the strain energy for a homogenous material with constant material parameters,

$$\frac{\partial W(\boldsymbol{\epsilon}^m)}{\partial \boldsymbol{x}} = \frac{\partial W}{\partial \boldsymbol{\epsilon}^m} : \frac{\partial \boldsymbol{\epsilon}^m}{\partial \boldsymbol{x}} = \boldsymbol{\sigma} : \frac{\partial \boldsymbol{\epsilon}}{\partial \boldsymbol{x}} \tag{2.11}$$

the 2D J-integral can be rewritten to its final form [10]

$$J = -\int_A \left[\boldsymbol{H} : \frac{\partial \overline{\boldsymbol{q}}}{\partial \boldsymbol{x}} + \left(\boldsymbol{f} \cdot \frac{\partial \boldsymbol{u}}{\partial \boldsymbol{x}}\right) \cdot \overline{\boldsymbol{q}}\right] dV \tag{2.12}$$

where $\boldsymbol{\epsilon}^m$ is the mechanical strain and $\boldsymbol{f}$ is the body force per unit volume. Thermal influence is neglected here.

The two dimensional J-integral (eq. (2.6)) can be extended to a three dimensional crack front where the J-integral is defined point-wise with respect to a parametric variable s along the crack front, $J(s)$, seen in Figure 2.5a [10]. The three dimensional calculations are performed in a similar manner as the two dimensional case, but the energy release rate is initially calculated with respect to a finite segment of the crack advance of the crack front, denoted $\bar{J}$. This is then used to obtain the point-wise energy release rate $J(s)$ for each node set along the crack tip.

This procedure is done by defining a parametric variable s along the crack front with a local coordinate system. The local Cartesian coordinate system is set up at the crack front with respect to s, see Figure 2.5a. The axis, x_3, runs tangentially to the crack, x_2 is defined perpendicular to the crack plane, and x_1 normal to the crack front. In this formulation x_1 will always be directed forward at the crack front and parallel to the crack plane coinciding with the crack front extension for a straight propagation of the crack. Furthermore, x_1 together with x_2 spans a plane perpendicular to the crack front. Hence, $J(s)$ is described in the x_1x_2-plane.

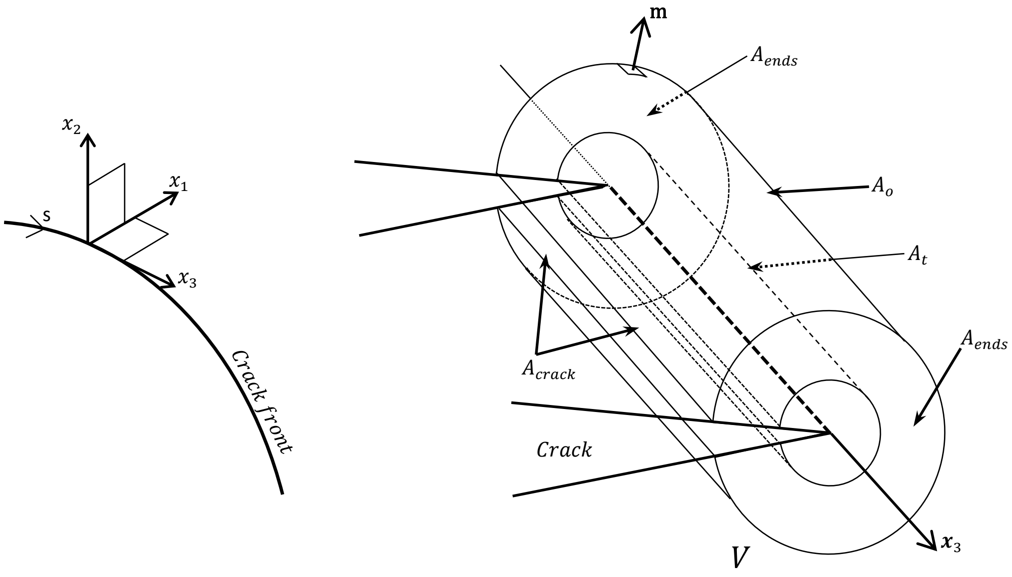

a) b)

Figure 2.5: a) Local coordinate system for $\boldsymbol{s}$. b) Contour integral for general 3D crack front.

In three dimensions, the energy release for a unit segment of crack advance over a finite segment of the crack front, $\bar{J}$, is defined as [10]

$$\bar{J} = -\int_V \left[\boldsymbol{H} : \frac{\partial \bar{\boldsymbol{q}}}{\partial \boldsymbol{x}} + \left(\boldsymbol{f} \cdot \frac{\partial \boldsymbol{u}}{\partial \boldsymbol{x}} \right) \cdot \bar{\boldsymbol{q}} \right] dV \tag{2.13}$$

where $\boldsymbol{H}$, $\boldsymbol{f}$ and $\boldsymbol{u}$ are defined as before but in three dimensions. The weighting function $\bar{\boldsymbol{q}}$ is here defined for the various surfaces. The point-wise J-integral, $J(s)$, for a general three dimensional crack front is then obtained by dividing with the increase of the crack area due to the crack advance for the finite segment [10]. The area of interest in this work is the calculation domain, therefore are the remaining steps not covered here.

The three dimensional case is a volume integral for the domain V shown in Figure 2.5b. This is a tubular domain for a closed contour along a finite segment of the crack front. The three dimensional surface integral consists of the inner tube surface, A_t,the outer tube surface, A_0, the two surfaces along the crack face, A_{cracks} and lastly the two surfaces at the ends, A_{ends}, in accordance with the closed contour domain. Noting that still $\Gamma \rightarrow 0$ which means that $A_t \rightarrow 0$. The two dimensional area domain along the crack front in the x_1x_2-plane is called contour domain in this report.

2.1.3.2 Stress intensity factor extraction

For isotropic linear elastic materials, the J-integral is related to the stress intensity factors by the following relationship [12]

$$J = \frac{1}{8\pi} \boldsymbol{K}^T \cdot \boldsymbol{B}^{-1} \cdot \boldsymbol{K} \tag{2.14}$$

where $\boldsymbol{K} = [K_I, K_{II}, K_{III}]^T$ and $\mathbf{B}$ is the pre-logarithmic energy factor matrix.

For a homogeneous, isotropic material the equation simplifies to:

$$J = \frac{1}{\bar{E}}(K_I^2 + K_{II}^2) + \frac{1}{2G}K_{III}^2 \tag{2.15}$$

where $\bar{E} = E$ for plane stress and $\bar{E} = \frac{E}{1-\nu^2}$ for plane strain, axisymmetry and three dimensions. Furthermore under pure Mode I loading, the relation between the J-integral and K_I for three dimensions is

$$J_I = K_I^2\left(\frac{1-\nu^2}{E}\right) \tag{2.16}$$

To evaluate mixed-mode stress intensity factors, the interaction integral method can be used. It is an effective way to calculate mixed-mode SIFs in terms of interaction integrals using the J-integral. The interaction integral method uses so called auxiliary fields superimposed on top of the actual fields. The auxiliary field can consist of for example stresses or strains around the crack tip. The J-integral of the actual field is denoted J, the J-integral related to the auxiliary field J_{aux} and the J-integral from the interaction integral J_{int}. These three terms are together defined as the total J-integral J_{tot}^I, i.e. $J_{tot} = J + J_{aux} + J_{int}$. By choosing the auxiliary fields wisely, the interaction integral for Mode α can be expressed as $J_{int}^{\alpha} = J_{tot}^{\alpha} - J_{aux}^{\alpha} - J$, which is used to extract the individual stress intensity factors.

The stress intensity factor extraction for Mode I ($\alpha = I$) is presented here. Expanding equation (2.14), the relation between the J-integral and the stress intensity factors is

$$J = \frac{1}{8\pi}(K_I B_{11}^{-1} K_I + 2K_I B_{12}^{-1} K_{II} + 2K_I B_{13}^{-1} K_{III}) + [terms\ without\ K_I] \tag{2.17}$$

The J-integral for an auxiliary field, Mode I crack tip field with k_I as stress intensity factor, is chosen as

$$J_{aux}^I = \frac{1}{8\pi}(k_I \cdot B_{11}^{-1} \cdot k_I) \tag{2.18}$$

Superposition of the auxiliary field and the real field gives

$$\begin{aligned} J_{tot}^I = \frac{1}{8\pi}([K_I + k_I]B_{11}^{-1}[K_I + k_I] + 2[K_I + k_I]B_{12}^{-1}K_{II} + 2[K_I \\ + k_I]B_{13}^{-1}K_{III}) + [terms\ without\ K_I\ and\ k_I] \end{aligned} \tag{2.19}$$

Since the terms without K_I and k_I are the same for J and J_{tot}^I, the interaction integral can be expressed as

$$J_{int}^I = J_{tot}^I - J_{aux}^I - J = \frac{k_I}{4\pi}(B_{11}^{-1}K_I + B_{12}^{-1}K_{II} + B_{13}^{-1}K_{III}) \tag{2.20}$$

The same procedure is done for Mode II and Mode III. The equations for the three modes can be written as

$$J_{int}^{\alpha} = \frac{k_{\alpha}}{4\pi} B_{\alpha\beta}^{-1} K_{\beta} \tag{2.21}$$

Choosing unit values for k_{α}, the stress intensity factors are expressed in terms of the interaction integral as

$$\boldsymbol{K} = 4\pi \boldsymbol{B} \cdot \boldsymbol{J}_{int} \tag{2.22}$$

where $\boldsymbol{J}_{int} = [J_{int}^{I}, J_{int}^{II}, J_{int}^{III}]^{\mathsf{T}}$. The interaction integral can be evaluated in a similar manner as the J-integral in Section 2.1.3 for the three modes $\alpha = I, II, III$ including auxiliary stress and strain fields:

$$J_{int}^{\alpha} = \lim_{\Gamma \to 0} \int_{\Gamma} \boldsymbol{n} \cdot \boldsymbol{M}^{\alpha} \cdot \boldsymbol{q} \, d\Gamma \tag{2.23}$$

where $\boldsymbol{M}^{\alpha}$ is given as

$$\boldsymbol{M}^{\alpha} = \boldsymbol{\sigma} : \epsilon_{aux}^{\alpha} \boldsymbol{I} - \boldsymbol{\sigma} \cdot \left(\frac{\partial \boldsymbol{u}}{\partial \boldsymbol{x}} \right)_{aux}^{\alpha} - \sigma_{aux}^{\alpha} \cdot \frac{\partial \boldsymbol{u}}{\partial \boldsymbol{x}}$$

where aux denotes the auxiliary pure Mode I, Mode II and Mode III crack tip field for the corresponding Mode α. For the full expression of the analytical terms, see [6].

2.2 FEM model

2.2.1 Governing equations

In this section, the governing equations are presented and the weak form is specified [4], which is the basis of the XFEM extension.

Consider the domain Ω in Figure 2.6. The domain is bounded by the boundary Λ that consists of four sets; Λ_t with a prescribed traction $\bar{t}$, Λ_u with prescribed displacements and two traction-free crack surfaces Λ_c^+ and Λ_c^-.

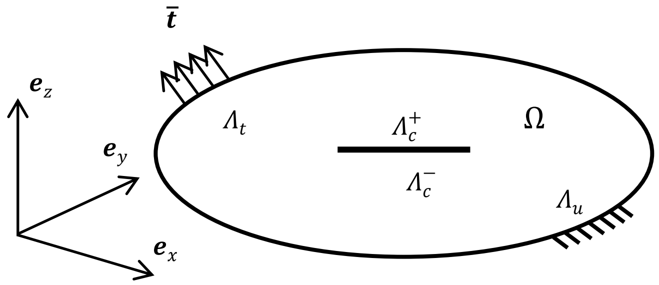

Figure 2.6: A body with a crack with a fixed boundary subjected to a load.

The equilibrium equations and boundary conditions are (for contact-free crack surfaces):

$$\boldsymbol{\nabla}\cdot\boldsymbol{\sigma}+\boldsymbol{b}=\boldsymbol{0} \text{ in } \Omega \tag{2.24a}$$

$$\boldsymbol{\sigma}\cdot\boldsymbol{n}=\bar{\boldsymbol{t}} \text{ on } \Lambda_t \tag{2.24b}$$

$$\boldsymbol{\sigma}\cdot\boldsymbol{n}=\boldsymbol{0} \text{ on } \Lambda_c^+ \tag{2.24c}$$

$$\boldsymbol{\sigma}\cdot\boldsymbol{n}=\boldsymbol{0} \text{ on } \Lambda_c^- \tag{2.24d}$$

$$\boldsymbol{u}=\boldsymbol{u}_{pres} \text{ on } \Lambda_u \tag{2.24e}$$

and the corresponding weak form is

$$\int_\Omega \boldsymbol{\sigma}:(\boldsymbol{\nabla}\delta\boldsymbol{v}) = \int_{\Lambda_\text{t}} \bar{\mathbf{t}}\cdot\delta\boldsymbol{v}d\Gamma + \int_\Omega \boldsymbol{b}\cdot\delta\boldsymbol{v}d\Omega\,. \tag{2.25}$$

which holds for arbitrary test functions $\delta\boldsymbol{v}$**.**

2.2.2 Material model

In the thesis, the work is restricted to linear elastic fracture mechanics. Therefore small elastic strains are considered with an isotropic linear elastic material. As mentioned in Section 1.3, the material model is restricted in the Abaqus XFEM model itself at the present version, 6.11-1. The material response is therefore described with Hooke's law

$$\boldsymbol{\sigma}=\boldsymbol{C}:\boldsymbol{\epsilon} \tag{2.26}$$

where $\boldsymbol{\sigma}$ is the Cauchy stress, $\boldsymbol{C}$ is the fourth-order stiffness tensor and $\boldsymbol{\epsilon}$ is the strain.

2.2.3 Elements

Two different types of 3D elements can be used in Abaqus for XFEM simulations; tetrahedral element and hexahedral element, see Figure 2.7. The tetrahedral elements are available as first (linear) and second (quadratic) order approximations, where the hexahedral elements are restricted to first order in the XFEM model.

The linear tetrahedral element uses a single integration point for the stiffness calculation and the second order element uses four integration points for the stiffness matrix. The full hexahedral element uses eight integration points and the hexahedral element with reduced integration uses one. The first order hexahedral element is denoted C3D8 with full integration and C3D8R with reduced integration in Abaqus. First order tetrahedral element is denoted C3D6 and second order C3D10 (full integration).

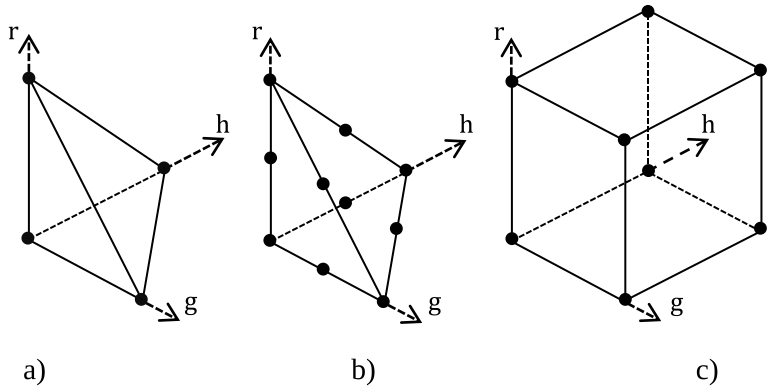

Figure 2.7 Isoparametric elements capable for XFEM. a) First order tetrahedron, b) Second order tetrahedron, c) First order hexahedron.

The geometry of the Abaqus model can be divided into different sections of various shapes, so called partitions. These partitions can be used to specify individual properties, primarily mesh size but also material properties, loads, boundary conditions etcetera. To control a certain refinement of the partitions, mesh sizes are specified on the partition edges.

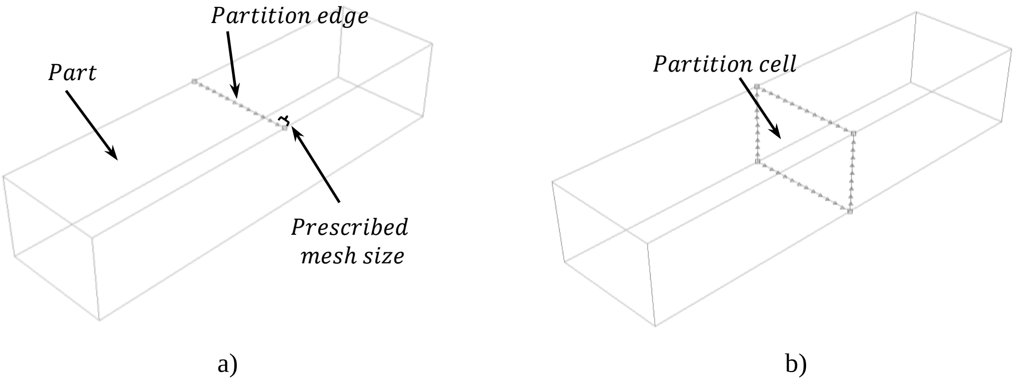

Figure 2.8: a) A part with an edge partition and with prescribed element size. b) A part divided into two by a partition.

2.3 XFEM framework

XFEM is an extension of the conventional finite element method based on the concept of partition of unity [13], i.e. the sum of the shape functions must be unity. It was developed by Ted Belytschko and colleagues in 1999 [14]. Using the partition of unity concept, XFEM adds a priori knowledge about the solution in the finite element space and makes it possible to model discontinuities and singularities independently of the mesh. This makes it a very attractive method to simulate crack propagation since it is not necessary to update the mesh to match the current geometry of the discontinuity and the crack can propagate in a solution-dependent path. In XFEM, enrichment functions connected to additional degrees of freedom are added to the finite element approximation in the region where the crack is located in the mesh to include the discontinuities and singularities. These enrichment functions consist of the asymptotic crack tip functions that capture the singularity at the crack tip and a discontinuous function that represent the gap between the crack surfaces. These functions will be described in more detail below.

2.3.1 XFEM enrichment

To explain how the discontinuous functions are added to the FE approximation, a simple two-dimensional crack is studied [4]. Consider the case of a crack in a mesh with four elements, where the crack is placed on the element boundary, seen in Figure 2.9. The finite element approximation for the mesh is

$$\boldsymbol{u}^h(\boldsymbol{x}) = \sum_{i=1}^{10} N_i(\boldsymbol{x})\boldsymbol{u}_i \tag{2.27}$$

where N_i is the shape function for node i, $\boldsymbol{u}_i$ is the displacement vector at node i and $\boldsymbol{x}$ is the position vector. Define $\boldsymbol{k}$ and $\boldsymbol{l}$ as

$$\boldsymbol{k} = \frac{\boldsymbol{u}_9 + \boldsymbol{u}_{10}}{2}, \quad \boldsymbol{l} = \frac{\boldsymbol{u}_9 - \boldsymbol{u}_{10}}{2} \tag{2.28}$$

i.e. $\boldsymbol{k}$ lie in between $\boldsymbol{u}_9$ and $\boldsymbol{u}_{10}$ and $\boldsymbol{l}$ is half the distance between $\boldsymbol{u}_9$ and $\boldsymbol{u}_{10}$.

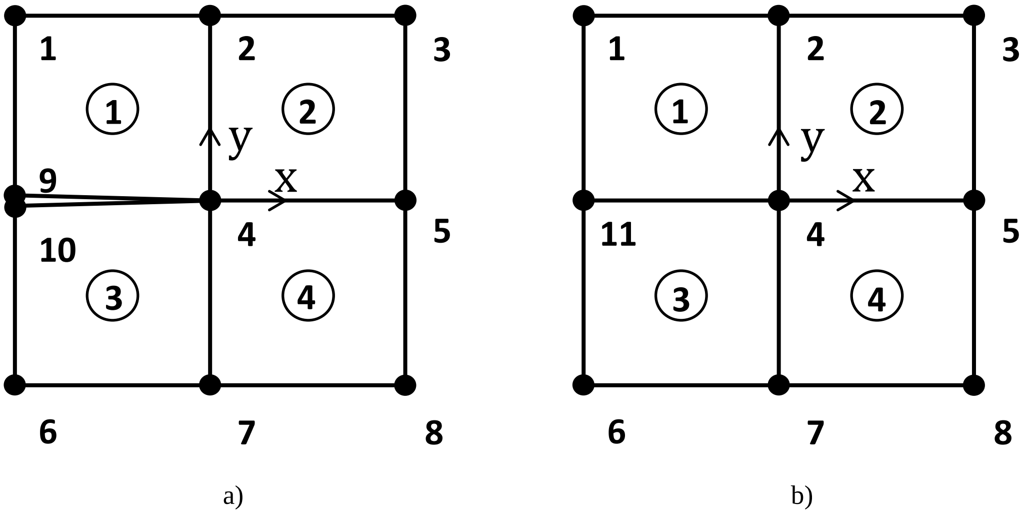

a) b)

Figure 2.9: Mesh with a crack, a), and a mesh without a crack, b). The circled numbers are element numbers.

Now, $\boldsymbol{u}_9$ and $\boldsymbol{u}_{10}$ can be expressed in terms of $\boldsymbol{k}$ and $\boldsymbol{l}$ as

$$\boldsymbol{u}_9 = \boldsymbol{k} + \boldsymbol{l}, \quad \boldsymbol{u}_{10} = \boldsymbol{k} - \boldsymbol{l} \tag{2.29}$$

Adding these expressions into eq. (2.27) yields

$$\boldsymbol{u}^h = \sum_{i=1}^{8} N_i\boldsymbol{u}_i + \boldsymbol{k}(N_9 + N_{10}) + \boldsymbol{l}(N_9 + N_{10})H(\boldsymbol{x}) \tag{2.30}$$

where the discontinuous sign/jump function $H(x)$ is introduced as

$$H(\boldsymbol{x}) = \begin{cases} 1, & y > 0 \\ -1, & y < 0 \end{cases} \tag{2.31}$$

Now, $N_9 + N_{10}$ can be replaced by N_{11} and $\boldsymbol{k}$ by $\boldsymbol{u}_{11}$ and the finite element approximation can be expressed as

$$\boldsymbol{u}^h = \underbrace{\sum_{i=1}^{8} N_i \boldsymbol{u}_i + N_{11}\boldsymbol{u}_{11}}_{Standard\ FE\ approximation} + \underbrace{\boldsymbol{l} N_{11} H(\boldsymbol{x})}_{Discontinous\ enrichment} \tag{2.32}$$

The first two parts on the right-hand side are the standard finite element approximation, and the third part is the additional discontinuous jump enrichment. Equation (2.32) shows that the finite element approximation of a crack in a mesh, as in Figure 2.9a, may be interpreted as a mesh without a crack, as in Figure 2.9b, and an additional discontinuous enrichment. The extension to a crack that is not placed on the element boundary can be described in a similar manner.

To be able to capture the singularity at the crack tip, discontinuous asymptotic crack tip functions are added to the nodes that surround the crack tip [4], as illustrated in Figure 2.10. If the tip does not end at an element boundary, the crack tip functions also describe the discontinuity over the crack surfaces in the element containing the crack tip.

Thus, in total, there are two types of enrichments; the asymptotic crack tip functions to describe the crack tip and the jump function to describe the rest of the crack. The nodes are enriched with the jump function when their supports are fully intersected by a crack whereas the element nodes surrounding the crack tip are enriched with the crack tip functions. The circled nodes are enriched with the jump function and the squared ones are enriched with the crack tip functions.

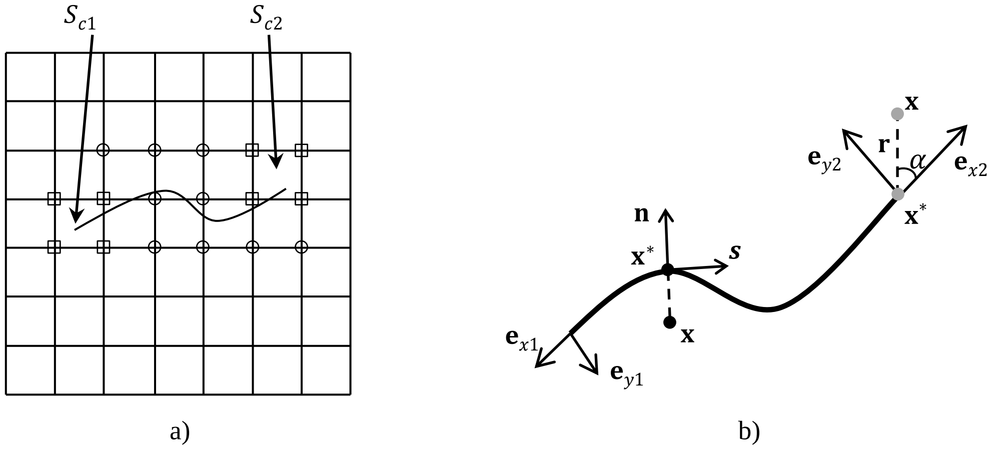

a) b)

Figure 2.10: a) An arbitrary crack in a mesh. b) Local coordinate axes for two crack tips.

With the aid of Figure 2.10, the total formulation of XFEM can now be derived. Let all the nodes in the mesh be defined by the set $\boldsymbol{S}$, the nodes surrounding the crack tip by the set $\boldsymbol{S}_c$ and the nodes whose supports are cut by the crack (excluding the nodes in $\boldsymbol{S}_c$) be defined by $\boldsymbol{S}_h$. The finite element approximation now reads

$$\boldsymbol{u} = \sum_{I \in \boldsymbol{S}} N_I(\boldsymbol{x}) \left[\boldsymbol{u}_I + \underbrace{H(\boldsymbol{x}) \boldsymbol{a}_I}_{I \in \boldsymbol{S}_h} + \underbrace{\sum_{i=1}^{4} \psi_i(\boldsymbol{x}) \boldsymbol{b}_I^i}_{I \in \boldsymbol{S}_c} \right] \tag{2.33}$$

where $\boldsymbol{u}_I$ is the nodal displacement vector, the $\boldsymbol{a}_I$ nodal enriched degree of freedom vector that with the jump function $H(\boldsymbol{x})$ represent the gap between the crack surfaces and $\boldsymbol{b}_I^i$ the nodal enriched degree of freedom vector that with the crack tip functions $\psi_i(\boldsymbol{x})$ represent the crack tip singularity. The jump function for a general crack is defined as [7]

$$H(\boldsymbol{x}) = \begin{cases} 1, & if\ (\boldsymbol{x} - \boldsymbol{x}^*) \cdot \boldsymbol{n} \geq 0 \\ -1, & otherwise \end{cases} \tag{2.34}$$

where $\boldsymbol{x}^*$ is the point on the crack closest to $\boldsymbol{x}$ and $\boldsymbol{n}$ is the outward normal vector at $\boldsymbol{x}^*$.

The crack tip enrichment functions for an isotropic elastic material are [7]

$$\{\psi_i(\boldsymbol{x})\}_{i=1}^{4} = \left(\sqrt{r} \sin\left(\frac{\alpha}{2}\right), \sqrt{r} \cos\left(\frac{\alpha}{2}\right), \sqrt{r} \sin\left(\frac{\alpha}{2}\right) \sin(\alpha), \sqrt{r} \cos\left(\frac{\alpha}{2}\right) \sin(\alpha) \right) \tag{2.35}$$

where (r, α) are the local polar coordinates at the crack tip and $-\pi \leq \alpha \leq \pi$. Together, the terms in (2.35) describe the singularity in the stress field (cf. with analytical stress field solution in (2.1)). In addition, the term $\sqrt{r} \sin\left(\frac{\alpha}{2}\right)$ describes the discontinuity over the crack surfaces in $\boldsymbol{S}_{c1}$:

$$\sqrt{r} \sin\left(\frac{\alpha}{2}\right) = \begin{cases} \sqrt{r}, & if\ \alpha = \pi \\ -\sqrt{r}, & if\ \alpha = -\pi \end{cases} \tag{2.36}$$

where α is 0 rad in the direction of the crack tip and $\alpha = \pi$ at the upper crack surface and $\alpha = -\pi$ at the lower crack surface. For an arbitrary crack with two crack tips, the approximation is

$$\boldsymbol{u} = \sum_{I \in \boldsymbol{S}} N_I(\boldsymbol{x}) \left[\boldsymbol{u}_I + \underbrace{H(\boldsymbol{x}) \boldsymbol{a}_I}_{I \in \boldsymbol{S}_h} + \underbrace{\sum_{i=1}^{4} \psi_i(\boldsymbol{x}) \boldsymbol{b}_I^{i1}}_{I \in \boldsymbol{S}_{c1}} + \underbrace{\sum_{i=1}^{4} \psi_i(\boldsymbol{x}) \boldsymbol{b}_I^{i2}}_{I \in \boldsymbol{S}_{c2}} \right] \tag{2.37}$$

where the set of nodes $\boldsymbol{S}_{c1}$ is for the first crack tip and $\boldsymbol{S}_{c2}$ is for the second crack tip. The functions $\psi_i^1(\boldsymbol{x})$ and $\psi_i^2(\boldsymbol{x})$ are the same but with polar coordinates (r_1, α_1) and (r_2, α_2) respectively, seen in Figure 2.10b.

A complete derivation and definition of the discretized equations are set up according to [5] and [7].

2.4 Benchmarks

To evaluate the performance of XFEM in Abaqus, a stress intensity factor comparison is made against benchmark cases. Five benchmark tests are studied; four are specified in the standard BS 7910 [1] and the last one is specified in *The application of asymptotic solutions to a semi-elliptical crack at the root of a notch* [15], which is referred to as U-notch. The equations used for the evaluation of the stress intensity factors for the different benchmark cases are defined in this section, with denotation B1-B5. These equations are closed-form solutions of a wide range of FE-analyses of the crack cases. The benchmark solutions will also be referred to as closed-form solutions.

For the elliptical cracks, the position along the crack tip is defined by the angle θ as in Figure 2.11.

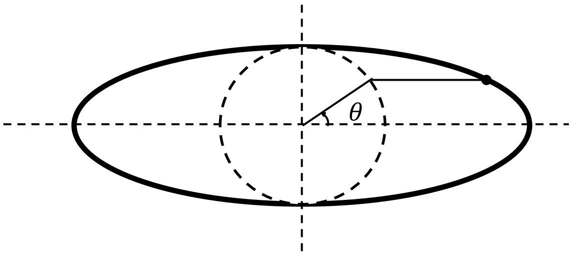

Figure 2.11: The angle θ, describing the position along the crack front, is calculated for a circle with the same radius as the smaller elliptical radius.

2.4.1 Benchmark case 1: B1

The benchmark case B1 is a through-thickness flaw in a plate with geometry given in Figure 2.12. The stress intensity factor is defined as:

$$K_I = M f_w(\frac{a}{W})\, M_m \sigma_\infty \sqrt{\pi a} \tag{2.38}$$

where M is the bulging correction factor, f_w is the geometry correction factor, M_m is a stress intensity magnification factor, σ_∞ is the stress far away from the crack, W is the width of the plate and a is half the crack width [1].

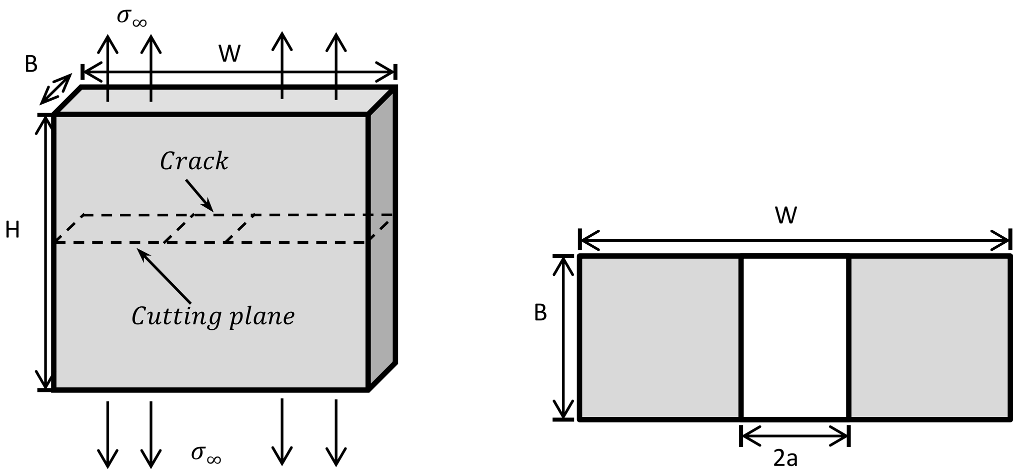

a)

b)

Figure 2.12: Benchmark case B1, a through-thickness flaw in a plate. a) shows the benchmark in 3D and b) shows the benchmark in the cutting plane in 2D.

2.4.2 Benchmark case 2: B2

B2 is a semi-elliptical surface flaw in a plate, see Figure 2.13. The SIF is defined as

$$K_I = M f_w\left(\frac{c}{W}, \frac{a}{B}\right) M_m\left(\frac{a}{B}, \frac{a}{c}, \theta\right) \sigma_\infty \sqrt{\pi a} \tag{2.39}$$

where M is the bulging correction factor, f_w is the geometry correction factor, M_m is a stress intensity magnification factor, σ_∞ is the stress far away from the crack, W is the width of the plate, B is the depth of the plate, a is the crack depth, c is half the crack width and θ is the parametric angle to identify the position along the crack front [1].

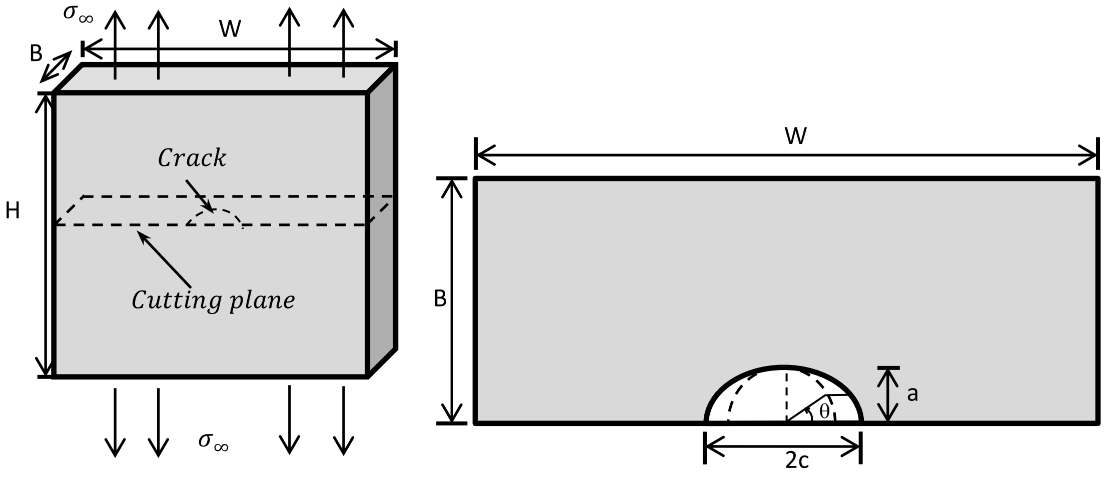

a)

b)

Figure 2.13: Benchmark case B2, a semi-elliptical surface flaw in a plate. a) shows the benchmark in 3D and b) shows the benchmark in the cutting plane in 2D.

2.4.3 Benchmark case 3: B3

This benchmark is an embedded elliptical flaw in a plate. See Figure 2.14 for the definition of the geometry. The stress intensity factor is defined as

$$K_I = M f_w\left(\frac{c}{W}, \frac{a}{B}\right) M_m \left(\frac{a}{B}, \frac{a}{c}, \theta\right) \sigma_\infty \sqrt{\pi a} \tag{2.40}$$

where M is the bulging correction factor, f_w is the geometry correction factor, M_m is a stress intensity magnification factor, σ_∞ is the stress far away from the crack, W is the width of the plate, B is the depth of the plate, a is the crack depth, c is half the crack width and θ is the parametric angle to identify the position along the crack front [1].

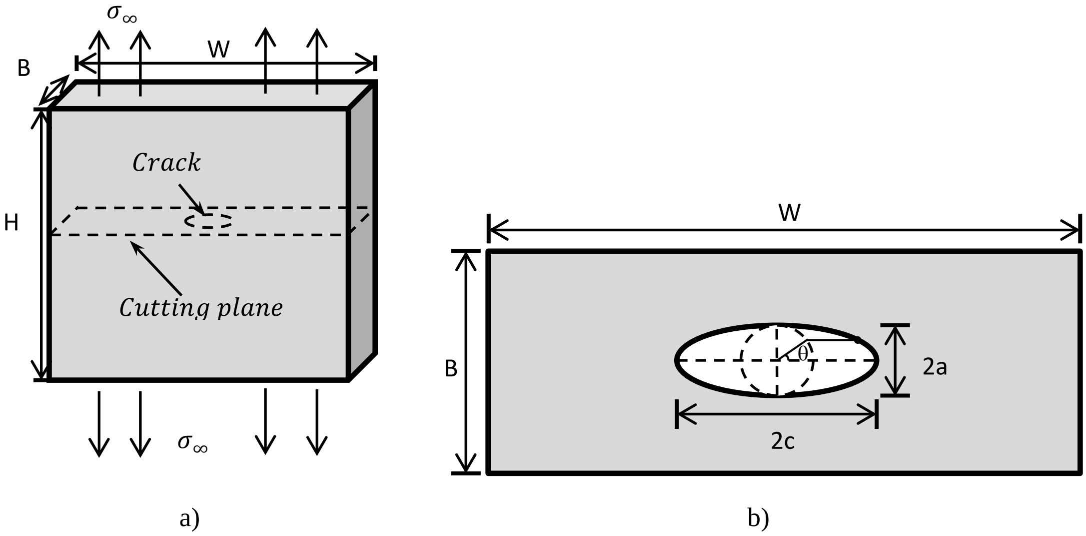

Figure 2.14: Benchmark case B3, an embedded elliptical flaw in a plate. a) shows the benchmark in 3D and b) shows the benchmark in the cutting plane in 2D.

2.4.4 Benchmark case 4: B4

B4 is a plate with two corner cracks in a hole defined in Figure 2.15. The SIF is defined as

$$K_I = M f_w\left(\frac{c}{W}, \frac{a}{B}\right) M_m \left(\frac{a}{B}, \frac{a}{c}, \frac{c}{r}, \theta\right) \sigma_\infty \sqrt{\pi a} \tag{2.41}$$

where M is the bulging correction factor, f_w is the geometry correction factor, M_m is a stress intensity magnification factor, σ_∞ is the stress far away from the crack, W is the width of the plate, B is the depth of the plate, a is the crack depth, c is half the crack width and θ is the parametric angle to identify the position along the crack front [1].

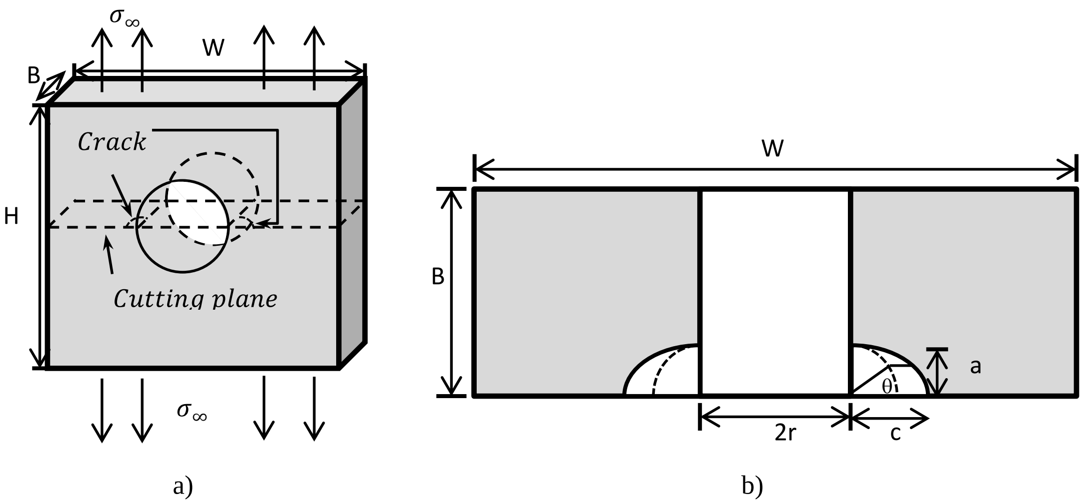

Figure 2.15: Benchmark case B4, finite plate with corner crack(s) at hole. a) shows the benchmark in 3D and b) shows the benchmark in the cutting plane in 2D.

2.4.5 Benchmark case 5: B5

B6 is the benchmark with a crack at the root of a notch, seen in Figure 2.16 and Figure 2.17, referred to as the U-notch. The stress intensity factor for the U-notch is calculated for two points [15]:

$$K_{I,A} = F_A\left(\frac{a}{c},\frac{a}{d}\right)\sigma_\infty\sqrt{\pi a} \tag{2.42}$$

$$K_{I,C} = F_C\left(\frac{a}{c},\frac{a}{d}\right)\sigma_\infty\sqrt{\pi a} \tag{2.43}$$

where A is the deepest point of the crack and C is the surface point.

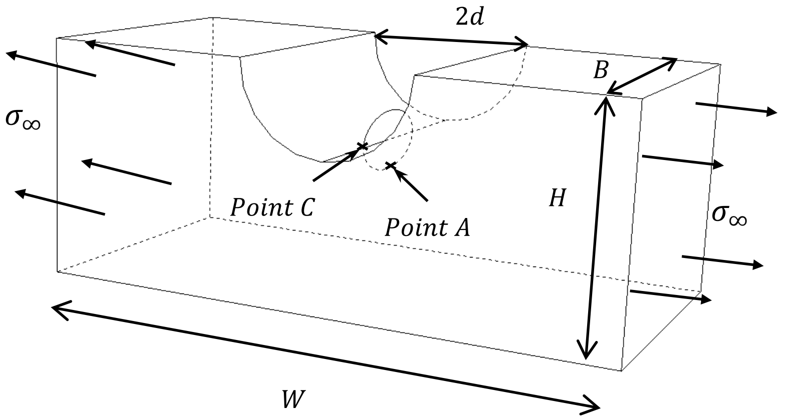

Figure 2.16: A 3D model of the benchmark case B5, a U-notch.

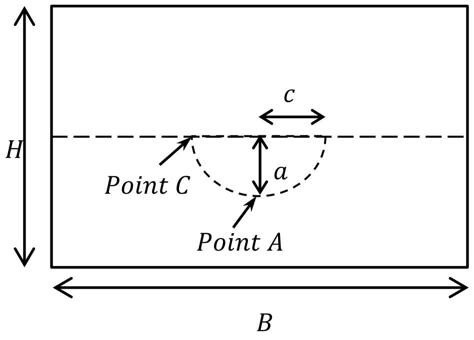

Figure 2.17: The figure shows the dimensions of the crack and the two points where the stress intensity factor is calculated for B5.

3 Method

The evaluation of stationary crack analysis in Abaqus XFEM is performed with a wide range of simulations of the different crack cases defined in Section 2.4. Firstly, a convergence analysis (see Section 3.2) is performed to discover the requirements of the features and parameters in the models to obtain converged results. Secondly, a benchmark analysis (see Section 3.3) is done to investigate the performance of the method. In the convergence analysis, comparisons are done between different models used in the simulations. In the benchmark analysis, comparisons are done between the results from the Abaqus simulations and the closed-form solutions, given in Section 2.4. The most essential results in a stationary crack analysis are the stress intensity factors and they consequently serve as the main parameter in the analyses. The discoveries are then applied in a strategy proposal (see Chapter 5) to aid the current standards methodology for subsea equipment.

In Section 3.1, the basic concepts of XFEM modeling in Abaqus for stationary cracks are defined and explained. The central parameters and techniques used in the convergence and benchmark analyses are also outlined together with the procedure used to evaluate the stationary cracks and perform comparisons.

The convergence analysis consists of two parts; a mesh technique study and a model simplification study. The mesh technique study consists of various investigations to see how different meshes and parameters affect the results in order to find a robust method to model cracks. In the model simplification study, the submodeling technique is evaluated as well as a symmetry investigation. The studies are devoted to find limits/rules where the results can be assured to be accurate. The crack cases studied in the convergence analysis are the crack specimens according to benchmark cases B1, B2 and B3. The results from the convergence analysis are then utilized in the benchmark analysis. Here all crack cases are studied with respect to crack dimensions and accuracy. The convergence and benchmark analyses are fully defined in Chapter 4 where the results are also presented together with a discussion.

Throughout the analyses, material properties and loads are chosen generically with the same parameters. The elastic modulus has no effect on the results since the stress intensity factors are related only to the geometric configuration and the applied load (cf. Section 2.1.2). In the same way, dimensions are specified in meters to ease the modeling process, since the effects from the geometric relations are of interest rather than the magnitude of the SIFs.

3.1 XFEM modeling

The basic concepts covered here are the XFEM model together with the construction of the contour integral for SIF calculation, meshing techniques, simplification techniques and post-processing procedures. Two different meshing techniques used in the analyses are outlined; *high end analysis* and *low end analysis* where accuracy is focused in the former and meshing flexibility in the latter.

3.1.1 Model

This section explains the different features and parameters that are used for stationary cracks in Abaqus and how they are handled in the FE model.

To be able to compute stationary cracks using XFEM in Abaqus, a few simple steps are needed; a crack must be defined, the crack domain must be chosen, the enrichment radius is defined and the output of interest is specified. These steps are explained below according to Abaqus 6.11 Online Documentation [6].

The crack is created as a *shell* surface for 3D cases and positioned as desired. Abaqus automatically finds the positioning of the crack in the solid model using the Level set method. The Level set method defines the crack using isoplanes; ϕ defines the crack face and ψ defines the crack front and is orthogonal to ϕ. The isoplane ϕ is called *PHILSM* in Abaqus and needs to be selected in the *Field output requests* to be able to visualize the crack opening in the post-process.

The *crack domain* defines where the enrichment features can be added to the finite element approximation, i.e. the region where a crack can be described with XFEM. It is specified manually and for stationary crack analyses it must contain any existing crack.

The *enrichment radius* is a radius from the crack tip and defines in which element nodes the crack tip functions are added. It can be manually chosen or Abaqus calculates the radius as three times the typical element characteristic length. This characteristic length is a typical length of a line across an element. The radius is chosen to be calculated automatically in all models presented in the stationary crack evaluation.

The last step is to specify the *number of contours* to be included in the contour domain to calculate the stress intensity factors. The parameter controls the number of element rings around the crack tip that construct the contour domains for the contour integral calculation (see Section 2.1.3). This is specified in *History output requests*.

The contour integral calculation is the most important aspect in stationary crack analysis since it gives the measure to assess critical crack size. The stress intensity factors in Abaqus are calculated along the crack front for a finite number of positions, so called contour integral evaluation points. These points are chosen automatically by Abaqus where the crack front intersects the element boundaries. At these points, the SIFs are calculated according to the contour integral procedure in Section 2.1.3. The contour domain for the volume integral is constructed from rings of elements around the element containing the crack tip, called the crack tip element. The element rings completely surround the crack tip element from one crack face to the other. A schematic description of the element rings in Abaqus can be seen in Figure 3.1, where a cut in the mesh perpendicular to the crack front is shown.

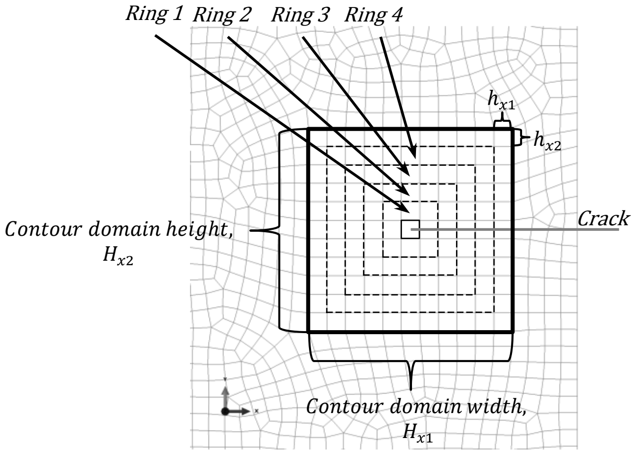

Figure 3.1: In the figure, the contour domain is presented. The four element rings are pointed out as well as the total contour domain height and width.

Several contour integral calculations are performed at each evaluation point for all specified element rings. The first partial contour domain is the elements surrounding the crack tip element. The next partial contour domain contains the first domain and the next element ring directly connected to the first contour domain. Each subsequent contour domain is built up by adding the next element ring to the previous contour domain.

If the *number of contours* is chosen as 5, the SIF is first calculated with a contour domain of one element ring, then two element rings and so on up to five element rings. So the size of the total contour domain is determined by the number of element rings (i.e. *number of contours*) that are included in the calculations of the contour integral.

Theoretically, the contour integral calculation is independent of the size of the contour domain as long as the crack faces are parallel. But because of the approximation with a finite element solution, the SIF for the different element rings will vary and should converge as the domain is increased. Therefore the first few element rings are usually discarded in the analyses because of their large deviation.

3.1.2 Tie constraint

A tie constraint connects two surfaces with mismatched meshes, i.e. different mesh sizes and element types. It constrains each node on the slave surface to have the same displacement/stress as the closest node on the master surface. For best accuracy the master surface should be chosen as the surface with the coarser mesh [6].

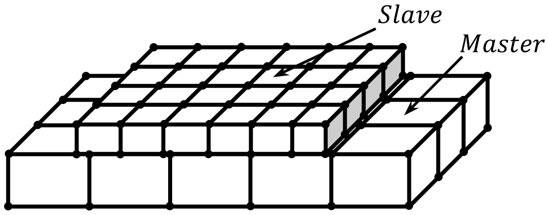

Figure 3.2: The figure shows a mesh using tie constraints. The coarser mesh is the master surface and the finer mesh is the slave surface.

3.1.3 Mesh techniques

Two mesh techniques are used in this work; high end analysis and low end analysis. In this section these two are explained and the corresponding mesh parameters are defined. The crack cases of B1 and B2 together with hexahedral elements will serve as schematic descriptions of the approaches.

3.1.3.1 High end analysis

The so called high end analysis is an analysis where the mesh is heavy refined and conformed at the crack tip. This method makes the mesh structured around the crack tip and element boundaries perpendicular to the crack front (i.e. in the x_1x_2-plane). This is thought to minimize the risk of numerical errors, since the information used in the contour domain is fully described in the x_1x_2-plane, where the contour domain is constructed. A non-perpendicular mesh could introduce a problem where the information in the singularity field is described by nodes not in line with the contour plane, meaning that the information gets interpolated where large deformation gradients exist (crack tip region). Essential in this analysis is that it enables a finer mesh at the crack front without the need to refine the whole crack region.

Presented in Figure 3.3 is a model for high end analysis for a straight crack. This will serve as a schematic description of the mesh procedure where the corresponding parameters in the model are defined. Used here is the through-thickness crack according to benchmark case B1, where symmetry is used so that only the left half of the specimen is shown. The model is divided into three partitions with different mesh sizes; crack tip partition, crack partition and global partition. The crack tip partition structures the mesh and defines the mesh size around the whole crack tip, the crack partition is the domain responsible for mesh size of the crack region, and the remaining partition, the global, controls the general/overall mesh size. Essential in this aspect is that the crack tip partition follows the crack front uniformly, which is not seen in Figure 3.3. This will be shown more in detail for an elliptical crack.

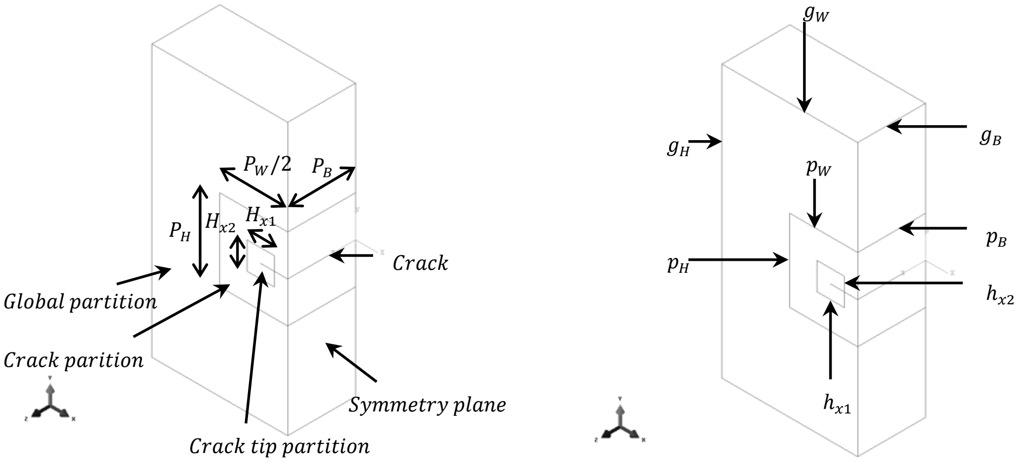

a) b)

Figure 3.3: A schematic description of the high end analysis for benchmark case B1 with the respective partition dimensions and mesh sizes. Note the symmetry plane shown in a).

Following Figure 3.3 the partition dimensions and mesh sizes are introduced with the use of subscripts, according to the dimensions in the benchmark cases (Section 2.4). The subscript W defines the width-direction, H the height-direction and B the depth-direction. The uppercase letters defines the partition dimension, whereas the lowercase letters define the respective partition mesh size. The uppercase letters P_w, P_H and P_B stand for the crack partition dimensions in width, height and depth direction respectively. H_{x1}, H_{x2} and H_{x3} stand for the crack tip partition dimensions in the similar way as before, but in accordance with the local coordinate system along the crack front x_1, x_2 and x_3 (see Figure 2.5a). Related to these partition dimensions are crack mesh sizes p and crack tip mesh sizes h with the same subscript notations for directions. Additionally the remaining global partition G has global mesh sizes g defined with the W, H and B directions.

For elliptical cracks, the partitions are a bit different. The crack partition, seen in Figure 3.4, is defined with the new dimensions El_A, El_C and El_{height} and the new mesh sizes el_{tang} and el_{height}. El_A and El_C are the radii of the semi-elliptical cylinder whereas El_{height} is the height. el_{tang} is the mesh size along the semi-ellipse and el_{height} is the mesh size in the height-direction. The procedure and parameters are equivalent for fully elliptical cracks.

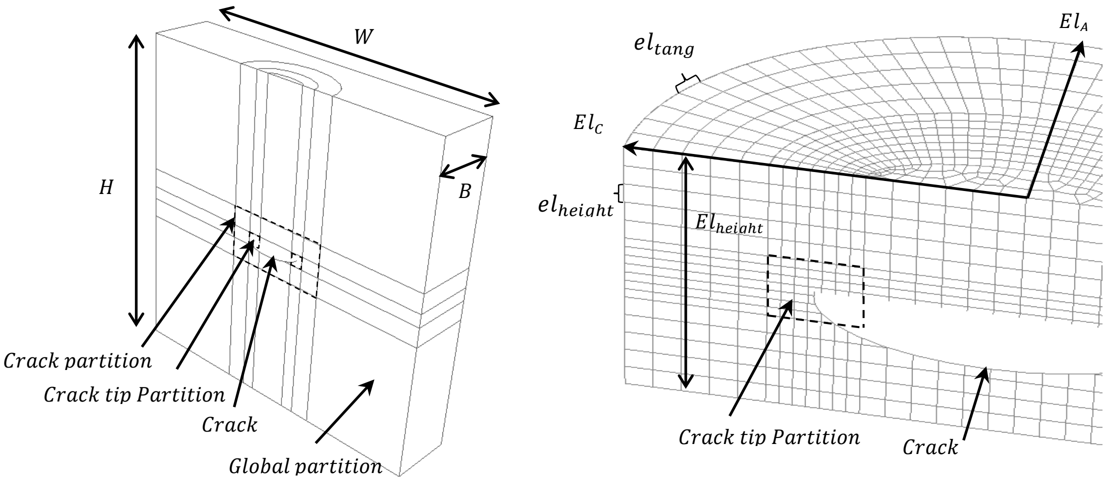

a) b)

Figure 3.4: The high end analysis partition in a) and the crack partition mesh with the new parameters in b).

The Figure 3.5 shows a crack tip partition and its mesh size for a semi-elliptical crack. In Figure 3.5a, the contour domain for 0° coincides with x_1 and x_2. The inner circle of the crack tip partition in Figure 3.5b has a slightly smaller mesh size than the outer circle since it has a shorter length. So the mesh size h_{x3} in the tangential x_3-direction is taken as the average of the inner and outer circle.

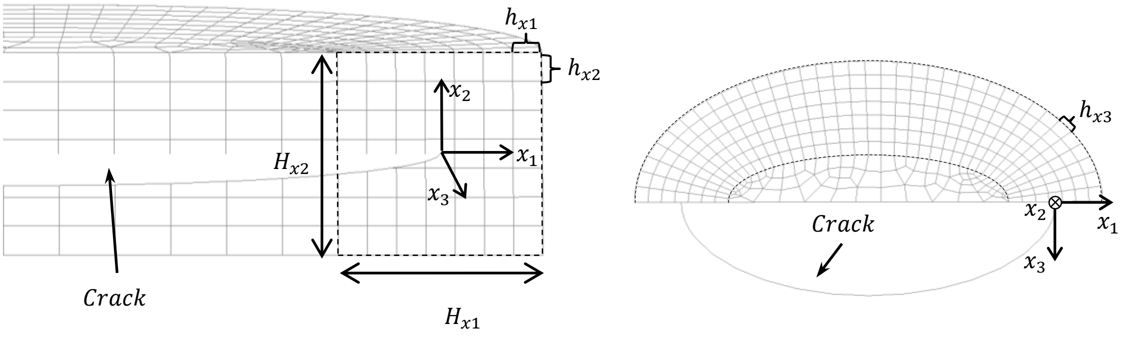

a) b)

Figure 3.5: In the figure, the crack tip partitions are visualized for an elliptical crack.

Consequently in the high end meshing technique the contour domain is conformed around the crack front (in the crack tip partition), as seen in Figure 3.5. The contour domain becomes the element rings around the element containing the crack tip. The first and the second rings are shown in Figure 3.6. The total contour domain (H_{x1}, H_{x2}) is specified as the crack tip partition by choosing the highest number of element rings included. In this way, the contour integral volume domain coincides with the crack tip partition for each evaluation point along the crack front.

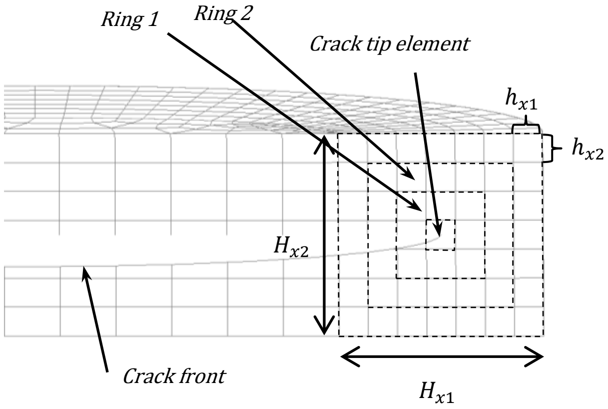

Figure 3.6: The contour domain is visualized and is chosen as the crack tip partition by specifying the number of included element rings.

3.1.3.2 Low end analysis

For more complex geometries than a plate or a box, it might be cumbersome to force the mesh to follow the crack front. Therefore, it is of interest to investigate a more simple mesh that is unstructured and does not follow the crack tip. An analysis with this type of mesh is called a low end analysis. This technique is also connected to the objective with flexible crack modeling for XFEM, since the high end analysis is bounded to a certain crack and specimen boundary and is time consuming and hard to achieve. The low end mesh approach focuses on constructing a relatively simple mesh around the whole crack region. But consequently, the number of elements in the model will increase faster for mesh refinement of the crack since a larger region has to be refined (i.e. not only the crack tip region). The main advantages with this approach are an easy mesh construction and that the crack placement can be varied within this domain. The free placement of cracks is one of main advantages of XFEM, so this approach is very interesting from a practical modeling aspect.

Compared to the high end analysis, where three partitions are made with different complexity, the modeling of the low end analysis is relatively simple. The crack tip partition H is skipped and the crack partition is kept to refine the mesh around the whole crack, seen in Figure 3.7. Hence, the crack partition dimensions (P), crack partition mesh sizes (p) and the global mesh size (g) remains. The contour domain size is still an important aspect and the number of element rings is chosen so that they are inside the crack partition, where the mesh size is controlled. In the same way a certain contour domain size can be specified by choosing the number of element rings to include.

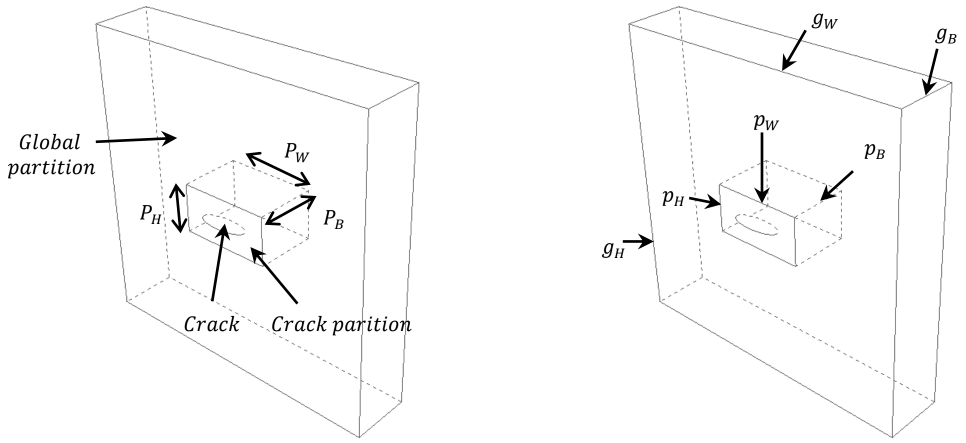

a) b)

Figure 3.7: The partition definitions and partition mesh sizes for a low end analysis of a semi-elliptical crack.

3.1.4 Model simplification techniques

3.1.4.1 Submodeling

Submodeling is a technique to study a certain area of interest in a model with a refined mesh to obtain more accurate and detailed solutions [6]. The technique is very advantageous to use on complex geometries where difficulties exist to refine a certain part of the model.

In an Abaqus submodel analysis, the full model is separated in two separate models; a global model and a submodel (see Figure 3.8). The global model contains the total geometry and loads/boundary conditions. Special features which are the target of investigation in the submodel, such as cracks, are excluded here. The submodel is specified as an arbitrary cut-out from the full model, including the special features and the global model and submodel emanate from the original coordinate system.

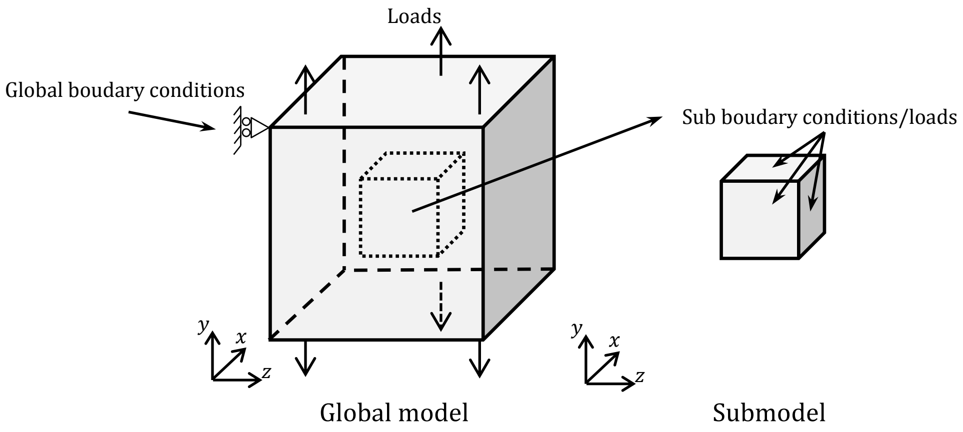

Figure 3.8: Schematic figure of the global model and corresponding submodel.

The global model is solved first to obtain the specimen response due to the applied loadings and boundary conditions. In the submodel analysis, the solution from the global model is then interpolated to the surfaces with appropriate interpolation functions. Now the submodel can be solved separately, with the applied response from the global model.

The connection between the two models is defined at the intersecting surfaces through boundary conditions. Two approaches exist in Abaqus for these connections; node-based connection and surface-based connection. In the node-based connection, the displacements are interpolated and in the surface-based connection, the stresses are interpolated. For further information about the actual interpolation procedure, the reader is advised to the *Abaqus 6.11 online documentation* [6].

In the context of submodeling in practice, the relation between global model and submodel dimensions must be thoroughly investigated for all cases, particularly for high loads. The requirement of the technique is that the submodel is large enough to not create any significant variations of the stress/strain field in the intersecting surface region. The nodal connection generally gives more accurate results for a load-controlled environment in the full model [6]. Additional deviation in the results can also occur where changes in stiffness take place in the submodel. Therefore, particular consideration has to be taken for crack analysis, where a weakening in the material is introduced.

3.1.5 Post-processing procedure

In this section, the procedure to handle the output from the simulations is covered. The various outputs have to be evaluated individually with respect to the different crack configurations. Important aspects here are to estimate SIFs from the different contour domains at the evaluation points, and to evaluate the convergence with respect to the element rings.

From the stationary crack analyses, the outputs are calculated at each evaluation point along the crack front. For each evaluation point, the SIFs are given for all numbers of included element rings in the contour integrals.

The SIFs are non-dimensionalized with the applied load and crack length to give results within a similar range for all analyses. Dimensions specified in the thesis are also non-dimensionalized. The SIF output for each evaluation point is post-processed with respect to the specific crack configuration. The evaluation is divided into two procedures, one for straight cracks and one for elliptical cracks.

3.1.5.1 Non-dimensional normalization

In the results presented, the SIF is non-dimensional normalized with the applied load, σ_∞, and crack length a as

$$K_I^{non-dim} = K_I/(\sigma_\infty\sqrt{\pi a})$$

where K_I is the stress intensity factor with the conventional dimension $[MPa \cdot m^{0.5}]$.

Dimensions (geometric) and mesh sizes in the analyses are non-dimensional normalized with the crack length, a:

$$x^{non-dim} = x/a$$

where x is the dimension (geometric) or the element size with the dimension $[m]$. From here on in the report, all values are treated as non-dimensional if not specified elsewise and the notation $non\text{-}dim$ is skipped throughout.

3.1.5.2 Straight cracks

As described in Section 3.1.1, at each contour evaluation point, the output of the SIFs is given with respect to the element rings. An example of output of K_I with respect to element rings is visualized in Figure 3.9a. The notation $ring$ specifies the number of element rings in the each contour integral calculation and $K_{I,ring}$ the calculated K_I for the corresponding contour integral calculation.

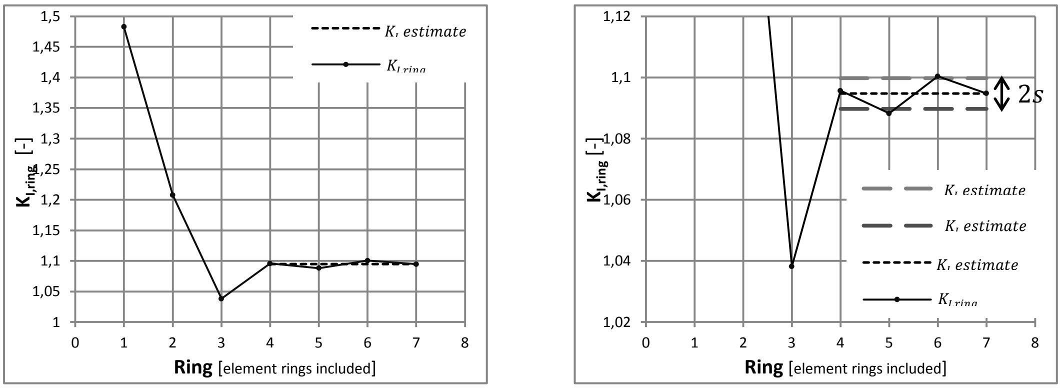

a) b)

Figure 3.9 An example of SIF output for one evaluation point, with respect to element rings. Figure a) shows the output of K_I and the estimation of K_I, figure b) shows estimated K_I and the corresponding standard deviation s. Excluded rings, $n = 3$. Total number of rings, $N = 7$.

For each evaluation point, the following data is estimated:

- K_I, normalized estimation of SIF Mode I
- s_{rel}, relative SIF standard deviation with respect to the element rings.
- ϵ_{rel}, relative SIF error with respect to the reference solution.

It should be noted that only the evaluation point in the middle of the crack front is regarded in the report for straight cracks if not specified otherwise.

The estimation of K_I is performed from $K_{I,ring}$ with respect to element rings according to:

$$K_I = \frac{1}{N-n} \sum_{ring=n+1}^{N} K_{I,ring}$$

where n is the excluded number of rings and N is the total number of rings in the contour integral. The SIF is estimated as the average value, where the first element rings n deviating too much are manually excluded, cf. Figure 3.9. The reason the SIF is estimated in this way is that the convergence with respect to the number of element rings is not perfect, but rather oscillating with numerical variations.

The standard deviation is calculated to evaluate how much the output is oscillating and is thereby a measure of convergence. The relative SIF standard deviation is calculated according to

$$s_{rel} = s/K_I$$

where s is the standard deviation of $K_{I,ring}$, for the chosen element ring interval ($ring = [n+1, N]$).

The standard deviation is calculated as [16]

$$s = \sum_{ring=n+1}^{N} \sqrt{\left(K_{I,ring} - K_I\right)^2}$$

where K_I is the estimated SIF for the evaluation point.

The relative SIF error is calculated as

$$\epsilon_{rel} = (K_I - K_{ref})/K_{ref}$$

where K_{ref} is the specified reference solution in the analysis. For the convergence analysis, K_{ref} is the most resolved model and for the benchmark analysis K_{ref} is the closed-form solution.

3.1.5.3 Elliptical cracks

For elliptical cracks, the variation along the whole crack front is of interest. The SIF varies substantially and gives highest values for various positions depending on the crack shape. Hence, for the elliptical cracks, the results in the report are presented with a plot of K_I along the crack front with respect to the angle θ (see Figure 2.11 for the definition of θ). Followed by symmetry in all of the crack cases, the evaluation is performed in the interval 0°-90° instead of 0°-360°.

K_I, s_{rel} and ϵ_{rel} are evaluated in the same way as described above for straight cracks at each evaluation point. The number of evaluation points and positions vary depending on the mesh. Therefore it is hard to compare each model against a reference model for elliptical cracks, since they are not evaluated at the same positions. Consequently, in most of the convergence analyses, the reference SIF K_{ref} is chosen as the closed-form solution and for benchmark analyses, K_{ref} is always the closed-form solution. The error is then presented in a plot with respect to the angle θ. Figure 3.10 below is an example of SIF and error plots presented for an elliptical crack.

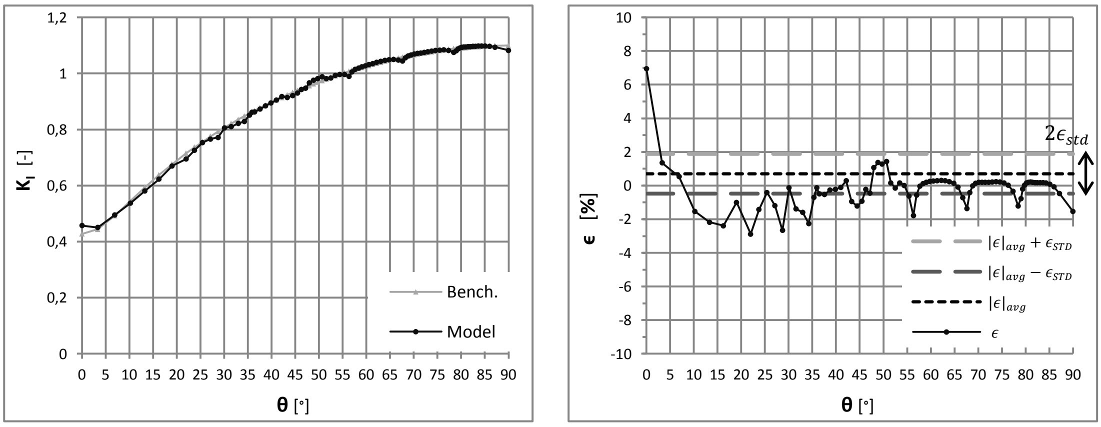

a) b)

Figure 3.10: An example of obtained results for an elliptical crack for all evaluation points 0°-90°. a) Estimated model SIF compared to benchmark B2. b) Corresponding error relative benchmark, including visualization of the (scalar) average error magnitude and average error STD.

In addition for the elliptical crack, the relative SIF standard deviation is estimated as the average over all evaluation points 0°-90°:

- $(s_{rel})_{avg}$, average relative SIF standard deviation

It is calculated according to:

$$(s_{rel})_{avg} = \frac{1}{m}\sum_{i=1}^{m} s_{rel,i}$$

where $s_{rel,i}$ is the relative SIF standard deviation at evaluation point i and m is the number of evaluation points between 0° and 90°.

To enable direct comparisons, scalar values related to the errors are calculated:

- $|\epsilon|_{avg}$, average error magnitude
- ϵ_{STD}, error standard deviation
- $\epsilon_{0°}$, error at 0°
- $\epsilon_{90°}$, error at 90°
- $\epsilon_{\max}$, maximum error

where the average error magnitude with the corresponding standard deviation is visualized for the example in Figure 3.10b.

The average error magnitude is calculated as the averaged absolute value of the error at each contour evaluation point between 0° and 90°:

$$|\epsilon|_{avg} = \frac{1}{m}\sum_{i=1}^{m}|\epsilon_i|$$

ϵ_{STD} is calculated as the standard deviation for the errors between 0° and 90°:

$$\epsilon_{STD} = \sum_{i=1}^{m}\sqrt{\left(\epsilon_i - \epsilon_{avg}\right)^2}$$

where ϵ_{avg} is taken as the average over all evaluations points between 0° and 90°.

The error for the contour evaluation point closest to 0° and 90° is taken as $\epsilon_{0°}$ and $\epsilon_{90°}$, respectively. The maximum error $\epsilon_{\max}$ is chosen as the largest error, whether it is positive or negative.

3.2 Convergence analysis

As mentioned before, the convergence analysis consists of two parts; a mesh technique study and a model simplification study. The convergence analyses are performed systematically for each parameter/aspect of interest, such as mesh size and elements, to find its influence and requirements on the accuracy. Analyses in the thesis are performed with the two different meshing techniques; high end analysis and low end analysis. Focus is on the high end analysis to foremost obtain accurate results. The aim is to cover all of the important aspects included in the modeling of a general crack, to enable the proposition of a strategy. The approaches in the two studies are outlined in this section and in Chapter 4 the full studies are presented with results and a discussion.

The models used in this analysis are carefully built up and tested to guarantee robust simulations with respect to the other modeling aspects. That is to say, all other modeling aspects at their fixed values have negligible influence on the results. Furthermore the last element ring in the crack tip partition is not included in the contour integral calculation, to not include the influence of the unstructured mesh in the crack partition. To guarantee full use of the crack tip enrichment functions, the crack front is placed in the middle of the elements where all element nodes are active if not specified otherwise.

Focus in these cases is to find accepted intervals for the various aspects in the models. It should also be noted that this work is not aimed to result in general rules, since each crack simulation is individual, but to result in guidelines and general validations.

3.2.1 Mesh technique study

A large part of the work is devoted to the mesh technique study to see how different meshes affect the stress intensity factor results. A substantial number of tests and analyses have been performed throughout the study to find robust meshing methods that ensure accurate results. The aspects investigated in the mesh technique study are presented here. The approaches are applied on both basic through-thickness cracks and general elliptical cracks.

3.2.1.1 High end evaluation

This investigation is carried out with the intention to get useful information regarding crack tip mesh size ($h_{x1},\ h_{x2}$) and the contour domain size (H_{x1}, H_{x2}) using the high end meshing technique. Initially, the basic straight crack case of B1 is studied with four mesh sizes together with three contour domains sizes. This analysis is furthermore extended to include two larger and two smaller contour domains with different mesh sizes. This extension is referred to as *part two* in the analysis of the straight crack. Lastly the analysis is also applied to a more general crack case, the elliptical crack case B2. This analysis is denoted *part three.* This is motivated by the complexity and large influence of the tip mesh size and contour domain aspects.

The main idea with this analysis is to study fixed contour domain sizes with decreasing mesh sizes, to evaluate whether convergence is obtained for the mesh sizes suggested. The SIF results are compared relative to the most resolved mesh for each contour domain size.

3.2.1.2 Low end evaluation

For complex geometries, it is of interest to investigate a more simple mesh that is unstructured and does not follow the crack tip. In the study, the low end meshing technique is investigated for the semi-elliptical crack case B2. What is studied is how the accuracy and robustness is affected by the partition size and the mesh size.

3.2.1.3 Crack region refinement (high end mesh)

The effects of the large discontinuities that the crack surfaces represent and the whole region around the crack are investigated with respect to the mesh size. The straight crack case (B1) is analyzed with various mesh sizes of the crack partition region, with the crack tip partition kept small and its mesh size fixed.

3.2.1.4 Mixed element types (high end mesh)

To overcome the difficulties to mesh complex geometries, an investigation of mixed element types with a tie constraint is performed. In the regular manner, the high end approach is used and the crack case B1 is analyzed. Hexahedral elements are used around the crack, but the neighboring region of the material is meshed with tetrahedral elements. In the intersecting surfaces, a tie constraint is introduced to connect the different element types.

This analysis is aimed to show the validity and accuracy of introducing a tetrahedral mesh with a tie constraint and additionally reveal the requirements on the size of the domain with hexahedral mesh.

3.2.1.5 Element integration (high end mesh)

Two integration schemes available in Abaqus for XFEM are tested in the study; full integration and reduced integration. The latter uses a reduced number of integration points and is faster in a computational aspect at the expense of accuracy. Therefore, the two schemes are analyzed and compared with respect to accuracy and efficiency. For the efficiency aspect, calculation time is compared and K_I is compared for the accuracy aspect. In the investigation, the same model is tested with both reduced integration and full integration to avoid other aspects affecting the results.

3.2.1.6 Crack placement in mesh (high end mesh)

In *The Abaqus 6.11 Online Documentation* [6] it is advised not to place the crack tangential to element boundaries since it might lead to convergence difficulties. The effect of a crack lying on the element boundary is therefore investigated to enable a more flexible crack placement. Three crack placements are investigated; one where the crack tip lies in the middle of the elements, one where the crack tip lies on the element boundaries and one where the crack tip lies in the element nodes.

3.2.2 Model simplification study

In accordance with the ambition to enable more flexible crack simulations, two simplifications within the Abaqus models are investigated:

- Geometric symmetry
- Submodeling

The model simplification studies are conducted to simplify the modeling and to reduce the number of elements in the model. This study is also strongly motivated by the high mesh requirements from the mesh technique study (see Section 4.1.1).

3.2.2.1 Geometric symmetry

Symmetry assumption is investigated for a symmetry plane perpendicular to the crack for which the elliptical crack of benchmark case B3 is used for the evaluation. The analysis is aimed to reveal how well the contour integral calculation performs when the crack tip breaks the surface of the specimen. Problems with the contour integral calculations regarding this manner are identified in the *Abaqus 6.11 Online Documentation* [6].

3.2.2.2 Submodeling

As described in Section 3.1.4.1, submodeling is a technique to study a specific area in a model with a refined mesh to obtain a more accurate solution. The purpose of the study is to see if the SIF evaluation with submodeling gives the same result as using the reference model. Both node-based (displacement interpolation) and surface-based (stress interpolation) submodeling is investigated.

3.3 Benchmark analysis

Five benchmark cases are studied to evaluate the performance and accuracy of XFEM in Abaqus. Different crack dimensions are tested for each benchmark case to see which crack dimensions that are valid for each crack case. Requirements from the convergence analysis are applied to guarantee the optimal solution in the comparison. The full analysis is presented in Chapter 4 with results and a discussion.

4 Numerical investigation

In this chapter, the procedure and results of the convergence analysis and the benchmark analysis are presented and discussed. The central parameters and results are highlighted with bold in the tables.

4.1 Convergence analysis

The six analyses in the mesh technique study are presented here as well as the two model simplification techniques.

4.1.1 Mesh technique study

4.1.1.1 High end evaluation

The crack case used in the straight crack analysis is a through middle crack in a finite plate (B1). The model is built up according to the high end analysis with symmetry at half of the specimen width, see Figure 4.1a. Dimensions for the specimen and partitions for the different straight crack models in *part one* and *two* analyses are defined in Table 4.1-Table 4.2. The mesh for model 14 is shown in Figure 4.1b.

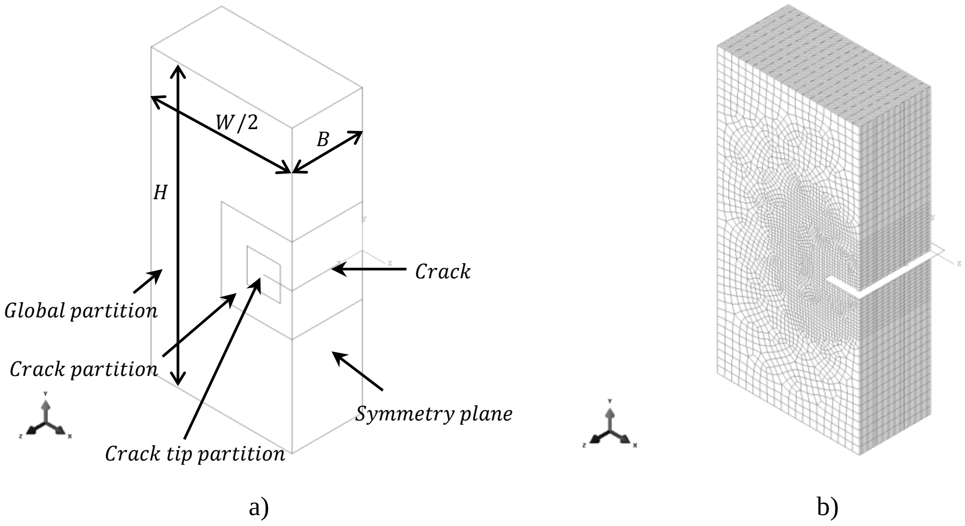

Figure 4.1: The partition dimensions and mesh of Model 14 using the high end analysis.

The load is applied as pure tension according to the B1 crack case. Symmetry boundary conditions are applied on the symmetry plane and an additional boundary condition is applied to prevent rigid body motion. The contour domain is specified to coincide with the crack tip partition by specifying the number of element rings to include, see Figure 4.2. The global mesh sizes g_W and g_H are 0.25 and g_B is 0.04. The construction of and parameters for the contour domain is visualized in Figure 4.2.

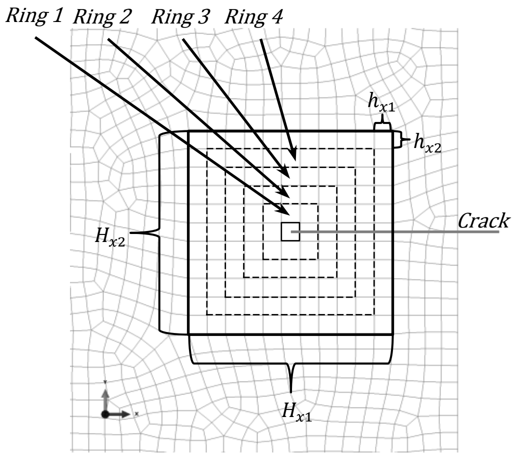

Figure 4.2 In the figure, the contour domain is built up by element rings.

Table 4.1: Identical properties for the models in the high end analysis (*part one* and *two*)

	Specimen size				Partition size		Mesh size			
Model	Crack length	Specimen width	Specimen height	Specimen depth	Part. width	Part. height	Tip depth	Part. width	Part. height	Part. depth
–	a $[m]$	W/a $[-]$	H/a $[-]$	B/a $[-]$	P_W/a $[-]$	P_H/a $[-]$	h_{x3}/a $[-]$	p_W/a $[-]$	p_H/a $[-]$	p_B/a $[-]$
1-16	2	10	10	2,5	5	6	0,040	0,10	0,10	0,04

Table 4.2: Unique properties for the models in the high end analysis

		Mesh size		Partition size		Mesh properties	
	Model	Tip width	Tip height	Contour domain width	Contour domain height	Element rings	Elements
	-	h_{x1}/a $[-]$	h_{x2}/a $[-]$	H_{x1}/a $[-]$	H_{x2}/a $[-]$	- [#]	C3D8r [#]
Part one	1	**0,019**	**0,019**	**0,125**	**0,125**	5	222 201
	2	**0,015**	**0,015**	**0,125**	**0,125**	7	243 432
	3	**0,013**	**0,013**	**0,125**	**0,125**	8	258 111
	4	**0,011**	**0,011**	**0,125**	**0,125**	10	274 680
	5	**0,019**	**0,019**	**0,250**	**0,250**	12	307 503
	6	**0,015**	**0,015**	**0,250**	**0,250**	15	323 631
	7	**0,013**	**0,013**	**0,250**	**0,250**	18	373 086
	8	**0,011**	**0,011**	**0,250**	**0,250**	21	420 840
	9	**0,019**	**0,019**	**0,500**	**0,500**	25	446 733
	10	**0,015**	**0,015**	**0,500**	**0,500**	32	578 781
	11	**0,013**	**0,013**	**0,500**	**0,500**	37	721 350
	12	**0,011**	**0,011**	**0,500**	**0,500**	44	944 433
Part two	13	**0,005**	**0,005**	**0,05**	**0,05**	5	274 176
	14	**0,004**	**0,004**	**0,05**	**0,05**	6	265 923
	15	**0,091**	**0,091**	**1,00**	**1,00**	5	152 019
	16	**0,077**	**0,077**	**1,00**	**1,00**	6	162 099

To reveal the influence of the crack tip mesh size in the part one analysis, a systematic increase with respect to the tip mesh sizes h_{x1} and h_{x2} is done simultaneously between $1.9 - 1.1$ percent of the crack length for fixed contour domain sizes. The contour domain sizes are varied as 12.5, 25 and 50 percent of the crack length ($H_{x1} = H_{x2} = [0.125, 0.25, 0.5]$).

In the *part two* analysis, the contour domain size is set to 5 and 100 percent of the crack length ($H_{x1} = H_{x2} = [0.05,\ 1]$). Crack tip mesh sizes are set to 0.5 and 0.4 percent of the crack length for the small contour and 9.1 and 7.1 percent for the large contour.

Followed by the converged results of model 14 (see Table 4.4), it will serve as a basis of all forthcoming straight crack models. The crack tip partition and mesh size will be kept while the other aspects can be changed depending on the analysis. The results of model 14 will also serve as reference solution in some forthcoming analyses.

The benchmark analysis is post-processed according to the procedure described for straight cracks, with $n = 3$. Reference solution, K_{ref}, is set as K_I from the most refined mesh for the various contour domains in part one.

The results of *part one* for the straight crack is shown in Table 4.3, where the tip mesh sizes, contour domain sizes and number of element rings is presented again for all models. The results for the models in *part two* are shown in Table 4.4.

The relative error between all the models and their respective reference model is less than 0.6 percent in *part one* (see Table 4.3). For model 5-8 and 9-12, it can be seen that the error reduces slightly with decreasing mesh size. This is not obtained for the smallest contour domain (model 1-4) in *part one* analysis, were the coarsest mesh instead gives the smallest error. But the errors are so small that they cannot be excluded from just numerical discretization errors.

Looking at the relative SIF STD, the deviation gets larger for increasing mesh size instead of showing sign of better convergence for the contour integrals. In model 1-8 the relative deviation shows sign of good convergence in the contour integrals, whereas the large contour domain in model 10-12 shows a significant higher deviation, around 3 percent. This can be explained by the fact that the standard deviation is calculated for all element rings except the ones that are excluded. Hence, when the amount of element rings increase and thereby the amount of contour integrals, more deviation can occur between the values from numerical variations. With this in mind, the relative SIF error alone still proves converged solutions at the suggested mesh sizes for the various domains.

Table 4.3: Results: High end evaluation for the straight crack case B1 (*part one*). $K_{I,bench} = 1,0254$

Model	Tip width, height	Contour domain width	Contour domain height	Element rings	SIF	Rel. SIF STD	Rel. SIF error
-	$h_{x1}/a\,, h_{x2}/a$ $[-]$	H_{x1}/a $[-]$	H_{x2}/a $[-]$	- $[nr.]$	$K_I/(\sigma_\infty\sqrt{\pi a})$ $[-]$	s/K_I [%]	ϵ_{rel} [%]
1	0,019	0,25	0,25	5	1,1030	**0,02**	**-0,01**
2	0,015	0,25	0,25	7	1,1041	**0,19**	**0,09**
3	0,013	0,25	0,25	8	1,1033	**0,17**	**0,02**
4	0,011	0,25	0,25	10	1,1031	**0,28**	**Ref.**
5	0,019	0,5	0,5	12	1,1019	**0,36**	**-0,02**
6	0,015	0,5	0,5	15	1,1018	**0,45**	**-0,03**
7	0,013	0,5	0,5	18	1,1023	**0,31**	**0,01**
8	0,011	0,5	0,5	21	1,1021	**0,42**	**Ref.**
9	0,019	1	1	25	1,0969	**0,39**	**-0,60**
10	0,015	1	1	32	1,1002	**2,94**	**-0,30**
11	0,013	1	1	37	1,1019	**3,05**	**-0,15**
12	0,011	1	1	44	1,1035	**3,30**	**Ref.**

In contrast to *part one*, the results for the *part two* analysis gives a clear break point where the solution for the straight crack does not converge. In Table 4.4, it can be observed that a mesh size of around 9 percent of the crack width introduces a significant error compared to the other models. Also the relative SIF STD indicates a lack of convergence. This can be related to the coarse mesh together with the contour domain, where only five element rings are included in the contour integral. But with a small refinement towards a mesh size of 7.7 percent of the crack width, convergence is again obtained. For the very small contour domain in model 13 and 14, surprisingly good results are obtained for the same number of element rings. For model 14 the relative SIF STD shows that especially good convergence in the solution is obtained. From this, the conclusion can be made that a small contour domain with a small crack tip mesh size captures the behavior well. This also motivates the use of this model in later analyses.

Table 4.4: Results: High end evaluation for the straight crack case B1 (part two). $K_{I,bench} = 1,0254$

Model	Tip width, height	Contour domain width	Contour domain height	Element rings	SIF	Rel. SIF STD	Rel. SIF error
-	$h_{x1}/a\,, h_{x2}/a$ $[-]$	H_{x1}/a $[-]$	H_{x2}/a $[-]$	- $[nr.]$	$K_I/(\sigma_\infty\sqrt{\pi a})$ $[-]$	s/K_I [%]	ϵ_{rel} [%]
13	**0,005**	**0,05**	0,05	5	1,1006	**0,30**	**-0,26**
14	**0,004**	**0,05**	0,05	6	1,1034	**0,01**	**-0,01**
15	**0,091**	**1,00**	1,00	5	1,0760	**2,64**	**-2,49**
16	**0,077**	**1,00**	1,00	6	1,0948	**0,57**	**-0,01**

For the more general crack case, the semi-elliptical surface crack in benchmark case B2 is used in *part three* of the analysis. The models are subjected to a pure tension load with boundary conditions to prevent rigid body motion. These models are built up using a mesh according to the high end analysis, seen in Figure 4.3.

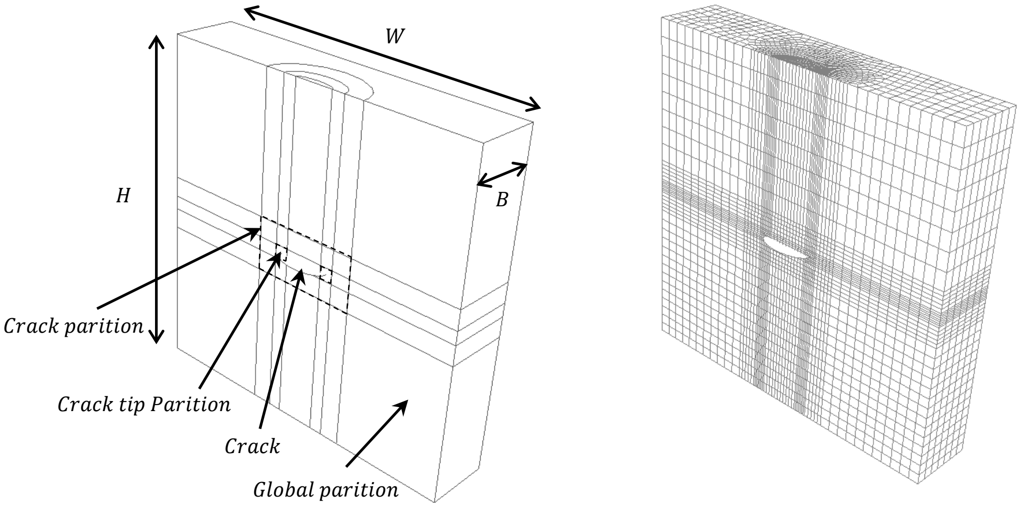

a) b)

Figure 4.3: The different partitions and specimen dimensions and are shown in a) and the mesh in b) for a semi-elliptical crack using the high end analysis.

The specimen and partition sizes, as well as the mesh sizes are presented in Table 4.5 and Table 4.6. The global mesh sizes g_W, g_H, g_B for models 17-22 are 0.25 and for models 23-25 the global mesh sizes are 0.5.

Table 4.5: Identical properties for the models in the high end analysis (part 3)

	Specimen size					Partition size			Mesh size	
Model	Crack depth	Crack ratio	Specimen width	Specimen height	Specimen depth	Ellipse radius	Ellipse radius	Ellipse height	Tip tang.	Ellipse tang.
−	a $[m]$	a/c $[-]$	W/a $[-]$	H/a $[-]$	B/a $[-]$	El_A/a $[-]$	El_C/a $[-]$	El_{height}/a $[-]$	h_{x3}/a $[-]$	el_{tang}/a $[-]$
17-25	4	0,5	25	25	5	2	4	1	0,063	0,13

Table 4.6: Unique properties for the models in the high end analysis (part 3)

		Mesh size			Partition size		Mesh properties	
	Model	Tip width	Tip height	Ellipse height	Contour domain width	Contour domain height	Element rings	Elements
	-	h_{x1}/a $[-]$	h_{x2}/a $[-]$	el_{height}/a $[-]$	H_{x1}/a $[-]$	H_{x2}/a $[-]$	- [#]	C3D8r [#]
Part 3	17	**0,008**	**0,008**	0,20	**0,05**	**0,05**	5	592 614
	18	**0,007**	**0,007**	0,20	**0,05**	**0,05**	6	625 190
	19	**0,006**	**0,006**	0,20	**0,05**	**0,05**	7	657 758
	20	**0,008**	**0,008**	0,20	**0,15**	**0,15**	18	772 411
	21	**0,007**	**0,007**	0,20	**0,15**	**0,15**	21	875 809
	22	**0,006**	**0,006**	0,20	**0,15**	**0,15**	24	985 687
	23	**0,008**	**0,008**	0,26	**0,25**	**0,25**	31	753 183
	24	**0,007**	**0,007**	0,26	**0,25**	**0,25**	36	926 873
	25	**0,006**	**0,006**	0,26	**0,25**	**0,25**	41	1 118 563

Three different contour domain sizes are investigated; 5, 15 and 25 percent of the crack depth. For these three domains, the tip mesh sizes h_{x1} and h_{x2} are decreased three times with mesh sizes of 0.8, 0.7 and 0.6 percent of the crack depth.

In model 17 the two first element rings are inaccurate and discarded. For model 18 and 19 the first three element rings are excluded and for the rest of the models the first five element rings are excluded.

With the current mesh size, the number of elements in the last three models exceeds the limit that the computer resources can manage. Therefore, tie constraints are introduced in these models creating an inner and outer part, to reduce the amount of elements. The width and height of the inner part with finer mesh are 60 percent of the full size and the depth of the inner part is 100 percent. Furthermore, the inner global mesh size is doubled to reduce the number of elements even more. The global mesh size for the outer part is defined by g_{out}.

The post-processing is done according to the procedure for elliptical cracks according to Section 3.1.5.3, with the closed-form solution of benchmark case B2 (2.39) as reference solution.

For the semi-elliptical crack, the best results are obtained for models 20-22 according to the SIF result in Table 4.7. For all these models, $|\epsilon|_{avg}$ is below 0.59 percent relative to the closed-form solution. The average error magnitude shows good convergence in models 17-19 and 23-25 as well for the suggested crack tip mesh sizes and contour domains, with magnitudes below 1.1 percent. But in these models, a few peaks is seen through the maximum error ϵ_{max}. Models 17-19 have error peaks reaching up to 7 percent and otherwise oscillating within 2 percent. This behavior is shown in Figure 4.4b for model 19. Models 23-25 have error peaks ranging from 5.82 for the coarsest to 3.64 percent for the finest mesh. The error is oscillating within 1.4 percent.

For model 22 in Figure 4.4, it can be seen that the error is oscillating around 0 percent and is below 2 percent along the whole crack front, except for one peak value that reaches 2.33 percent, which is low compared to model 17-19 and 23-25.

When comparing the error plots for model 22 and 25 in Figure 4.4b, they are very similar when disregarding the peaks. These peaks might occur due to the tie constraint, since the mesh size is the same in the models and since theoretically a larger contour domain should give more accurate results for a numerical solution.

In conclusion, 7 element rings, as in model 19, are enough to give converged results for the corresponding mesh size. More rings can be implemented to receive even better accuracy but will require more computational resources and time due to the increase in number of elements in the model. Otherwise, mesh sizes and contour domains according to model 20-22 give best convergence.

Table 4.7: Results: High end evaluation for the semi-elliptical crack case B2 (part three)

Model	Crack depth	Crack ratio	SIF Avg. Rel. STD	SIF Avg. Error mag.	SIF Error STD	*SIF Error 0°*	SIF Error 90°	SIF Max error
-	a $[m]$	a/c $[-]$	$(s/K_I)_{avg}$ [%]	$\lvert\epsilon\rvert_{avg}$ [%]	ϵ_{STD} [%]	$\epsilon_{0°}$ [%]	$\epsilon_{90°}$ [%]	ϵ_{max} [%]
17	4	0,5	0,74	**1,10**	1,55	**1,33**	**-2,63**	**-6,81**
18	4	0,5	0,99	**1,16**	1,90	**-6,32**	**-2,55**	**-6,32**
19	4	0,5	0,97	**0,93**	1,30	**-1,95**	**-2,21**	**4,93**
20	4	0,5	1,02	**0,59**	0,70	**1,45**	**-1,42**	**2,20**
21	4	0,5	0,96	**0,53**	0,68	**1,10**	**-1,40**	**2,42**
22	4	0,5	0,95	**0,53**	0,73	**1,13**	**-1,42**	**2,33**
23	4	0,5	0,38	**0,84**	1,15	**1,52**	**-1,57**	**5,82**
24	4	0,5	0,38	**0,87**	1,38	**1,62**	**-1,56**	**-5,46**
25	4	0,5	0,29	**0,74**	1,09	**1,76**	**-1,45**	**-3,64**

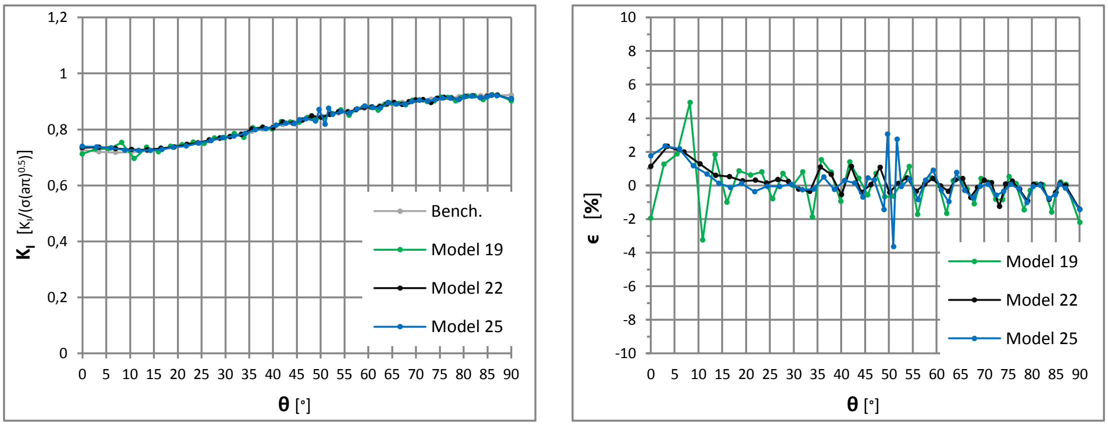

a) b)

Figure 4.4: A comparison of model 19,22 and 25 and the closed-form solution. a) shows the stress intensity factors for angles 0°-90° and b) shows the errors.

4.1.1.2 Low end evaluation

For the low end mesh study, the semi-elliptical surface crack in benchmark case B2 is investigated, seen in Figure 4.5. The models are subjected to loads and constraints according to the benchmark case. The study is performed by keeping the crack partition size constant while varying the mesh sizes p_H, p_W and p_B.

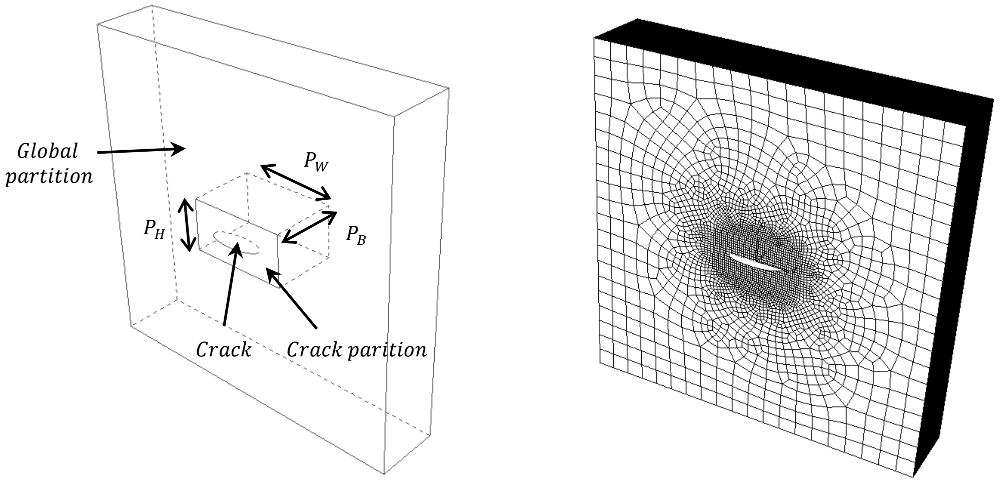

a) b)

Figure 4.5: Low end analysis of model 3. The partitions are defined in a) and the mesh in b).

The partition is defined by its height P_H and width P_W whereas the depth P_B is the same as the specimen depth B. In the analysis, three different mesh sizes are investigated with a fixed contour domain. This means that the number of element rings is changed depending on the mesh size in order for all three models to have the same contour domain size.

The specimen and partition sizes, as well as the mesh sizes are presented in Table 4.8 and Table 4.9.

Table 4.8: Identical properties for the low end analysis

	Specimen size					Partition size			Mesh size	
Model	Crack depth	Crack ratio	Specimen width	Specimen height	Specimen depth	Part. width	Part. height	Part. depth	Tip tang.	Ellipse tang.
–	a $[m]$	a/c $[-]$	W/a $[-]$	H/a $[-]$	B/a $[-]$	P_W/a $[-]$	P_H/a $[-]$	P_B/a $[-]$	h_{x3}/a $[-]$	el_{tang}/a $[-]$
26-28	3	0,4	33,3	33	7	4,3	2,0	6,7	0,063	0,13

Table 4.9: Unique properties for the low end analysis

	Mesh size						Mesh properties	
Model	Part. width	Part. height	Part. depth	Global width	Global height	Global depth	Element rings	Elements
-	p_W/a $[-]$	p_H/a $[-]$	p_B/a $[-]$	g_W/a $[-]$	g_H/a $[-]$	g_B/a $[-]$	- [#]	C3D8r [#]
26	**0,20**	**0,24**	**0,13**	1,000	1,000	0,133	7	140 950
27	**0,12**	**0,14**	**0,07**	1,000	1,000	0,073	13	486 122
28	**0,08**	**0,10**	**0,05**	1,667	1,667	0,052	19	1 260 330

The stress intensity factor for the different models is estimated by excluding element rings $n = 5$, $n = 4$ and $n = 3$ for models 26, 27 and 28, respectively. The post-processing procedure is done as described for elliptical cracks (Section 3.1.5.3) and the reference solution is the closed-form solution (2.39).

For the low end analysis, the post-processing results are presented in Table 4.10. The mesh size decreases for the three models, where model 28 has the finest mesh. The stress intensity factor and error comparisons are seen in Figure 4.6.

As expected, this meshing technique does not obtain as good convergence as the high end approach according to the results from models in this analysis. The average relative error ranges between 3.26-3.75 percent for the various mesh sizes and is decreasing with a decreasing mesh sizes. In addition, the error is oscillating significantly along the crack front for all models. The errors are below 10 percent for all three models, except peak values reaching 12 percent. The same pattern can be seen for the standard deviation of the errors.

It can thereby be stated that the accuracy is reasonably good for analysis in practice but according to the error, convergence is not fully obtained for these models. The robustness for the low end analysis is therefore shown to be lower compared to the high end analysis. Conclusions can also be drawn that a finer mesh and including more element rings give better accuracy, as expected. Contradictory, higher crack mesh refinement is cumbersome to achieve due to the mesh technique where the number of elements increases rapidly in the model.

Table 4.10: Results: Low end evaluation

Model	Crack depth	Crack ratio	SIF Avg. Rel. STD	SIF Avg. Error mag.	SIF Error STD	SIF Error 0°	SIF Error 90°	SIF Max error
-	a $[m]$	a/c $[-]$	$(s/K_I)_{avg}$ [%]	$\lvert\epsilon\rvert_{avg}$ [%]	ϵ_{STD} [%]	$\epsilon_{0°}$ [%]	$\epsilon_{90°}$ [%]	ϵ_{max} [%]
26	3	0,375	5,068	**3,75**	4,62	**11,71**	**-4,46**	**11,71**
27	3	0,375	6,825	**3,56**	4,32	**4,46**	**-4,77**	**-11,54**
28	3	0,375	6,054	**3,25**	3,56	**2,52**	**-2,65**	**8,18**

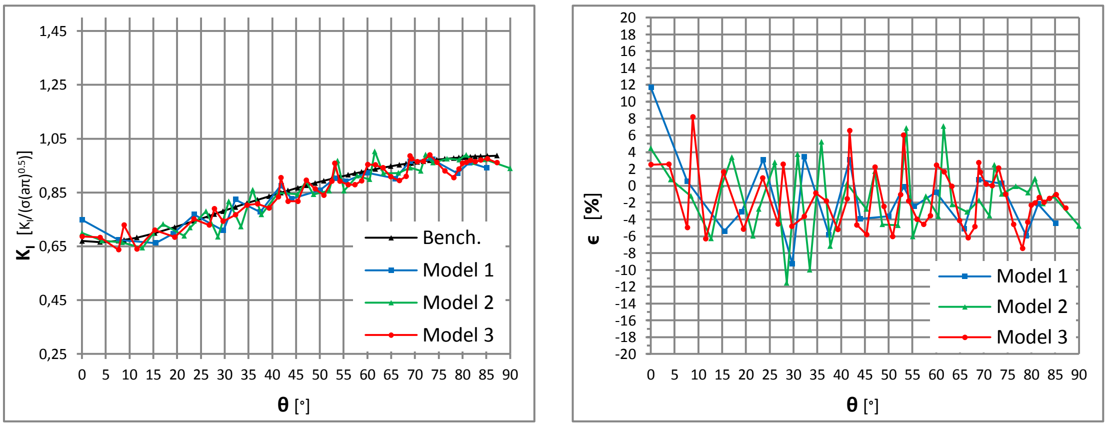

a) b)

Figure 4.6: A comparison of the three models and the closed-form solution. a) shows the stress intensity factor for angles 0-90° and b) shows the error.

4.1.1.3 Crack region refinement

The benchmark case in the analysis is the straight crack (B1) with a high end mesh, where model 14 in Section 4.1.1.1 is utilized. The only changes in the models for this analysis is the crack partition dimension (P) and the crack partition mesh size (p), see Table 4.11 and Table 4.12. The crack partition has been decreased to encapsulate the crack region close to the crack, see model and mesh in Figure 4.7. The mesh size has then been varied over a large interval in models 29-33.

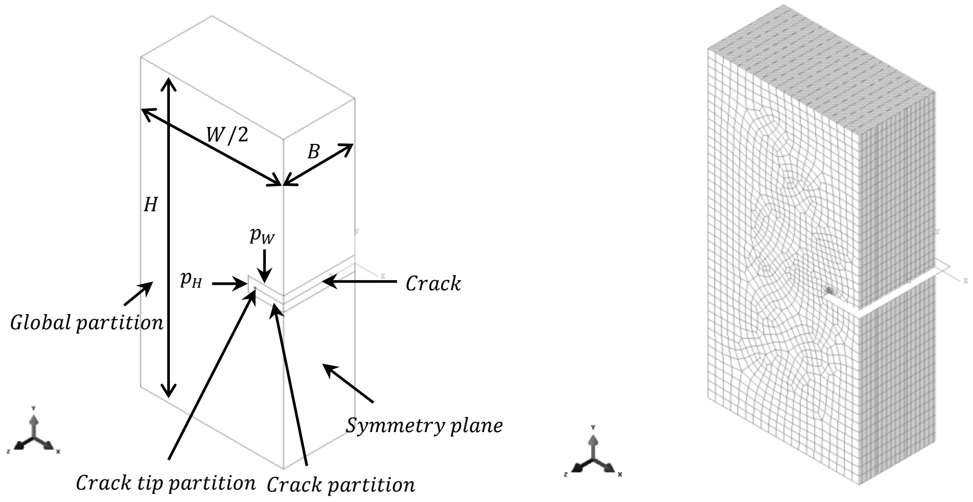

a)

b)

Figure 4.7: The figure shows the partitions and specimen dimensions in a) and the mesh in b) for model 1.

The mesh sizes are systematically varied from 17.5 to 1.5 percent of the crack length ($p_W = p_H = [0.175, 0.125, 0.075, 0.025, 0{,}015]$). This interval ranges from very coarse (close to the global mesh size) to very fine. For visualization, the most coarse crack region mesh is shown Figure 4.7b. As before, the parameters in the depth-direction are kept fixed since the variation is small. The global mesh sizes g_W and g_H are 0.25 and g_B is 0.04. The contour domain sizes H_{x1} and H_{x2} is kept as 0.05 to not influence the crack mesh.

Table 4.11: Identical properties for the crack region refinement study

	Specimen size				Partition size		Mesh size			
Model	Crack length	Specimen width	Specimen height	Specimen depth	Part. width	Part. height	Tip width	Tip height	Tip depth	Part. depth
–	a $[m]$	W/a $[-]$	H/a $[-]$	B/a $[-]$	P_W/a $[-]$	P_H/a $[-]$	h_{x1}/a $[-]$	h_{x2}/a $[-]$	h_{x3}/a $[-]$	p_B/a $[-]$
29-33	2	10	10	2,5	3	1	0,004	0,004	0,040	0,040

Table 4.12: Unique mesh properties for the crack region refinement study

	Mesh size		Mesh properties	
Model	Part. width	Part. height	Element rings	Elements
-	p_W/a [−]	p_H/a [−]	- [#]	C3D8r [#]
29	**0,175**	**0,175**	6	98 406
30	**0,125**	**0,125**	6	105 525
31	**0,075**	**0,075**	6	132 174
32	**0,025**	**0,025**	6	300 888
33	**0,015**	**0,015**	6	378 378

The analysis is post-processed according to the procedure described for straight cracks, with $n = 3$. Reference solution, K_{ref}, is set as K_I from model 14 in Section 4.1.1.1. The SIFs and errors are presented in Table 4.13.

Following the relative SIF error, the largest error occurs for model 29 which has a coarse mesh, close to the global mesh size. For decreasing mesh size in the remaining models, the error then becomes below 0.4 percent. This is neglectable in numerical contexts. Evaluating the relative STD of the SIF it can be seen that for a coarser mesh, model 29 and 30, the convergence is not as good as for model 31-33. It can thereby be concluded that the model is not sensitive to the mesh of the crack surfaces/crack region, but introducing a too coarse mesh disturbs the convergence slightly.

Table 4.13: Results: Crack region refinement study. $K_{I,bench} = 1.02541$

Model	Crack mesh size	SIF	SIF rel. STD	Rel. SIF error
-	p_w/a (p_H/a) [−]	$K_I/(\sigma_\infty\sqrt{\pi a})$ [−]	s/K_I [%]	ϵ_{rel} [%]
29	**0,175**	1,1156	**2,67**	**1,10**
30	**0,125**	1,0990	**3,63**	**-0,40**
31	**0,075**	1,1029	**0,50**	**-0,05**
32	**0,025**	1,1017	**0,17**	**-0,15**
33	**0,015**	1,1017	**0,27**	**-0,16**

4.1.1.4 Mixed element types (tie constraint)

The crack case used is the straight crack (B1). Model 14 from Section 4.1.1.1 is used, with some modifications. Everything but the crack partition is kept. Additional for this analysis is the implementation of several partitions through the model, see Figure 4.8a. Following Figure 4.8b, these partitions are used to construct seven regions (symmetric with respect to the crack) around the crack with decreasing size. These seven regions are then used to construct various regions with hex mesh, so called hex domains. These regions are defined with the dimension parameters W_{hex} and H_{hex} in Table 4.14. W_{hex} is the width, H_{hex} is the height and B_{hex} is the depth of the region. Full depth of the specimen is used in the regions ($B_{hex} = B$). Mesh sizes for the various regions are defined as w_{hex}, h_{hex} and b_{hex}.

In Figure 4.9 the mixed mesh in model 2 is shown with hex domain according to region 2. Full definition of dimensions and mesh sizes are presented in Table 4.14 and Table 4.15 for models 34-40 in this analysis.

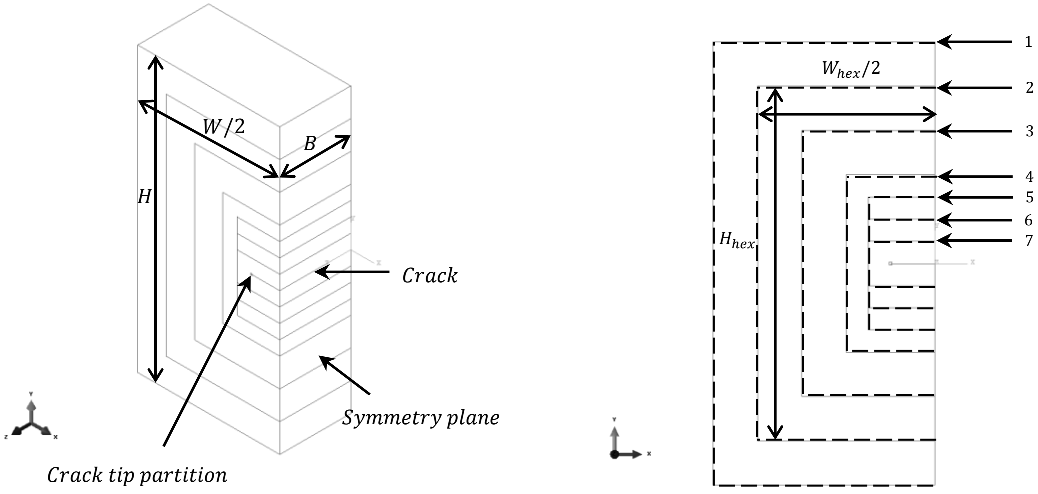

a)

b)

Figure 4.8 a) Model in 3D showing partitions b) Regions highlighted 1-7 (uniform with respect to the crack surface)

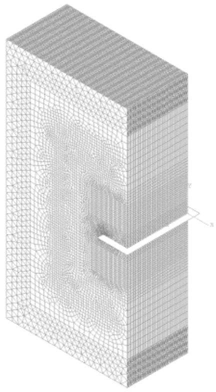

Figure 4.9: The figure shows the mesh of model 35.

The analysis is performed with decreasing hex mesh domains according to regions 1 to 7, seen in Figure 4.8b. In model 34-40, the hex domain ranges from 100 percent of the width and height, to 30 and 10 percent of the width and height, respectively. The full hex meshed model without tie constraint (model 34) serves as the reference model. Outside, linear tetrahedral elements are used (C3D4). Hence, the least accurate tetrahedral element is tested in this analysis and improvement with second order elements is possible.

Estimation of K_I from the contour integral is performed according to straight crack post-processing ($n = 3$).

Table 4.14: Unique parameters for the mixed element type analysis

Model	Hex region size		Mesh size			Mesh properties	
	Hex part. width	Hex part. height	Hex part. width	Hex part. height	Hex part. depth	Hex elements	Tet elements
-	W_{hex}/W [−]	H_{hex}/H [−]	w_{hex}/a [−]	h_{hex}/a [−]	b_{hex}/a [−]	C3D8r [#]	C3D4 [#]
34 (ref.)	**1,0**	**1,0**	0,250	0,250	0,04	394 002	0
35	**0,8**	**0,8**	0,100	0,200	0,04	368 424	107 680
36	**0,6**	**0,6**	0,100	0,085	0,04	313 992	336 988
37	**0,4**	**0,4**	0,075	0,090	0,04	231 777	682 277
38	**0,3**	**0,3**	0,075	0,075	0,04	184 275	944 759
39	**0,3**	**0,2**	0,200	0,075	0,04	157 815	1 170 842
40	**0,3**	**0,1**	0,050	0,050	0,04	131 355	1 389 763

Table 4.15: Identical parameters for the mixed element type analysis

Model	Partition size		Mesh size	Mesh properties
	Contour domain width	Contour domain height	Hex part. depth	Element rings
−	H_{x1}/a [−]	H_{x2}/a [−]	b_{hex}/a [−]	- [#]
34-40	0,05	0,05	0,04	6

The results for the mixed element study are presented in Table 4.16. According to this, the solutions have converged towards the full hexahedral mesh in all cases. The relative SIF error is below 0.27 percent in all models, and no clear improvement can be seen while increasing the hexahedral domain size from model 40 to model 35. It should also be noted that only linear tetrahedral elements is used outside the hexahedral domain. This study suggests that mixed element types with a tie constraint are appropriate to use without introducing any problems for the solution to convergence, even for small hexahedral domains around the crack (30 percent width and 10 percent height of the specimen).

It has to be emphasized that this analysis is only performed for the through-thickness crack in a finite plate, which is a simple crack geometry and also relatively simple specimen geometry and loading case. Hence, a more general crack and complex geometry might introduce difficulties to obtain the converged solution. This is believed to be the case especially for the linear tetrahedral elements that are tested here. In this sense, the use of the method is not proved for a more general crack configuration.

Table 4.16: Results: Mixed element types study. $K_{I,bench} = 1.02541$

Model	Hex mesh width	Hex mesh height	SIF	Rel. SIF STD	Rel. SIF error
-	W_{hex}/W [−]	H_{hex}/H [−]	$K_I/(\sigma_\infty\sqrt{\pi a})$ [−]	s/K_I [%]	ϵ_{rel} [%]
34 (ref.)	1	1	1,1012	**0,07**	**REF.**
35	**0,8**	**0,8**	1,0996	**0,29**	**-0,15**
36	**0,6**	**0,6**	1,0990	**0,23**	**-0,20**
37	**0,4**	**0,4**	1,0996	**0,29**	**-0,15**
38	**0,3**	**0,3**	1,0992	**0,20**	**-0,19**
39	**0,3**	**0,2**	1,0982	**0,23**	**-0,27**
40	**0,3**	**0,1**	1,0995	**0,16**	**-0,15**

4.1.1.5 Element integration

Crack configuration used is the straight crack B1 with high end analysis. Two comparisons are done between identical models, but with different integrations schemes. The two models with the reduced integration used in this analysis are chosen as model 13 and 14 from Section 4.1.1.1. Model 41 and model 42 are the new models with full integration, see Table 4.17. The former model is related to model 13 and the latter to model 14. The element type with full integration is specified as C3D8.

Table 4.17: Mesh properties for the element integration study

Model	Contour domain width	Contour domain height	Part. width	Part. height	Part. depth	Element rings	Elements
-	H_{x1}/a [−]	H_{x2}/a [−]	P_W/a [−]	P_H/a [−]	P_B/a [−]	- [#]	C3D8r [#]
41	0,05	0,05	5	6	-	5	274 176
42	0,05	0,05	5	6	-	6	265 923

The analysis is post-processed according to the procedure described for straight cracks, with $n = 3$. Comparison of the schemes is carried out with K_I and calculation time t_{calc} between model 13 and 41 and between model 14 and 42.

The results and comparison of the different integration schemes is presented in Table 4.18. The results show that the calculation time is reduced by more than 14 percent using reduced integrated elements while the difference in SIF is less than 0.15 percent. Relative to the decrease in computation time, the difference in SIF is insignificant in the numerical context.

Elements with reduced integration are therefore suggested. It should be noted that this is only verified for a simple crack and specimen case (B1). More complex geometries are believed to show larger effect from the reduced integration.

Table 4.18: Results: Element integration study. $K_{I,bench} = 1.02541$

Model	SIF (Full)	SIF STD (Full)	Calc. Time (Full)	SIF (Red.)	SIF rel. STD (Red.)	Calc. Time (Red.)	Diff. SIF	Diff. time
-	$K_I/(\sigma_\infty\sqrt{\pi a})$ $[-]$	$s/(\sigma_\infty\sqrt{\pi a})$ $[-]$	t_{calc} [s]	$K_I/(\sigma_\infty\sqrt{\pi a})$ $[-]$	$s/(\sigma_\infty\sqrt{\pi a})$ $[-]$	t_{calc} [s]	δ_{SIF} [%]	δ_{time} [%]
13 vs. 41	1,1006	0,30	3173	1,1001	0,24	2709	**-0,05**	**-14,6**
14 vs. 42	1,1034	0,01	3114	1,1018	0,01	2617	**-0,14**	**-16,0**

4.1.1.6 Crack placement in mesh

A semi-elliptical crack according to benchmark B2 is studied and the high end mesh is used. Three crack placements are modeled; one where the crack tip lies in the middle of the elements (model 45), one where the crack tip lies in the middle of the element boundaries (model 44) and one where the crack tip lies in the element nodes (model 43). The reference model has the crack tip placed in the middle of the elements and is visualized in Figure 4.10a. The two models with the other crack placements, seen in Figure 4.10b and c, are investigated and compared against the reference model. Pure tension is applied on all three cases with constrained nodes to avoid the rigid body motions.

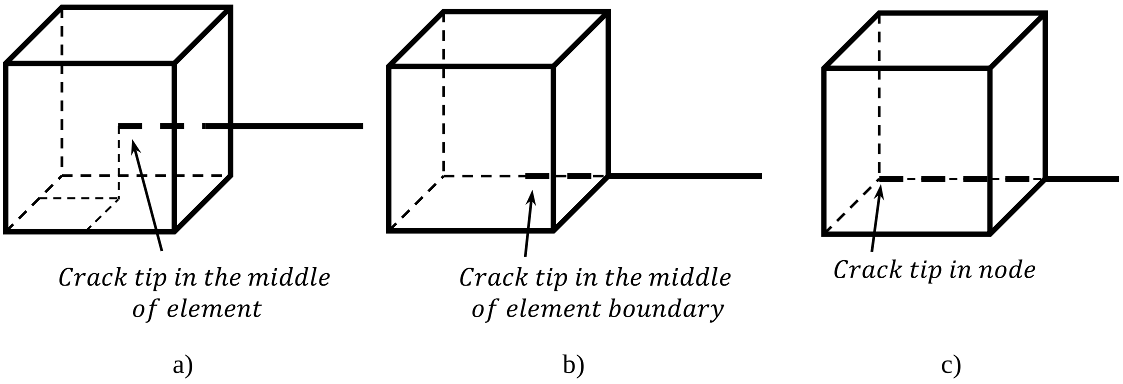

Figure 4.10: A schematic description of the three crack placements. In a) the crack lies in the middle of the element. b) shows a crack tip placed in the middle of an element boundary. In c) the crack is placed at the node.

The three crack placements are accomplished by alternating the crack tip mesh sizes h_{x1} and h_{x2} slightly. The model dimensions, mesh dimensions and properties are presented in Table 4.19-Table 4.21.

Table 4.19: Identical properties for the crack placement in mesh study

Model	Crack depth	Crack ratio	Specimen width	Specimen height	Specimen depth
-	a $[m]$	a/c $[-]$	W/a $[-]$	H/a $[-]$	B/a $[-]$
43-45	3	0,4	33,33	33,33	6,67

Table 4.20: Unique mesh sizes for the crack placement in mesh study

Model	Tip width	Tip height	Tip tang.	Ellipse height	Ellipse tang.	Global width	Global height	Global depth
-	h_{x1}/a $[-]$	h_{x2}/a $[-]$	h_{x3}/a $[-]$	el_{height}/a $[-]$	el_{tang}/a $[-]$	g_W/a $[-]$	g_H/a $[-]$	g_B/a $[-]$
43	0,0078	0,0083	0,075	0,17	0,27	0,33	0,33	0,33
44	0,0083	0,0083	0,075	0,17	0,27	0,33	0,33	0,33
45 (ref)	0,0078	0,0078	0,075	0,17	0,27	0,33	0,33	0,33

Table 4.21: Unique mesh properties for the crack placement in mesh study

Model	Contour domain width	Contour domain height	Ellipse radius	Ellipse radius	Ellipse height	Element rings	Elements
-	H_{x1}/a $[-]$	H_{x2}/a $[-]$	El_A/a $[-]$	El_C/a $[-]$	El_{height}/a $[-]$	- [#]	C3D8r [#]
43	0,067	0,067	1,33	2,67	1,33	7	718 488
44	0,067	0,067	1,33	2,67	1,33	7	708 900
45 (ref)	0,067	0,067	1,33	2,67	1,33	7	725 738

The stress intensity factor for the different models is averaged using all element rings except the first three ($n = 3$). The models are compared to the reference model since the evaluation points are obtained at the same angles. The post-processing is done according to the procedure for elliptical cracks in Section 3.1.5.3.

The SIF comparison for model 43 and model 44 relative to model 45 is presented in Table 4.22 and in Figure 4.11 for the different crack angles.

By evaluating the comparisons in the plots relative to the reference solution, only very small differences can be distinguished for the various crack placements. Following the comparison in Table 4.22 it can be seen that the differences are negligible and are believed to be only numerical variations. Therefore, free placement it suggested for the crack tip.

Table 4.22: Results: Crack placement in mesh study

Model	Crack depth	Crack ratio	SIF Avg. Rel. STD	SIF Avg. Error mag.	SIF Error STD	SIF Error $0°$	SIF Error 90°	SIF Max error
-	a $[m]$	a/c $[-]$	$(s/K_I)_{avg}$ [%]	$\lvert\epsilon\rvert_{avg}$ [%]	ϵ_{STD} [%]	$\epsilon_{0°}$ [%]	$\epsilon_{90°}$ [%]	ϵ_{max} [%]
43	3	0,375	1,05	0,17	0,22	-0,68	0,38	**-0,68**
44	3	0,375	1,04	0,07	0,18	-0,17	0,40	**0,43**
45 (ref)	3	0,375	1,04	-	-	-	-	-

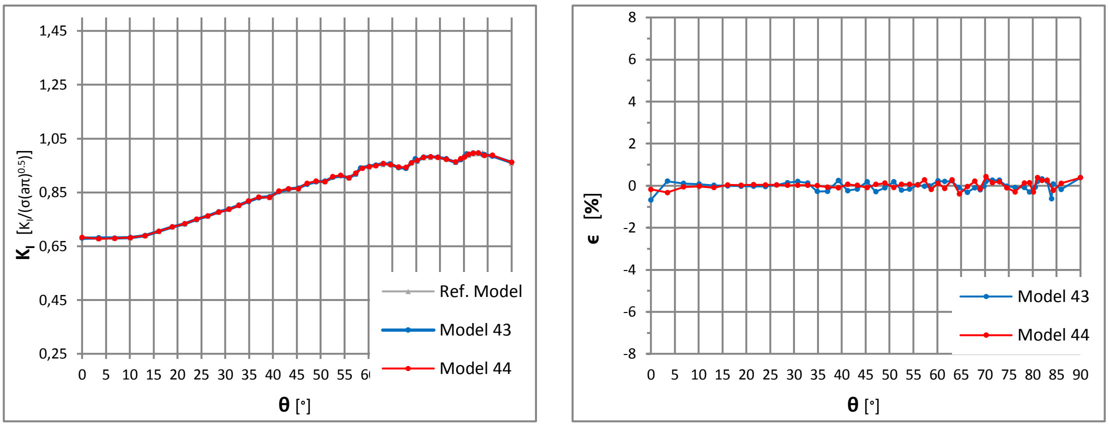

a) b)

Figure 4.11: a) SIF comparison and b) the error for model 43 and 44 versus the reference model.

4.1.2 Model simplification study

4.1.2.1 Symmetry

In the evaluation, two new models are created for the crack case; model 46 and 47. The model containing the full geometry is denoted model 46. See Figure 4.12 for visualization of model and mesh. High end analysis for an elliptical crack is used and small mesh sizes are implemented in the crack partition to be able to distinguish the symmetry effect from other effect related to the mesh. Full definition of the models is found in Table 4.23-Table 4.25. Boundary conditions are introduced to prevent rigid body motion.

Table 4.23: Crack and specimen dimensions for the symmetry study

Model	Crack depth	Crack ratio	Specimen width	Specimen height	Specimen depth
-	a $[m]$	a/c $[-]$	W/a $[-]$	H/a $[-]$	B/a $[-]$
46-47	1,5	0,5	100	100	13

Table 4.24: Mesh sizes for the symmetry study

Model	Tip width	Tip height	Tip tang.	Ellipse height	Ellipse tang.	Global depth	Global height	Global depth
-	h_{x1}/a $[-]$	h_{x2}/a $[-]$	h_{x3}/a $[-]$	el_{height}/a $[-]$	el_{tang}/a $[-]$	g_W/a $[-]$	g_H/a $[-]$	g_B/a $[-]$
46-47	0,018	0,018	0,067	0,20	0,23	2	2	2

Table 4.25: Mesh properties for the symmetry study

Model	Contour domain height	Contour domain width	Ellipse radius, A	Ellipse radius, C	Ellipse height	Element rings	Elements
-	H_{x1}/a $[-]$	H_{x2}/a $[-]$	El_A/a $[-]$	El_C/a $[-]$	El_{height}/a $[-]$	- [#]	C3D8r [#]
46	0,027	0,027	2,7	6,7	2,7	6	561 744
47	0,027	0,027	2,7	6,7	2,7	6	276 473

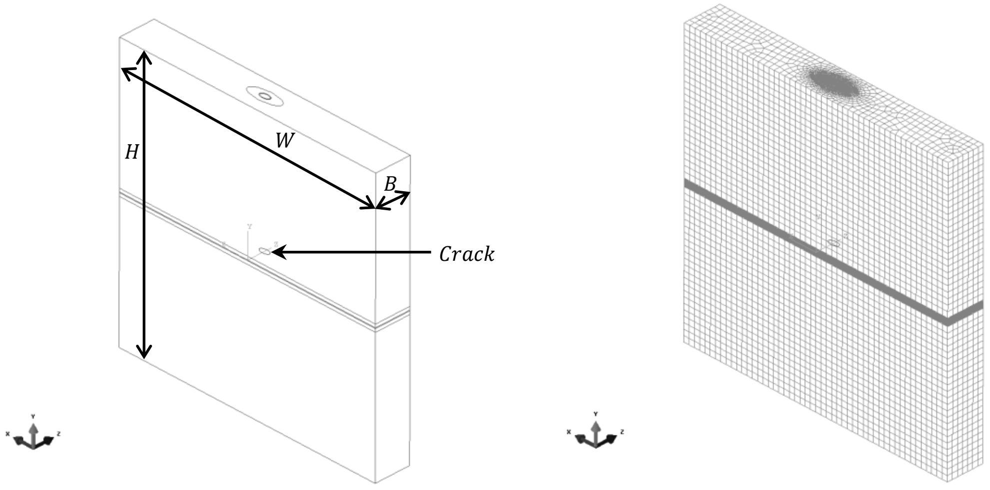

a)

b)

Figure 4.12: Specimen dimensions in a) and the mesh in b) for the full geometry model.

Symmetry assumption in the crack front is introduced in model 47. It is chosen as the plane half of the depth in the specimen, intersecting the crack front at 0° and 180°. Model 47 is therefore created from model 46, where separation in the symmetry plane (see Figure 4.13) is done and all other parameters are kept except boundary conditions. In this way, the models have the same mesh around the crack front. The evaluation points have therefore the same positions and the models can be compared directly. Except symmetry boundary conditions, constraints in the width-direction are only introduced to prevent rigid body motion.

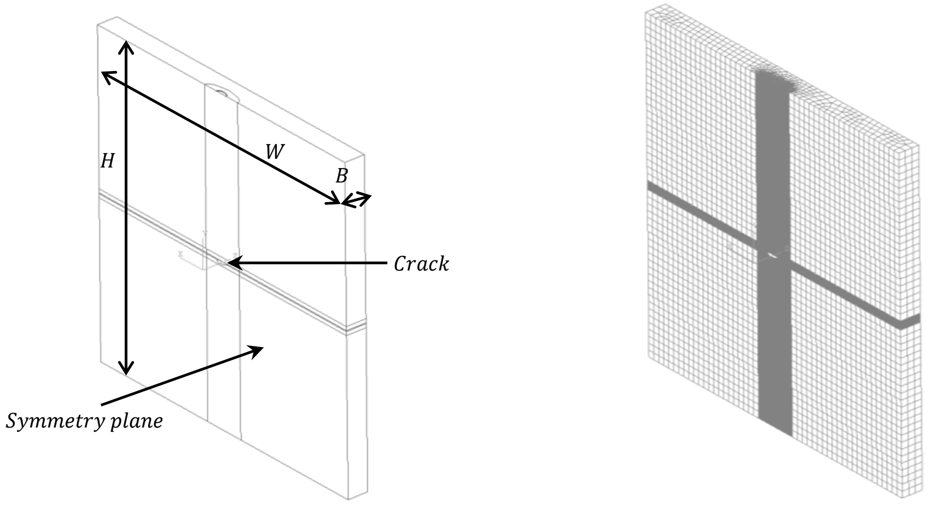

a)

b)

Figure 4.13: Specimen dimensions in a) and the mesh in b) for the symmetry model.

In both models, K_I is estimated between 0° and 90° in the crack front according to the elliptical post-processing procedure. The full model is chosen as the reference model.

In Figure 4.14 and Table 4.26 the SIF comparison and the error for the full and symmetric models is displayed. The average relative error for the symmetric model is 1.33 percent. Then at 0°, i.e. the position of the crack front that lies in the symmetry plane, the error is 22.7 percent. This is a high error compared to previous analyses, especially since only a symmetry condition is introduced which should give the same results. In the modeling context, this position represents a surface with symmetry boundary conditions in the symmetry model. The peak error proves that there exist problems with the contour integral when the crack tip breaks the surface [6].

The analysis shows that caution have to be taken when evaluating the SIF at a free surface. This problem has been seen for other models with surface cracks as well, especially connected to a coarser mesh. For a fine enough mesh, considering the results for the surface crack in Section 4.1.1.1, the solution at 0° coincides with the benchmark solution. Hence, the behavior at the free surface can be regarded as erroneous. This is also supported by the early work of Newman and Raju [17] where the peak also occurs and flattens out for increasing mesh density.

Table 4.26: Results: Symmetry

Model	Avg. Rel. SIF STD	SIF Avg. Error mag.	Error STD	SIF Error 0°	SIF Error 90°	SIF Max error
	$(s/K_I)_{avg}$ [%]	$\|\epsilon\|_{avg}$ [%]	ϵ_{STD} [%]	$\epsilon_{0°}$ [%]	$\epsilon_{90°}$ [%]	$\epsilon_{\max}$ [%]
46	0,79	REF	REF	REF	REF	REF
47	0,90	**1,33**	**3,95**	**-22,6926**	**-0,48**	**-22,6926**

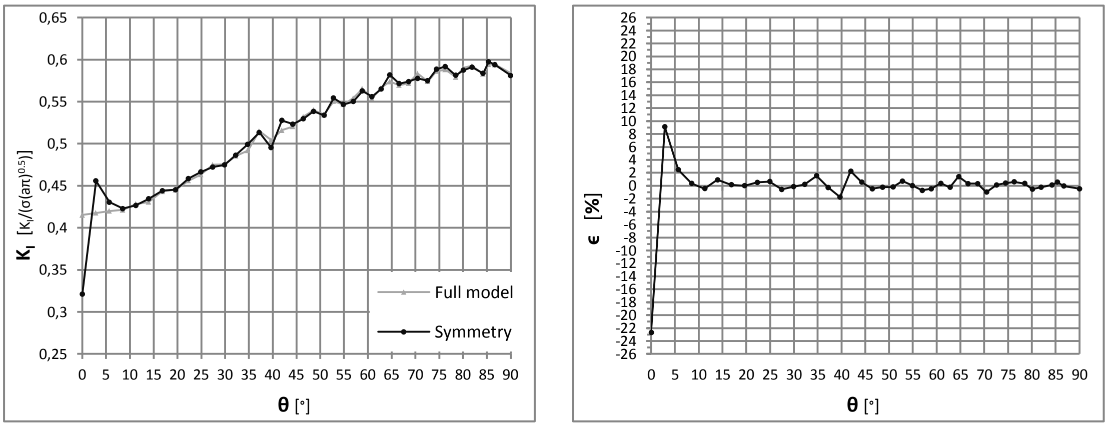

a) b)

Figure 4.14 SIF comparison and error for full and symmetric model

4.1.2.2 Submodel

The case considered is benchmark B2, a semi-elliptical surface crack. The global model is subjected to a pure tension load with constrained nodes to avoid rigid body motion. The submodel nodes are subjected either to a displacement field or a stress field interpolated from the global model. The high end meshing technique is used and the mesh sizes and partition sizes of the full model are identical in the submodels to ensure that these parameters have negligible effect on the results and enable direct comparison. The submodel dimensions are defined by S_W and S_H in width and height, respectively, and the depth of the submodel is equal to the reference model. The dimensions are shown in Figure 4.15b. The global model is coarse meshed without any refinements.

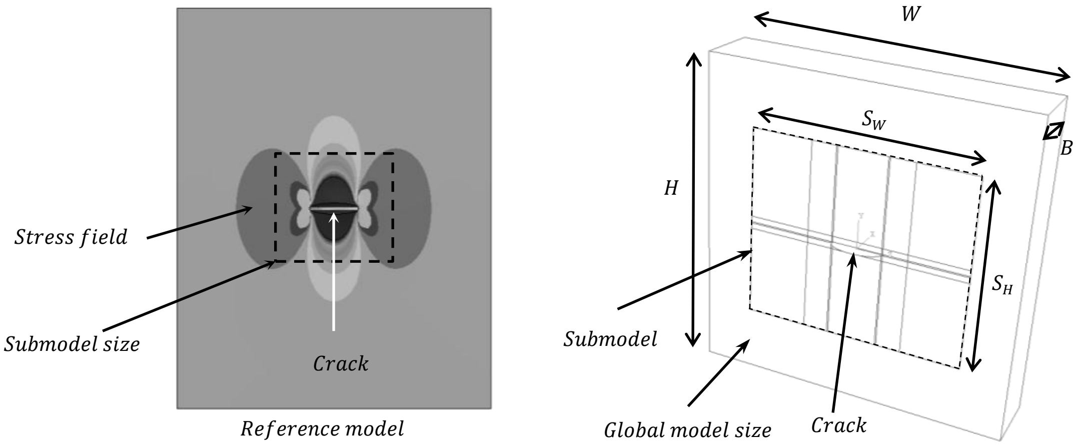

a) b)

Figure 4.15: The submodel in a) is so small that it might give an incorrect result since it doesn't capture the stress field. b) shows the submodel partitions and the global model size.

The only parameter that is changed in the analysis is the submodel size. Six different sizes are tested to see if there is any correlation between the submodel size and the accuracy of the model. The submodel sizes are shown in Table 4.27.

The analysis is started with a study of the stress field of the reference model. Secondly, the submodel sizes are chosen so that the first submodel is small enough to not capture the stress field variation. The submodels are then systematically increased in size to see if/when a correlation can be found. Figure 4.15a shows the stress fields on the surface of the reference solution and a theoretical submodel size that would not capture the stress fields in an accurate way.

Table 4.27: Submodel size

Model	Submodel width	Submodel height	Elements
-	S_W/W $[-]$	S_H/H $[-]$	C3D8r [#]
48	**0,40**	**0,60**	322 966
49	**0,50**	**0,60**	367 093
50	**0,50**	**0,70**	382 503
51	**0,60**	**0,70**	432 592
52	**0,60**	**0,80**	457 140
53	**0,70**	**0,80**	517 978
54 (ref)	-	-	665 483

In Table 4.28, the dimensions of the specimens are defined, in Table 4.29 the mesh sizes for the different partitions are presented and in Table 4.30 the dimensions of the partitions are specified.

Table 4.28: Crack and reference dimensions for the submodeling study

Model	Crack depth	Crack ratio	Reference width	Reference height	Reference depth
-	a $[m]$	a/c $[-]$	W/a $[-]$	H/a $[-]$	B/a $[-]$
48-54	4	0,5	25	25	5

Table 4.29: Mesh sizes for the submodeling study

Model	Tip width	Tip height	Tip tang.	Ellipse vert.	Ellipse tang.	Global width	Global height	Global depth
-	h_{x1}/a $[-]$	h_{x2}/a $[-]$	h_{x3}/a $[-]$	el_{vert}/a $[-]$	el_{tang}/a $[-]$	g_W/a $[-]$	g_H/a $[-]$	g_B/a $[-]$
48-54	0,006	0,006	0,069	0,13	0,20	0,25	0,25	0,25

Table 4.30: Mesh properties for the submodeling study

Model	Contour domain width	Contour domain height	Ellipse radius	Ellipse radius	Ellipse height	Element rings
-	H_{x1}/a $[-]$	H_{x2}/a $[-]$	El_A/a $[-]$	El_C/a $[-]$	El_{height}/a $[-]$	- [#]
48-54	0,05	0,05	2	4	1	7

The stress intensity factor for the different models is estimated using all element rings except the first three ($n = 3$). Since the models have the same crack tip partitions as the reference model, the evaluation points are the same. Thus, the submodels are compared to the reference model. The post-processing procedure is done according to elliptical cracks in Section 3.1.5.3.

In Figure 4.16 below, K_I and the relative error for the reference model and the closed-form solution is illustrated. The accuracy is very good with errors oscillating within 2 percent range.

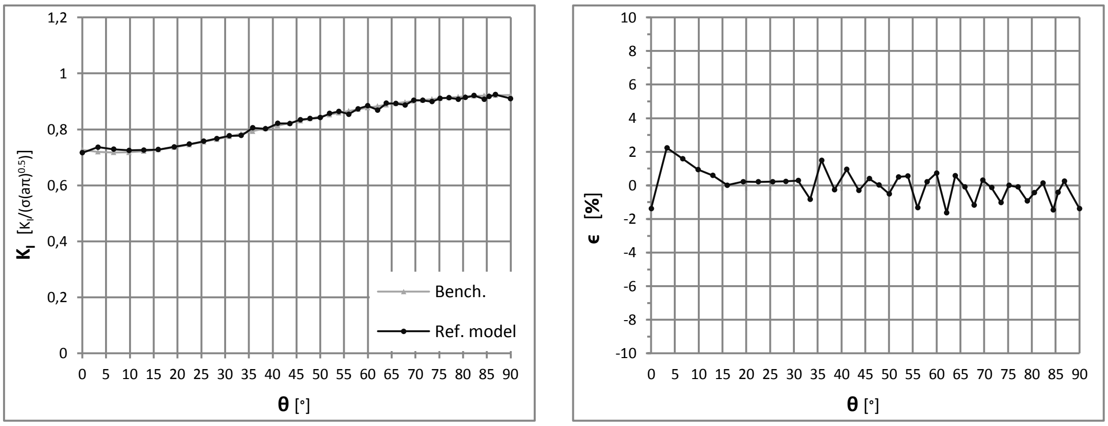

a) b)

Figure 4.16: SIF comparison and the error for the full reference model and the closed-form solution.

In Table 4.31, the post-processing variables are displayed for the submodels with interpolated displacements from the global model. The results show that the displacement submodels give small errors relative to the reference model along the whole crack front. The errors are also getting smaller as the submodels are getting larger, which can be explained by the fact that the larger submodels capture more of the correct stress fields.

For the largest submodel, model 53, the stress intensity factor and relative error comparison is plotted in Figure 4.17. The average error for the model is -1.73 percent and all displacement submodels are underestimating the stress intensity factor for all angles.

Table 4.31: Results: Submodeling with interpolated displacements

Model	Submodel width	Submodel height	SIF Avg. Rel. STD	SIF Avg. Error mag.	SIF Error STD	SIF Error 0°	SIF Error 90°	SIF Max error
-	w_{sub}/w_{full} [-]	h_{sub}/h_{full} [-]	$(s/K_I)_{avg}$ [%]	$\lvert\epsilon\rvert_{avg}$ [%]	ϵ_{STD} [%]	$\epsilon_{0°}$ [%]	$\epsilon_{90°}$ [%]	ϵ_{max} [%]
48	0,6	0,4	0,70	3,26	0,40	**-2,50**	**-3,29**	**-4,10**
49	0,6	0,5	0,67	2,39	0,41	**-2,03**	**-2,71**	**-3,28**
50	0,7	0,5	0,63	2,46	0,41	**-2,13**	**-2,77**	**-3,29**
51	0,7	0,6	0,65	2,04	0,40	**-1,88**	**-2,22**	**-3,00**
52	0,8	0,6	0,65	2,02	0,37	**-2,05**	**-2,16**	**-2,86**
53	0,8	0,7	0,63	1,73	0,35	**-1,77**	**-1,84**	**-2,51**
54 (ref)	-	-	REF	REF	REF	REF	REF	REF

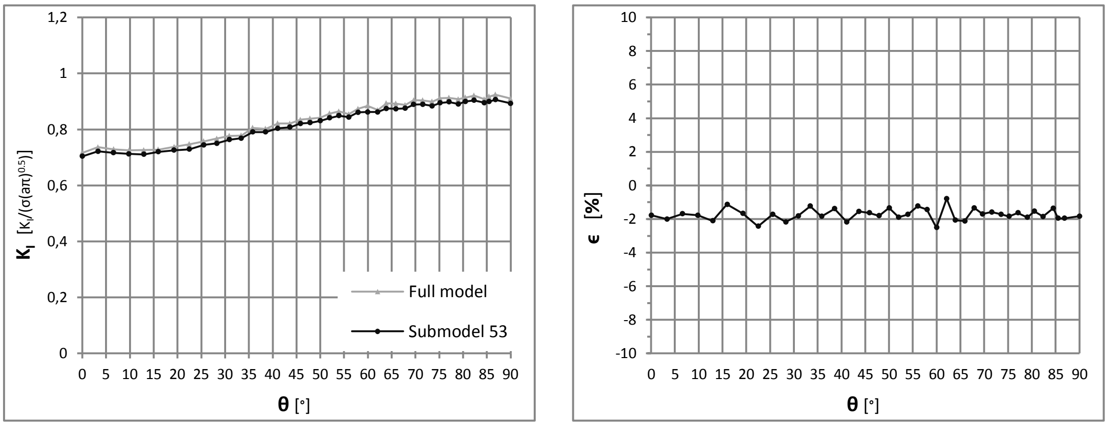

a) b)

Figure 4.17: SIF comparison and the error for the full model and Submodel 53 using interpolated displacement field.

In Table 4.32, the variables are shown for the submodels with an interpolated stress field from the global model. These results show that stress submodels give even better results than the displacement based. In Figure 4.18, K_I and the relative error for model 53 is plotted. The average error for the model is 0.43 percent and just as for the displacements, the error for the force submodels is decreasing as the submodel size is increasing. All stress submodels investigated overestimate K_I and are therefore more conservative than the displacement submodels.

Table 4.32: Results: Submodeling with interpolated stresses

Model	Submodel width	Submodel height	SIF Avg. Rel. STD	SIF Avg. Error mag.	SIF Error STD	SIF Error 0°	SIF Error 90°	SIF Max error
-	W_{sub}/W_{full} [%]	H_{sub}/H_{full} [%]	$(s/K_I)_{avg}$ [%]	$\lvert\epsilon\rvert_{avg}$ [%]	ϵ_{STD} [%]	$\epsilon_{0°}$ [%]	$\epsilon_{90°}$ [%]	ϵ_{max} [%]
48	**60**	**40**	**0,70**	**2,59**	**0,43**	**3,60**	**2,53**	**3,60**
49	**60**	**50**	**0,67**	**1,66**	**0,42**	**2,29**	**1,22**	**2,65**
50	**70**	**50**	**0,63**	**1,31**	**0,42**	**1,85**	**0,91**	**2,38**
51	**70**	**60**	**0,66**	**0,80**	**0,41**	**1,18**	**0,52**	**1,84**
52	**80**	**60**	**0,65**	**0,63**	**0,38**	**0,76**	**0,40**	**1,60**
53	**80**	**70**	**0,64**	**0,43**	**0,36**	**0,52**	**0,20**	**1,30**
54 (ref)	-	-	REF	REF	REF	REF	REF	REF

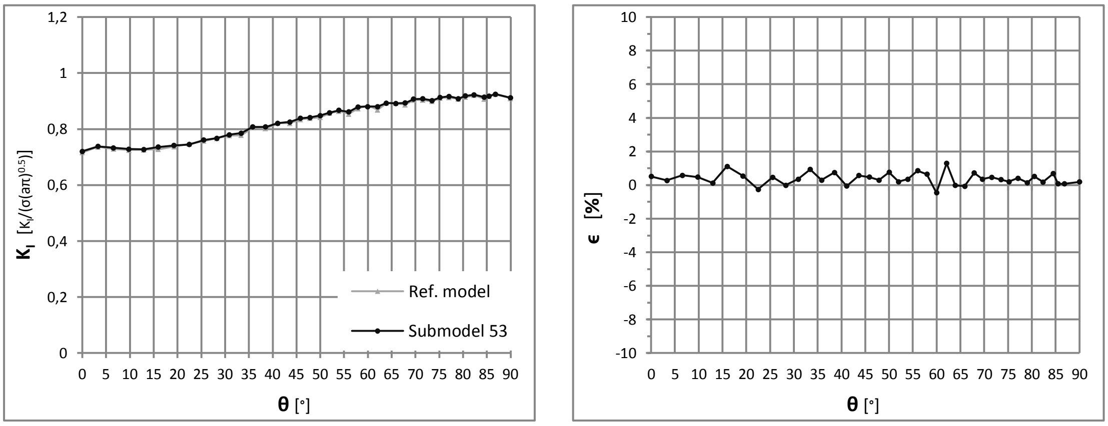

a) b)

Figure 4.18: SIF comparison and the error for the full model and Submodel 53 using interpolated stress field.

The results show that both force and displacement submodeling are very similar to the reference solution and converges with increasing submodel size. Per definition, the full model solution lies in between the two submodels. As seen here, the stress submodel is the upper limit and the displacement submodel is the lower. It is therefore suggested to use both methods to find an interval for the real solution. In both methods, models 52 and 53 give the most accurate solutions but model 48-51 are of more practical use and still give satisfactory results.

4.2 Benchmark analysis

4.2.1 B1 – Through-thickness crack

Investigation of the performance of a through-thickness crack in a finite plate is done relative the benchmark solution for B1. One crack length is used here. The central aspect for the straight crack is the depth of the specimen, which affects the solution but is not regarded in the closed-form solution (2.38) in benchmark case B1. Three depths are tested, $B = [10, 20, 30]$, i.e. 30 times the crack length at most. These specified depths are regarded as approaching the infinite depth solution. High end analysis for straight cracks is used to reveal the true accuracy. Visualization of model 1 and the corresponding mesh is shown in Figure 4.19.

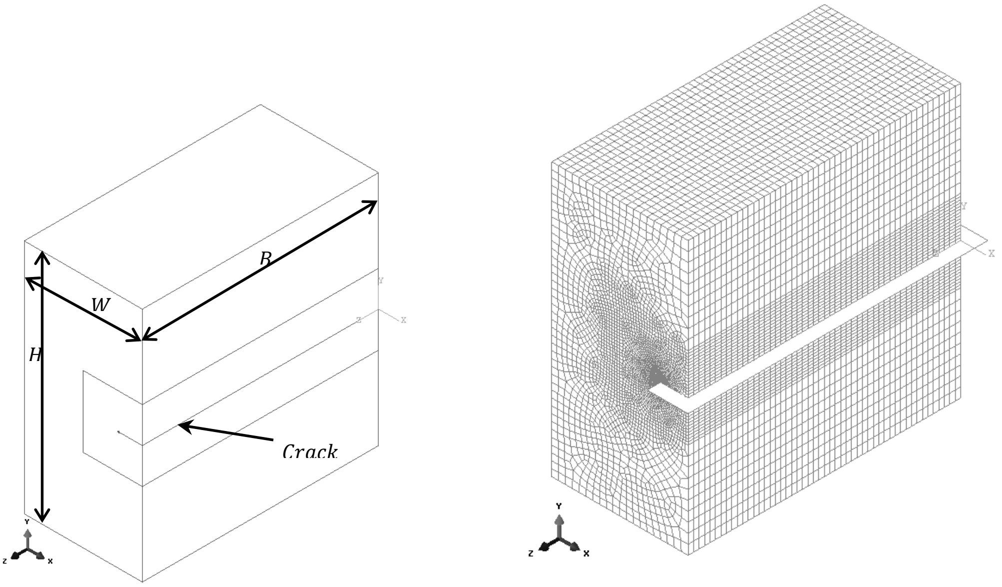

a) b)

Figure 4.19: The dimensions of model 1 are shown in a) and the mesh in b). Note the symmetry in the W-direction.

Model 14 from High end evaluation is used as the basis in this benchmark analysis. Complete definition of crack case, mesh properties and sizes is specified in Table 4.33-Table 4.35 for models 55-57.

Table 4.33: Specimen dimensions for benchmark case B1

Model	Specimen width	Specimen height	Specimen depth
-	W/a [−]	H/a [−]	B/a [−]
55	10	10	**10**
56	10	10	**20**
57	10	10	**30**

Table 4.34: Mesh sizes for benchmark case B1

Model	Tip width	Tip height	Tip depth	Part. width	Part. height	Part. depth	Global width	Global height	Global depth
-	h_{x1}/a [−]	h_{x2}/a [−]	h_{x3}/a [−]	p_W/a [−]	p_H/a [−]	p_B/a [−]	g_W/a [−]	g_H/a [−]	g_B/a [−]
55-57	**0,004**	**0,004**	**0,200**	0,10	0,10	0,20	0,25	0,25	0,20

Table 4.35: Mesh properties for benchmark case B1

Model	Contour domain width	Contour domain height	Part. width	Part. height	Part. depth	Element rings	Elements
-	H_{x1}/a $[-]$	H_{x2}/a $[-]$	P_W/a $[-]$	P_H/a $[-]$	P_B/a $[-]$	- [#]	C3D8r [#]
55	**0,025**	**0,025**	5	6	-	6	211 050
56	**0,025**	**0,025**	5	6	-	6	422 100
57	**0,025**	**0,025**	5	6	-	6	634 800

The benchmark analysis is post-processed according to the procedure described for straight cracks. Reference solution, K_{ref}, is set as the closed-form solution (2.38) from benchmark case B1 and in Table 4.36 the results are displayed.

It was thought that the error would converge for larger specimen depths where it would approach the "infinite" depth solution. According to the results in Table 4.36, this is not the case. The error is instead increasing for larger specimen depths. This can depend on the fact that the specimen depths are too small to fully see this behavior. Comparing to model 14 in Section 4.1.1.1, where the specimen depth is 2.5, the relative SIF error is 7.6 percent against the closed-form solution. Hence, model 55-57 here can be seen as close to the "infinite" depth solution.

Table 4.36: Results: Benchmark case B1

Model	Crack depth	Specimen depth	SIF	SIF bench	Rel. SIF STD	Rel. SIF error
-	a $[m]$	B/a $[-]$	$K_I/(\sigma_\infty\sqrt{\pi a})$ $[-]$	$K_I/(\sigma_\infty\sqrt{\pi a})$ $[-]$	s/K_I [%]	ϵ_{rel} [%]
55	2	**10**	1,0653	1,0254	0,26	**3,89**
56	2	**20**	1,0679	1,0254	0,26	**4,14**
57	2	**30**	1,0693	1,0254	0,15	**4,28**

4.2.2 B2 – Semi-elliptical surface crack

The benchmark B2 with a semi-elliptical crack is investigated for eight different crack dimensions with a/c ratios from 0.125 to 1, i.e. from very elliptical to circular cracks. An accuracy test of K_I is performed where the models are compared to the closed-form solutions. A high end mesh is used and two loading cases are investigated; pure tension and bending with boundary conditions to prevent rigid body motions.

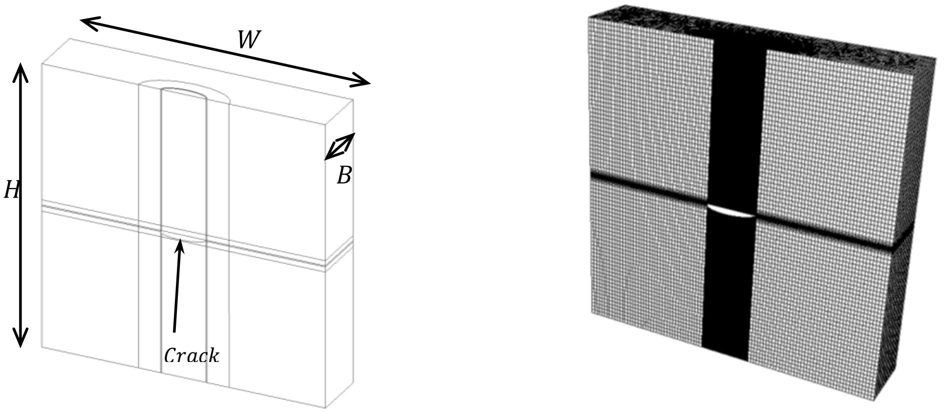

a) b)

Figure 4.20: The specimen dimensions , partitions and mesh for model 4.

The main parameter that is changed is the crack depth a whereas the crack width c is kept constant. The tangential mesh size h_{x3} is decreased as the crack depth gets smaller to avoid distorted elements and to keep the number of elements relatively similar.

The specimen and partition sizes, as well as the mesh sizes are presented in Table 4.37 and Table 4.38. The only variables changing between the models are h_{x3}, a and El_a. The dimensions and mesh sizes are the same for both bending and tension. The global mesh sizes g_W, g_H and g_B are 0.125.

Table 4.37: Identical properties for benchmark case B2

	Specimen size			Mesh size				Partition size			
Model	Spec. width	Spec. height	Spec. depth	Tip width	Tip height	Ellipse height	Ellipse tang.	Contour domain width	Contour domain height	Ellipse radius, C	Ellipse height
–	W/c $[-]$	H/c $[-]$	B/c $[-]$	h_{x1}/c $[-]$	h_{x2}/c $[-]$	el_{height}/c $[-]$	el_{tang}/c $[-]$	H_{x1}/c $[-]$	H_{x2}/c $[-]$	El_C/c $[-]$	El_{height}/c $[-]$
58-65	12,5	12,5	2,5	**0,003**	**0,003**	0,100	0,063	**0,025**	**0,025**	2,0	0,5

Table 4.38: Unique properties for benchmark case B2

	Specimen size		Mesh size	Partition size	Mesh properties	
Model	Crack depth	Crack ratio	Tip tang.	Ellipse radius, A	Element rings	Elements
-	a $[m]$	a/c $[-]$	h_{x3}/c $[-]$	El_A/c $[-]$	- [#]	C3D8r [#]
58	**1**	**0,125**	0,016	1,00	7	812 052
59	**2**	**0,250**	0,022	1,00	7	805 254
60	**3**	**0,375**	0,028	1,00	7	725 738
61	**4**	**0,500**	0,034	1,00	7	664 762
62	**5**	**0,625**	0,038	1,25	7	632 626
63	**6**	**0,750**	0,038	1,50	7	663 938
64	**7**	**0,875**	0,038	1,75	7	727 077
65	**8**	**1,000**	0,044	2,00	7	683 096

The post-processing results are visualized in Table 4.39 for tension and Table 4.40 for bending. The stress intensity factor comparisons are seen for models 58, 61 and 65 in Figure 4.21 for tension and Figure 4.22 for bending.

Table 4.39 shows that all models except 58 have less than 5 percent error at the critical points 0° and 90°. But all models have a jump in the solution at 0°, i.e. where the crack tip breaks the specimen surface. This is explained by the bad performance of the contour integral at the surface, as shown in Section 4.1.2.1. Looking at the average SIF error, the overall correlation is good for all models, although the error is increasing the more circular the cracks are.

Since the closed-form solution has an error of 5 percent and all models subjected to tension lie within this limit, they are fully verified for the given crack dimensions. Consideration has to be taken at 0° due to the error present here. Following the benchmark solution, it is suggested to disregard this value and extrapolate the SIF from the closest evaluation points.

Table 4.39: Results: Benchmark case B2 subjected to tension

Model	Crack depth	Crack ratio	SIF Avg. Rel. STD	SIF Avg. Error mag.	SIF Error STD	SIF Error 0°	SIF Error 90°	SIF Max error
-	a $[m]$	a/c $[-]$	$(s/K_I)_{avg}$ [%]	$\|\epsilon\|_{avg}$ [%]	ϵ_{STD} [%]	ϵ_{0° [%]	ϵ_{90° [%]	ϵ_{max} [%]
58	**1**	**0,125**	0,97	**0,70**	1,17	**6,94**	**-1,54**	**6,94**
59	**2**	**0,25**	1,59	**0,83**	1,00	**3,24**	**-1,63**	**3,44**
60	**3**	**0,375**	1,04	**0,87**	0,97	**2,19**	**-2,95**	**-2,95**
61	**4**	**0,5**	0,64	**0,65**	0,87	**-1,39**	**-1,38**	**2,23**
62	**5**	**0,625**	0,57	**0,91**	1,09	**-2,43**	**-1,58**	**3,67**
63	**6**	**0,75**	0,63	**1,45**	1,09	**-1,84**	**-1,08**	**3,83**
64	**7**	**0,875**	1,04	**2,08**	1,16	**-2,32**	**-0,22**	**4,65**
65	**8**	**1**	1,03	**2,85**	1,53	**-4,22**	**0,57**	**5,39**

In Figure 4.21 model 58 with the highest maximum error is shown. The relative error is less than 3 percent for all angles except at 0°. The model with the lowest error, model 61, is also presented. The relative error is less than 2 percent for all angles. Model 65 has the highest average error and the stress intensity factor and relative error are also shown in Figure 4.21. K_I is overestimated along the whole crack front.

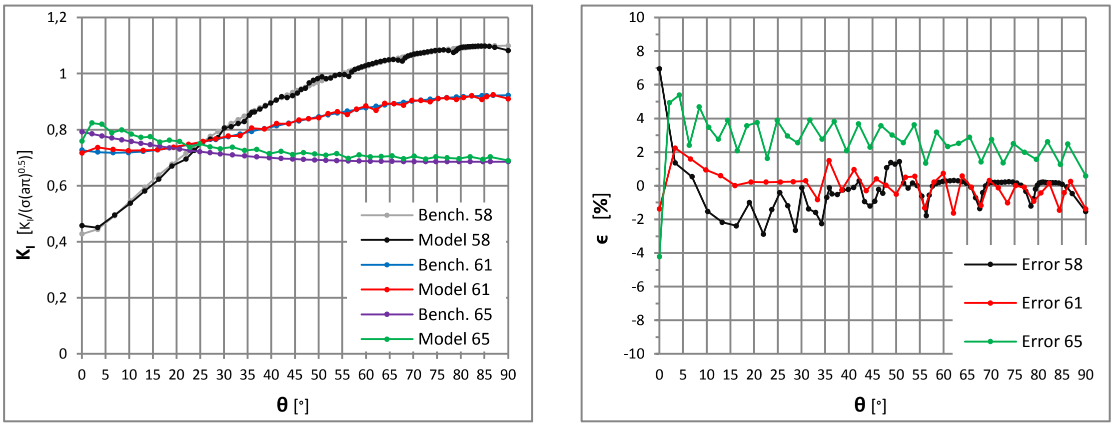

a) b)

Figure 4.21: SIF comparison and the error for models 58, 61 and 65 and the respective closed-form solution.

In Table 4.40, the results for the models subjected to bending are shown and in Figure 4.22 the SIF and error plots are displayed for the same models as for tension. The bending cases have a similar behavior as the tension cases. The bending specimens have the same jump behavior in the solution at 0° and an increase in average SIF error for more circular crack cases. The errors are less than 8 percent for all angles for the crack ratios investigated and the average errors are less than 2.5 percent.

Table 4.40: Results: Benchmark case B2 subjected to bending

Model	Crack depth	Crack ratio	SIF Avg. Rel. STD	SIF Avg. Error mag.	SIF Error STD	SIF Error 0°	SIF Error 90°	SIF Max error
-	a $[m]$	a/c $[-]$	$(s/K_I)_{avg}$ [%]	$\lvert\epsilon\rvert_{avg}$ [%]	ϵ_{STD} [%]	$\epsilon_{0°}$ [%]	$\epsilon_{90°}$ [%]	ϵ_{max} [%]
58	**1**	**0,125**	0,97	**1,02**	1,20	**6,47**	**-2,83**	**6,47**
59	**2**	**0,25**	1,59	**1,36**	1,66	**3,01**	**-3,14**	**5,69**
60	**3**	**0,375**	1,04	**1,58**	1,83	**1,88**	**-4,41**	**-4,41**
61	**4**	**0,5**	0,67	**1,74**	2,02	**-0,93**	**-3,14**	**3,66**
62	**5**	**0,625**	0,59	**1,92**	2,20	**-1,97**	**-3,57**	**4,98**
63	**6**	**0,75**	0,60	**1,82**	2,09	**-0,42**	**-3,47**	**5,10**
64	**7**	**0,875**	1,00	**1,74**	2,22	**-0,18**	**-3,32**	**6,13**
65	**8**	**1**	0,98	**2,28**	2,93	**-0,83**	**-3,79**	**5,39**

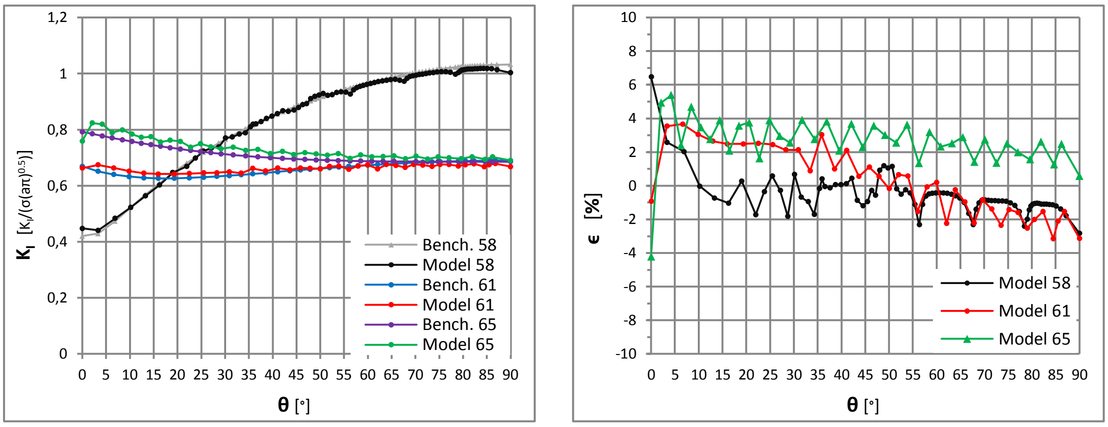

a) b)

Figure 4.22: SIF comparison and the error for model 58 and the closed-form solution.

4.2.3 B3 – Embedded elliptical crack

The performance of the embedded elliptical crack in a finite plate is investigated relative to the benchmark solution B3 with pure tension. Four different crack size ratios are tested to evaluate the accuracy of embedded elliptical cracks, where the crack ratio (a/c) ranges from 0.2 to 1. High end analysis is used with small mesh sizes at the crack tip to guarantee converged results. The load is pure tension and boundary conditions are implemented to prevent rigid body motion. Visualization of the model and the high refinement is shown in Figure 4.23 for model 66.

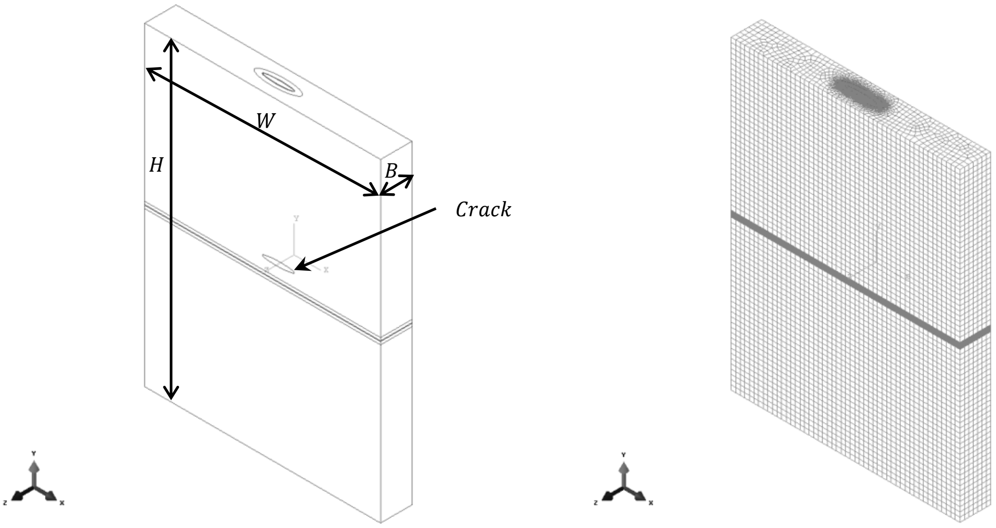

a) b)

Figure 4.23: The specimen dimensions and partitions in a) and the mesh in b) for benchmark case B3.

In this analysis, crack width c is the dimension controlling the crack ratio a/c, while the crack depth a is kept constant. Due to the low crack ratio in model 66, the partition radius El_C and tangential mesh size of the crack front partition, h_{x3} cannot be kept fixed. Otherwise, the partitions and mesh sizes in the model are the same in the different models.

The complete specification of the various models is defined in Table 4.41 and Table 4.42. As can be seen in Table 4.41, crack tip mesh sizes h_{x1} and h_{x2} are 1.8 percent of the crack depth to guarantee converged results. The global mesh sizes g_W, g_H and g_B are 2.

Table 4.41: Identical properties for benchmark case B3

	Specimen size			Mesh size				Partition size			
Model	Spec. width	Spec. height	Spec. depth	Tip width	Tip height	Ellipse height	Ellipse tang.	Contour domain height	Contour domain width	Ellipse radius, A	Ellipse height
–	W/a $[-]$	H/a $[-]$	B/a $[-]$	h_{x1}/a $[-]$	h_{x2}/a $[-]$	el_{height}/a $[-]$	el_{tang}/a $[-]$	H_{x1}/a $[-]$	H_{x2}/a $[-]$	El_A/a $[-]$	El_{height}/a $[-]$
17-25	100	133	13	**0,018**	**0,018**	0,20	0,23	**0,027**	**0,027**	2,7	2,7

Table 4.42: Unique properties for benchmark case B3

	Specimen size		Mesh size	Partition size	Mesh properties	
Model	Crack depth	Crack ratio	Tip tang.	Ellipse radius, C	Element rings	Elements
-	a $[m]$	a/c $[-]$	h_{x3}/a $[-]$	El_C/a $[-]$	- [#]	C3D8r [#]
66	**1,5**	**0,2**	0,167	10	6	732 351
67	**1,5**	**0,3**	0,100	6,7	6	464 095
68	**1,5**	**0,5**	0,100	6,7	6	492 274
69	**1,5**	**1,0**	0,100	6,7	6	430 664

The contour domain is specified with seven element rings and the first three are discarded in the SIF estimation ($n = 3$). The results from the benchmark are post-processed according to the post-processing procedure described for elliptical cracks. Reference solution, K_{ref}, is consequently the closed-form solution (2.40) in this benchmark analysis.

According to the average error magnitude in Table 4.43, the SIF results correlates very good for the embedded crack. The average error magnitude ranges from 0.97-1.43 percent. In contrast to the benchmark analysis of the semi-elliptical surface crack, the embedded crack gives increasing correlation for more circular cracks. According to the maximum error, there exist some error peaks. Model 67 exhibits a peak error of 6.35 percent. This is not seen in the other models and is likely connected to some meshing problem of that model. Otherwise, the error has a small variation according to the error STD, where it is below 1.43 percent for all models.

Following the plots in Figure 4.24, the correlation for the embedded cracks is seen. The error is stable with a uniform deviation along the crack front, predicting the values at the critical positions 0°and 90° well.

It can be concluded that the embedded crack case gives very good correlation to the closed-form solution. This can be motivated by the fact that stress state is simpler since the crack is not close or intersecting the free surfaces of the specimen.

Disregarding the peak value in model 67, the error is less than 5 percent for all crack cases.

Table 4.43: Results: Benchmark case B3

Model	Crack depth	Crack ratio	Avg. Rel. SIF STD	Avg. SIF Error mag.	Error STD	SIF Error 0°	SIF Error 90°	SIF Max error
	a [m]	a/c [-]	$(s/K_I)_{avg}$ [%]	$\lvert\epsilon\rvert_{avg}$ [%]	ϵ_{STD} [%]	ϵ_{0° [%]	ϵ_{90° [%]	ϵ_{max} [%]
66	**1,5**	**0,15**	0,95	**1,22**	0,94	**-3,19**	**-0,14**	**3,23**
67	**1,5**	**0,3**	0,44	**1,43**	1,43	**2,84**	**-0,88**	**6,35**
68	**1,5**	**0,5**	0,66	**1,11**	0,71	**-0,66**	**0,23**	**2,25**
69	**1,5**	**1**	0,67	**0,97**	1,33	**-0,86**	**-1,65**	**-3,24**

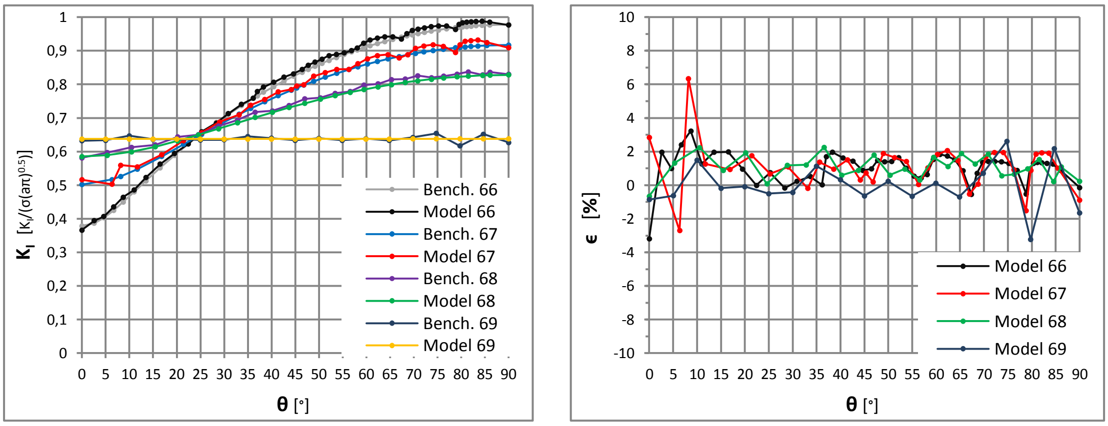

a) b)

Figure 4.24: SIF comparison and relative error for model 66 and the closed-form solution.

4.2.4 B4 – Corner crack at hole

The two corner cracks in a hole in benchmark B4 is investigated for a crack dimension with crack ratio $a/c = 1$, i.e. a circular crack. An accuracy test of K_I is performed where the models are compared to the closed-form solutions. The high end meshing technique is applied in the region of the hole. The crack and crack tip partition is implemented around the edge of the hole, see Figure 4.25a. With this modification, high end analysis is performed in the regular manner for elliptical cracks. Visualization of the mesh in model 1 is shown in Figure 4.25b where the high focus of the crack and hole (stress raiser) can be seen. The loading case is pure tension with boundary conditions to prevent rigid body motion.

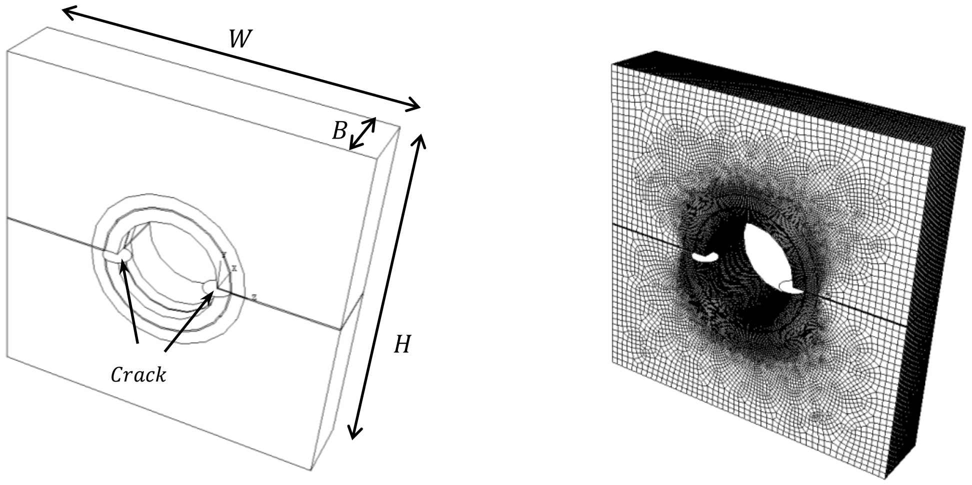

a) b)

Figure 4.25: The specimen dimensions and partitions are defined in a) and the mesh in b) for benchmark case B4.

The dimensions of the specimen are defined in Table 4.44, the element sizes for the different partitions are presented in Table 4.45 and in Table 4.46 the dimensions of the partitions are specified.

Table 4.44: Crack and specimen dimensions for benchmark case B4

Model	Crack depth	Crack ratio	Specimen width	Specimen height	Specimen depth
-	a $[m]$	a/c $[-]$	W/a $[-]$	H/a $[-]$	B/a $[-]$
70	**0,04**	**1**	12,5	12,5	5

Table 4.45: Mesh sizes for benchmark case B4

Model	Tip width	Tip height	Tip tang.	Part. width	Part. height	Part. depth	Global width	Global height	Global depth
-	h_{x1}/a $[-]$	h_{x2}/a $[-]$	h_{x3}/a $[-]$	p_W/a $[-]$	p_H/a $[-]$	p_B/a $[-]$	g_W/a $[-]$	g_H/a $[-]$	g_B/a $[-]$
70	**0,009**	**0,009**	0,05	0,175	0,0868	0,175	0,5	0,5	0,5

Table 4.46: Mesh properties for benchmark case B4

Model	Contour domain width	Contour domain height	Part. width	Part. height	Part. depth	Element rings	Elements
-	H_{x1}/a $[-]$	H_{x2}/a $[-]$	P_W/a $[-]$	P_H/a $[-]$	P_B/a $[-]$	- [#]	C3D8r [#]
70	**0,1**	**0,1**	2,04	0,942	2,04	5	876 240

The stress intensity factor for the model is averaged using all element rings except the first two, i.e. $n = 2$. The post-processing procedure is done as described for elliptical cracks and the reference solution is the closed-form solution (2.41).

Model 70 gives and average error magnitude of 71.1 percent, which is far beyond any other model presented previously. Following Figure 4.26 it can be seen that the model overestimates the stress intensity factor along the whole crack front. On the other hand, it can be seen that the shape of the stress intensity factor along the crack front is very similar, where the error is stable with a standard deviation of 3.37 percent. In addition, the standard deviation of the SIF is relatively low, 5.72 percent according to the table, which proves that the solution is sufficiently converged. In this context, no direct problems in the FE model can be seen where the mesh in the crack region is performed in the same manner as usual and the mesh size in the hole region (stress raise region) is very small.

According to model 70, correlation between the Abaqus results and the closed-form solutions is not obtained. The behavior of the SIF along the crack front is similar but not the magnitude. The reason why the results differ so much is unknown. The erroneous response of XFEM in Abaqus for holes with cracks cannot be fully guaranteed by this work. Error sources can instead be present in the post-processing or the comparison of the closed-form solution. In contrast to this, several models with different mesh approaches have all given the same overestimating behavior.

Table 4.47: Results: Benchmark case B4

Model	Crack depth	Crack ratio	Avg. Rel. SIF STD	Avg. SIF Error mag.	Error STD	SIF Error 0°	SIF Error 90°	SIF Max error
	a [m]	a/c [-]	$(s/K_I)_{avg}$ [%]	$\|\epsilon\|_{avg}$ [%]	ϵ_{STD} [%]	ϵ_{0° [%]	ϵ_{90° [%]	ϵ_{max} [%]
70	**0,04**	**1**	5,72	**71,10**	3,37	**58,34**	**70,63**	**76,09**

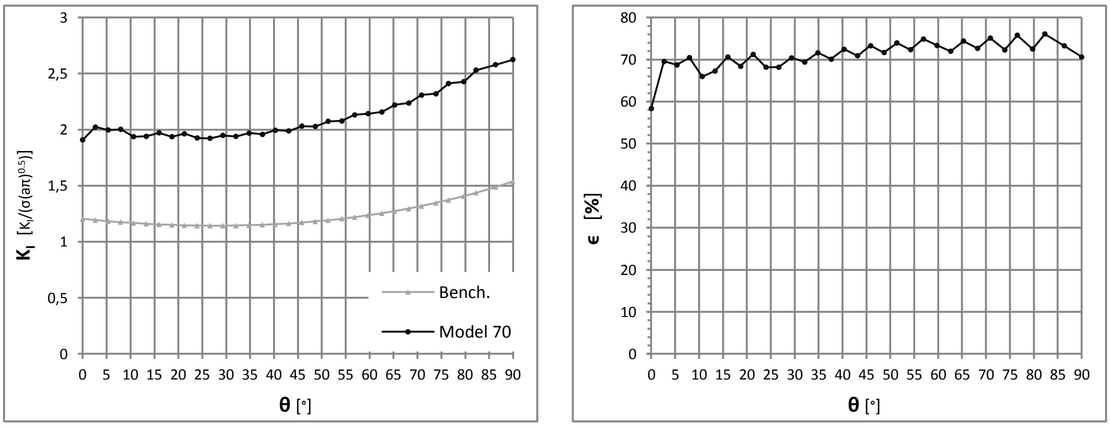

a) b)

Figure 4.26: SIF and ϵ for model 70 and the closed-form solution.

4.2.5 B5 – Semi-elliptical crack at U-notch

A specimen with a crack at the root of the notch is investigated for a crack dimension with crack ratio $a/c = 0{,}2$. The high end meshing technique is applied and the model and mesh is visualized in Figure 4.27. The loading case is pure tension with boundary conditions to prevent rigid body motion.

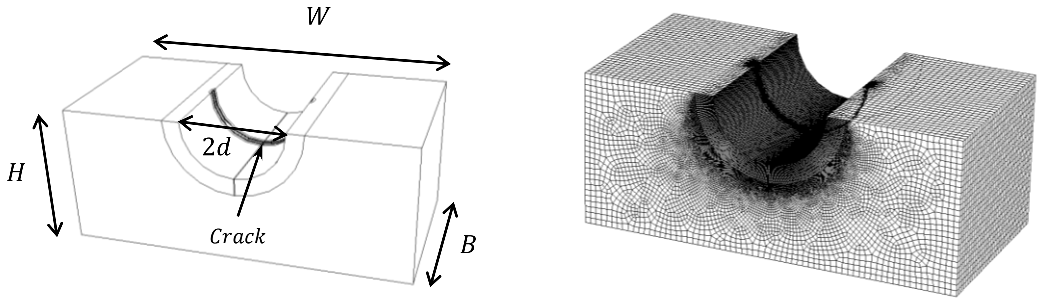

a) b)

Figure 4.27: The benchmark case B5 modeled in Abaqus is seen including specimen dimensions, partitions and mesh. The crack is so small that it cannot be seen in a).

The dimensions of the specimen, the mesh size and the dimensions of the partitions are seen in Table 4.48, Table 4.49 and Table 4.50, respectively.

Table 4.48: Crack and specimen dimensions for benchmark case B5

Model	Crack depth	Crack ratio	Specimen width	Specimen height	Specimen depth
-	a $[m]$	a/c $[-]$	W/a $[-]$	H/a $[-]$	B/a $[-]$
71	**2**	**0,2**	500	200	250

Table 4.49: Mesh sizes for benchmark case B5

Model	Tip width	Tip height	Tip tang.	Ellipse vert.	Ellipse tang.	Global width	Global height	Global depth
-	h_{x1}/a $[-]$	h_{x2}/a $[-]$	h_{x3}/a $[-]$	el_{height}/a $[-]$	el_{tang}/a $[-]$	g_W/a $[-]$	g_H/a $[-]$	g_B/a $[-]$
71	**0,09**	**0,09**	0,55	1	1	7,5	7,5	7,5

Table 4.50: Mesh properties for benchmark case B5

Model	Contour domain width	Contour domain height	Ellipse radius, A	Ellipse radius, C	Ellipse height	Element rings	Elements
-	H_{x1}/a $[-]$	H_{x2}/a $[-]$	El_A/a $[-]$	El_C/a $[-]$	El_{height}/a $[-]$	- [#]	C3D8R [#]
71	**1**	**1**	5	10	471	5	686 331

The stress intensity factor for the model is estimated using all element rings except the first two ($n = 2$). The reference solution is the closed-form solution (2.42) for 0° (point C) and (2.43) for 90° (point A). The post-processing procedure is done as described for elliptical cracks. In Table 4.51, the SIF and errors at point A and C are displayed.

The errors are exceedingly high compared to the closed-form solution. Compared to the benchmark analysis of a corner crack at hole (Section 4.2.4) the overestimation of the error is similar, around 80-100 percent. Hence, this analysis gives additional evidence of the problems in Abaqus to simulate the correct crack response in the region of stress raisers.

Table 4.51: Results: Benchmark case B5

Model	Crack depth	Crack ratio	SIF Abaqus point A	SIF Bench. point A	SIF error point A	SIF Abaqus point C	SIF Bench. point C	SIF error point C
-	a $[m]$	a/c $[-]$	$K_{I,A}$ $[-]$	$K_{I,A}$ $[-]$	ϵ_A [%]	$K_{I,C}$ $[-]$	$K_{I,C}$ $[-]$	ϵ_C [%]
71	**2**	**0,2**	6,52	3,30	**97,90**	2,97	1,66	**79,50**

5 Strategy proposal

Based on the convergence analysis and the benchmark analysis, a strategy is proposed here on how to perform stationary crack analysis with XFEM. Mesh requirements are suggested for certain accuracies and various crack cases are verified. The strategy consists only of guidelines and not exact rules. It should be noted that the suggested parameters are verified only for the crack cases that are stated.

5.1 Mesh technique

High end analysis (requirement of accuracy: < ~5 percent error)

Mesh construction:

- Conformed mesh at crack tip region.
- High mesh density at crack tip region.

Modeling difficulty:

- Difficult to achieve in general and especially problematic for crack specimens with complex geometries.

Modeling flexibility:

- Low flexibility with respect to crack placement (cracks can't be moved due to the conformed crack tip mesh region).
- Low flexibility with respect to crack dimension (cracks can't be varied due to the conformed crack tip mesh region).
- Time consuming mesh construction.
- Fast increase in model size for mesh refinements (large number of elements required in the overall region due to the refinement of the crack tip region).

Mesh requirements for the crack tip of a straight crack:

- Crack tip mesh size: < 7.7 percent of crack length.
- Size of contour domain in contour integral calculation: 5-100 percent of crack length.
- Number of element rings in contour integral calculation: ≥ 4.
- Verified for: Through-thickness crack.

Mesh requirements for the crack tip of an elliptical crack:

- Crack tip mesh size: < 0.8 percent of crack depth.
- Size of contour domain in contour integral calculation: 5-25 percent of crack depth.
- Number of element rings in contour integral calculation: ≥ 5.
- Verified for: Semi-elliptical surface crack.

Mesh requirements of crack region (outside the crack tip region):

- Small effects of mesh size compared to the crack tip region.
- Crack region mesh size: < 17.5 percent of crack length
- Verified for: Through-thickness crack

Low end analysis (requirement of accuracy: < ~10 percent error)

Mesh construction:

- Un-conformed mesh at crack tip.
- High mesh density at overall crack region (without focus on the crack tip).

Modeling difficulty:

- Easy to achieve for both general and complex geometries.

Modeling flexibility:

- High flexibility with respect to crack placement (cracks can be moved within the refined crack region).
- High flexibility with respect to crack dimension (cracks can be varied within the refined crack region).
- Fast mesh construction.
- Fast increase in model size for mesh refinements (large number of elements required in the overall region due to the refinement of the crack region).

Mesh requirements for elliptical crack:

- Crack region mesh size: < 13 percent of crack depth
- Size of contour domain in contour integral calculation: 167-200 percent of crack depth
- Number of element rings in contour integral calculation: ≥ 7
- Verified for: Semi-elliptical surface crack

General modeling suggestions

Hexahedral elements with reduced integration scheme is suggested

- Reduction in calculation time relative to full integration: 10-20 percent
- Difference in K_I relative to full integration: < 0.15 percent
- Verified for: Through-thickness crack

Free crack placement in mesh suggested

- Difference in K_I: < 1 percent (crack tip placed in middle of elements, at element boundaries and the nodes).
- Verified for: Semi-elliptical surface crack.

Extrapolation at position where crack breaks surface suggested

- Extrapolate the SIFs from the closest integration points to position at surface (numerical problems for contour integral at this point).

5.2 Simplification technique

General simplification suggestions

Submodeling is suggested for large structures

- Use both displacement and stress based submodels to find the lower and upper limit of the real solution (i.e. solution from the full model).
- Requirement: include the stress field emanating from the crack
- Difference in K_I relative to full models: < 1,5-4 percent.

Mixed element types is suggested for complex geometries

- Hexahedral mesh around crack required
- Tetrahedral mesh outside crack region
- Difference in K_I: < 0.3 percent
- Verified for: Through-thickness crack

5.3 Crack cases

Through-thickness crack – B1: Approved

- Specimen with “infinite” depth: error less than 4.5 percent

Semi-elliptical surface crack – B2: Approved

- Verified crack ratios: $0.125 \leq a/c \leq 1$
- Accuracy: less than 5 percent error
- Numerical problems when crack tip breaks the surface (large peak variations of K_I)

Embedded elliptical crack – B3: Approved

- Verified crack ratios: $0.15 \leq \mathrm{a/c} \leq 1$
- Accuracy: less than 5 percent error

Corner crack at hole – B4: Not approved

- Error: 60-80 percent along the crack front

Semi-elliptical crack at U-notch – B5: Not approved

- Error: 80-100 percent at 0° and 90°

6 Conclusions

Crack modeling with XFEM in Abaqus has been evaluated for five different crack cases and, from these results, a strategy for crack modeling using the software is proposed based on a convergence analysis for mesh sizes and other aspects of XFEM.

Overall, a good agreement of K_I has been obtained between XFEM and the benchmark solutions with relative errors less than 10 percent. For the specimens with stress raisers (notches/holes) the agreement was surprisingly poor with relative errors between 60-100 percent. It was seen that the shape of K_I along the crack front were similar, but with a consistent difference in magnitude. These results are a severe setback since most geometries consist of some sort of stress raiser and it reduces the area of use for XFEM.

XFEM is often proposed to be a mesh-independent method, i.e. the mesh does not have to follow the crack geometry. But the modeling method showed a higher mesh dependency than expected, where the mesh size at the crack tip showed to be the aspect that affected the accuracy the most. XFEM enables for a relatively simple/flexible crack modeling in terms of mesh construction, but the accuracy is varying with the flexibility. A conformed mesh around the crack tip, similar to what is used in conventional crack modeling, gives very good results within 5 percent error. However, this kind of mesh refinement is hard to accomplish for complex structures. An unstructured mesh is more flexible and easier to model but is shown to give lower accuracy (within 10 percent error).

Caution should be taken when the crack breaks the specimen surface. The contour integral is evaluated poorly at the surface which results in erroneous SIFs there. It is advised to disregard this value and extrapolate the SIF from the closest evaluation points.

Submodeling has proven to work well with XFEM and is recommended to handle larger structures. Using both stress and displacement based submodels is advised to find the limits where the real solution lies within. Mixed tetrahedral-hexahedral FE-meshes with tie constraints have also shown good results. It simplifies the mesh modeling, thus increasing flexibility while the accuracy is maintained. The approach is recommended for more complex geometries, where the crack region is meshed using hexahedral elements while tetrahedral elements are used outside the crack region. This is only proven for a straight crack case, whereas a more complex loading situation can be disturbed by the constraint between the meshes to a greater extent.

Elements with reduced integration scheme give for pure tension loads a reduction of the calculation time by 10-20 percent. The loss in accuracy is less than 1 percent and the reduced integration scheme is therefore concluded to be applicable for XFEM. It should be noted that this is not proven for complex load situations.

The requirements on the SIF solution in the thesis are thought to be too high for practical use. Larger mesh sizes are therefore suggested to be investigated further, especially for conformed meshes. The results for notched specimens differ vastly and therefore further studies of cracks with stress raisers are suggested. In this context, the usage of reduced integration could be examined as a potential problem. Other benchmark cases with stress raisers could be investigated, but also the cases analyzed in this thesis could be further studied to strengthen or disapprove these results. Furthermore, the models could be tested using conventional crack modeling techniques using conformed meshes.

7 References

[1] BS 7910, Guide to methods for assessing the acceptability of flaws in metallic structures.

[2] DNV-RP-C203*, Fatigue design of offshore steel structures, 2010*

[3] ISO13628-7 *Petroleum and natural gas industries - Design and operation of subsea production systems*, 2006.

[4] Moës, N., Dolbow, J., Belytschko, T. (1999): A finite element method for crack growth without remeshing. *International Journal for Numerical Methods in Engineering,* Vol. 46, No. 1, 1999, pp. 132-150.

[5] Belytschko, T., Gracie, R., Venture, G. (): a Review of extended/generalized finite element methods for material modelling. *Modelling and Simulation in Materials Science and Engineering*, vol. 17, No 4, 2009, pp. 043001.

[6] Dassault Systèmes (2011): *Abaqus 6.11 Online Documentation*, Dassault Systèmes, Providence, Rhode Island.

[7] Sukumar, N., Moës, N., Moran, B., Belytschko, T. (1999): Extended finite element method for three-dimensional crack modelling. *International Journal for Numerical Methods in Engineering*, Vol. 48, No. 11, 2000, pp. 1549-1570.

[8] Dowling, N. E. (2007): *Mechanical behaviour of materials*. Pearson Prentice Hall, Upper Saddle River, New Jersey.

[9] Miannay, Dominique P. (1997): *Fracture Mechanics*. Springer-Verlag New York Inc., New York.

[10] Shih, C.F., Moran, B., Nakamura, T. (1985): Energy release rate along a three-dimensional crack front in a thermally stressed body. *International Journal of Fracture,* Vol. 30, No. 2, 1986, pp. 79-102.

[11] Rice, J. R. (1968): A path independent integral and the approximate analysis of strain concentrations by notches and cracks. *Journal of Applied Mechanics,* Vol. 35, No 2, 1968, pp. 379-386.

[12] Shih, C. F., Asaro, R. J., (1988): Elastic-Plastic Analysis of Cracks on Bimaterial Interfaces: Part I - Small Scale Yielding. *Journal of Applied Mechanics*, Vol. 55, 1988, pp. 299-316.

[13] Melenk, J.M., Babuska, I. (1996): The partition of unity finite element method: Basic theory and applications. *Computer Methods in Applied Mechanics and Engineering*, Vol. 139, No. 1, 1996, pp. 289–314.

[14] Belytschko, T., Black, T. (1999): Elastic crack growth in finite elements with minimal remeshing. *International Journal for Numerical Methods in Engineering,* Vol. 45, No. 5, 1999, pp. 601-620.

[15] Wormsen, A., Fjeldstad, A., Härkegård, G. (2006): The application of asymptotic solutions to a semi-elliptical crack at the root of a notch. *Engineering Fracture Mechanics,* Vol. 73, No. 13, 2006, pp. 1899-1912

[16] Råde, L. (1988): *Mathematics handbook for science and engineering*. Studentlitteratur, Lund, Sweden.

[17] Raju, I.S., Newman, J.C., (1979): Stress-intensity factors for a wide range of semi-elliptical surface cracks in finite-thickness plates. *Engineering Fracture Mechanics*, Vol. 11, No. 4, 1979, pp. 817-829.